Kinetics of Isotope-Labeled Pathways in the Ozone Forming Recombination Reaction

Elizaveta Grushnikova
Marquette University

KINETICS OF ISOTOPE-LABELED PATHWAYS IN THE OZONE FORMING RECOMBINATION REACTION

by
Elizaveta Grushnikova

Milwaukee, Wisconsin
December 2022

ABSTRACT
KINETICS OF ISOTOPE-LABELED PATHWAYS IN THE OZONE FORMING RECOMBINATION REACTION

Elizaveta Grushnikova, M.S.

Marquette University, 2022

The ozone layer in Earth's atmosphere is unique and plays a vital role in the development of life. Studying the mechanism behind ozone formation helps us understand the development of our planet's atmosphere. We focus here on the anomalous mass-independent isotope effect.[1] In 1981, Mauersberger et al.[2] performed an experiment using weather balloons, resulting in the discovery of the anomalous isotope effect for ozone formation. Since then, other chemists have continued to investigate the theory behind this phenomenon. To understand the nature of the isotope effect, we must consider all stages of ozone formation. The basic reaction for ozone formation is $O + O_2 \rightarrow O_3$. To further describe ozone's formation, several theoretical mechanisms have been developed. A commonly used mechanism at the low-pressure regime is the energy transfer (Lindemann) mechanism[3] which involves a metastable intermediate state O_3*. At the second step of the reaction, energy is transferred from the intermediate state O_3* to the bath gas. Metastable intermediate state of O_3* is explained by scattering resonance in quantum mechanics. Here, we use the mixed quantum classical approach. The quantum approach is related to consideration of the scattering resonances with their eigenvalues, eigenfunctions, probabilities and resonance widths. The classical approach is related to kinetics of ozone formation including the stabilization step. The relevant parameters are presented and compared with experimental results, specifically the temperature and pressure dependence of rate coefficients and isotope effects.

ACKNOWLEDGEMENT

I would like to express my appreciation to my professor Dr. Dmitri Babikov. He has accepted me into his group, where the work was not easy for me, but thanks to his patience and readiness to teach me scientific methods and discipline, I was able to accomplish my graduate work. I want to say a special thanks to my co-workers Igor Gayday and Adil Yermek for being my friends and good advisors. Thank you for constant support and fruitful discussions. You have been a great team and true friends. During my stay in Milwaukee, you created an enjoyable environment.

I want to say a special thanks to Prof. Nobile who always supported me while I was her TA. Her encouraging example inspired me during teaching. Her professionalism and empathy toward students made a huge impression on me.

To Dr. Vyas for his understanding and patience in working with me and being professional all the time. Thank you for being a great professional example for all of us.

Thank to Dr. Timerghazin, Dr. Kedem and Dr. Huang to be a part of my committee, instructing me, and being with me during my PhD path.

I want to say thanks to my family, especially to Dan Wenzel, grandfather of my son Emmett. Thank you, Dan, for the support and most importantly for your constant believing in me. Without you I would not have reached this point. Finally, I want to express my deepest gratitude to Stuart Baker for his encouragement, constant support, understanding and being the love of my live.

TABLE OF CONTENTS

ACKNOWLEDGEMENT iii

LIST OF TABLES vii

LIST OF FIGURES ix

CHAPTER I. INTRODUCTION 1

I-1 Ozone in the Earth Atmosphere 1

I-2. Recombination Mechanisms 4

I-3. Description of Quantum Resonances Using Stabilization Method 10

I-4 Kinetics for Single Recombination Pathway 15

I-5. Objectives and the Structure of This Dissertation 18

CHAPTER II. Four Isotopically Labelled Recombinaetion Pathways on the Potential Energy Surface of Ozone 20

II-1. Introduction 20

II-2. Channel-Specific and Product-Specific Rate Coefficients 25

II.3. Recombination Rate Expression for Single Substitution 29

II.4. Kinetic Weight of a Resonance 33

II.5. Dynamical Partition Function 34

II.6. Concise Rate Expressions 35

II.7. Isotope Exchange 35

II-8 Product Specific Recombination Rate Coefficients 37

II-9 Channel Specific Recombination Rate Coefficients 38

II-10 Zero-Pressure vs. High-Pressure Limits 39

II-11 Isotope Effects 42

II-12 Summary 44

CHAPTER III. Doubly Substituted Isotopologue of Ozone 46

III-1. Introduction....46

III-2. Kinetics Expressions for Double Isotopic Substitution....47

III-3. Analysis of Temperature Dependencies. 53

III-4. Summary....57

CHAPTER IV. Numerical Results: Isotope Effects, Insertion Pathway, and Temperature Dependence....59

IV-1. Introduction 59

IV-2. Updated Values of Pathway-Specific Rate Coefficients....63

IV-3. Temperature Dependencies of Recombination Rates 68

IV-4. Temperature Dependencies of Isotope Effects....78

IV-5. Summary 83

CHAPTER V. Properties of Scattering Resonances in Ozone and Their Role in the Isotope Effects 85

V-1. Introduction....85

V-2. Distribution of Resonance Widths....89

V-3. Resonance Widths in Symmetric and Asymmetric Ozone Molecules 93

V-4. Empirical Model for Splitting the Van der Waals Probabilities....96

V-5. Summary....98

CHAPTER VI. The Model of Stabilization and Application to Kinetic Theory....99

VI-1. Exponential Model of Stabilization....99

VI-2. Testing the Exponential Model 103

VI-3. The Exponential Model with Transitions between the States 112

VI-4. Numerical Results with New Stabilization Model. 119

CHAPTER VII. SUMMARY 128

Appendix A. Calculation of the Reagent Partition Functions and Equilibrium Constants for the Isotope Exchange 130

BIBLIOGRAPHY 135

LIST OF TABLES

Table 1. The contribution of Chaperon and Lindeman mechanism at different temperatures to ozone recombination. 8

Table 2. The efficiency of Lindeman and chaperon mechanisms at different temperature and pressure regimes. 9

Table 3. The ratios of rate coefficients for exo- and endo-ergic pathways A and B over the rate coefficient for an iso-ergic pathway S, for singly and doubly substituted cases, and their expressions in terms of the dynamical partition functions. 55

Table 4. The ratios of rate coefficients for singly and doubly substituted cases, using exo- and endo-ergic pathways A and B, and an iso-ergic pathway S, and their expressions in terms of the dynamical partition functions. 56

Table 5. The ratios of rate coefficients in singly and doubly substituted cases, using lower and upper Channels 1 and 2, and their expressions in terms of the dynamical partition functions. 57

Table 6. Experimental and theoretical rate coefficients (in the units of 10^{-35} cm^6/s) for different pathways of ozone formation at room temperature in the cases of single and double isotopic substitution, and the corresponding isotope effects 60

Table 7. Theoretical and experimental and rate coefficients (in the units of 10^{-35} cm^6/s) for various pathways of ozone formation at room temperature in the cases of single and double isotopic substitution, and the corresponding isotope effects. 65

Table 8. Experimental and theoretical slopes (gradients per 1000 K) obtained from temperature dependencies of pathway-specific rate coefficients at 300 K. Note that experiment and theory use different reference pathways. 69

Table 9. Temperature dependence of pathway specific recombination rate coefficients (3rd order, 10^{-35} cm^6/s) for singly and doubly substituted cases, computed theoretically for the range $200 \leq T \leq 400$ K. 72

Table 10. The slopes (gradients per 1000 K, at $T = 300$ K) for various ratios of the pathway-specific rate coefficients obtained from theoretically computed temperature dependencies. 72

Table 11. The slopes (gradients per 1000 K, at $T = 300$ K) of the ratios of rate coefficients for singly and doubly substituted cases, using exo- and endo-ergic pathways A and B, and an iso-ergic pathway S. 73

Table 12. The slopes (gradients per 1000 K, at $T = 300$ K) for the ratios of channel-specific rate coefficients obtained from theoretically computed temperature dependencies. 77

Table 13. Temperature dependence of isotope effects for singly and doubly substituted cases, computed theoretically for the range $200 \leq T \leq 400$ K. 79

Table 14. Average resonance widths and their corresponding lifetimes for the resonances of three kinds in singly and doubly substituted ozone molecules. 92

Table 15. Average resonance widths and their corresponding lifetimes for the resonances localized over the covalent well of symmetric and asymmetric ozone molecules in the cases of single and double substitution. 94

Table 16. The temperature dependence of the ΔE based on the fitting results of experimental temperature dependence. ΔE from second column was used for blue theoretical curve; ΔE from third column used for green theoretical curve on Figure 31. 109

Table 17. The temperature dependence of the ΔE based on the data of Schinke.[18] In first colomn with ΔE contains the vibrational ΔE which was used for exponential model. $\Delta E\downarrow$ and $\Delta E\uparrow$ are depicted in the Figure 34. 116

Table 18. The best fitting parameters to describe the temperature and pressure dependences of isotope effects and k_{666}. The results achieved with these parameters in terms of absolute value of η, δ-effects at 300 K, absolute value of k_{666}. 127

Table 19. The rotational partition function calculated with two approaches for singly- and doubly substituted molecules in the wide range of temperatures. 131

Table 20. Ratios singly- and doubly substituted exponential factors with ΔZPE corresponding partition functions ratio of channels and gradients per 1000 K (temperature dependence slopes at 300 K)..... 132

LIST OF FIGURES

Figure 1. Pressure dependence of the recombination rate coefficient k_{rec} × [M], experimental data of Troe et al.[16] at several temperatures. The linear dependence corresponds to the second order rate coefficient k_{rec}. Plateau corresponds to the 3d order k_{rec}. 5

Figure 2. The fitting of experimental temperature dependence of recombination rate coefficient for ozone with Chaperon and Lindeman mechanisms with fitting Equations 7 and 8 accordingly. 7

Figure 3. The temperature dependence of recombination rate coefficient. Dots are the experimental results. The lines correspond to the theoretical predictions with Chaperon mechanism. The closest coincidence with experiment lies in the area of low temperature. At the room temperature on 25% accounts for Chaperon mechanism. It assumed that alternative Lindeman mechanism dominates at the higher temperature. 8

Figure 4. Energy diagram with one dimensional Morse potential with three types of states at J = 80. Green lines correspond to the bound states. Red lines correspond to the resonances and the rest are the free particle states. Orange line shows the boundary wall which was moved. 11

Figure 5. Diagram of $^{668}O_3$ isotope continua. Highlighted region underlines irregularly behavior and corresponds to resonance state from bottom to the top V = 12, 13, 14. First two states are distinguishable resonance narrow states, the third state is barely visible broad resonance 12

Figure 6. Second derivative of energies relative to extension of the grid boundary as a function of energies (J=24). Resonance energy corresponds intersection of x axis around 100 cm^{-1}. 13

Figure 7. Wave functions for resonance states of $^{668}O_3$ isotopomer with potential energy curve. Three eigenfunctions are depicted with corresponding vibrational quantum numbers. Lower two are comparably narrow resonances under the rotational barrier, the last one is a broad resonance state above the barrier. 14

Figure 8. Pressure dependence of the second-order recombination rate coefficient κ_{rec} × [M]. Colored symbols depict experimental data. Green line is the result of the theoretical evaluation summarizes the 1D kinetic model. 17

Figure 9. Schematic of the global PES of ozone that possesses a three-fold symmetry with respect to the entrance channels and product wells. The channels and wells are labeled for singly substituted (left) and doubly substituted (right) isotopologues. Reagents are indicated by black letters, the product ozone molecules by white letters. Four distinguishable reaction pathways are also indicated in each case, by red letters and arrows. The "insertion" pathway is shown schematically by the dashed arrow. 22

Figure 10. Two distinct channels of ozone formation (left and right) and the metastable ozone states (middle) in the case of singly isotopic substitution. Here "6" denotes ^{16}O whereas "8" denotes ^{18}O. Lower energy channel corresponds to the heavier diatomic reagent $^{16}O^{18}O$ with smaller zero-point energy. Upper channel corresponds to the lighter diatomic reagent $^{16}O^{16}O$. Energy difference of the two channels, ΔZPE, is indicated..... 31

Figure 11. Two distinct channels of ozone formation (left and right) and the metastable ozone states (middle) in the case of double isotopic substitution. Here "6" denotes ^{16}O whereas "8" denotes ^{18}O. Lower energy channel corresponds to the heavier diatomic reagent $^{18}O^{18}O$ with smaller zero-point energy. Upper channel corresponds to the lighter diatomic reagent $^{16}O^{18}O$. Energy difference of the two channels, ΔZPE, is indicated..... 46

Figure 12. Experimental temperature dependence of k_B (rate coefficient for pathway B) relative to k_{888} in the case of single substitution, and relative to k_{666} in the case of double substitution. 68

Figure 13. Temperature dependencies of the ratios of pathway-specific rate coefficients defined in Table 10 (see the Table for color assignments). Single and double isotopic substitutions are plotted by dashed and solid lines, respectively. 74

Figure 14. Temperature dependencies of various ratios of the pathway specific rate coefficients in singly and doubly substituted isotopologues, as defined in Table 11. Colors are assigned in the Table 11. 75

Figure 15. Temperature dependencies of various ratios of channel-specific rate coefficients (upper vs lower channels), as defined in Table 12. Colors are assigned in Table 12. Single and double isotopic substitutions are plotted by dashed and solid lines, respectively. 76

Figure 16. Temperature dependencies of isotope effects in singly (dashed line) and doubly (solid line) substituted ozone molecules, computed using our theoretical model. 80

Figure 17. Theoretical (green) and experimental (orange) temperature dependencies of symmetry-driven isotope effect, the η-effect, in the case of single isotopic substitution. 82

Figure 18. Temperature dependencies of isotope η-effect according to Janssen[10] for singly substituted molecule..... 82

Figure 19. Probability in the van der Waals 1 (light blue) and van der Waals 2 (light green colors); asymmetric (blue) and symmetric (green) regions. 86

Figure 20. Dalitz-plot analysis of the p_i^{cov} versus p_i^{vdw} versus p_i^{free} for the scattering resonances in ozone. Upper right corner corresponds to the pure covalent states, lower corner corresponds to the pure van der Waals states, while upper left corner corresponds to the free particle states (unbound). The points distributed through the area of triangle exhibit all three probabilities..... 88

Figure 21. Distribution of resonance widths in singly (grey) and doubly (orange) substituted ozone molecules. Three ranges with different trends can be identified (shown by dashed lines)..... 90

Figure 22. Deconvolution of the overall distribution of resonance widths in the singly substituted ozone onto three component that correspond to the covalent well states (red), van der Waals plateau states (green), and the continuum states in the asymptotic region of the PES (blue). Their total (gray) is the same as in Figure 21. 91

Figure 23. Distribution of resonance widths for the covalent states in asymmetric (red) and symmetric (blue) ozone molecules. Left and right frames correspond to single and double isotopic substitutions. To simplify the comparison, we plotted Q_{asym} and $2Q_{sym}$ in order to offset the effect of symmetry. 94

Figure 24. Simple splitting of probability in the van der Waals plateaus of the PES (light blue and light green colors) between asymmetric (dark blue) and symmetric (dark green) ozone molecules. 95

Figure 25. Distribution of resonance widths for the van der Waals states in asymmetric (red) and symmetric (blue) ozone molecules. Left and right frames correspond to single and double isotopic substitutions. To simplify the comparison, we plotted Q_{asym} and $2Q_{sym}$ in order to offset the effect of symmetry. In this analysis, van der Waals probability in Channel 2 was split in halves between symmetric and asymmetric isotopologues, as shown in Figure 24. 96

Figure 26. Distribution of resonance widths for the van der Waals states in asymmetric (red) and symmetric (blue) ozone molecules. Left and right frames correspond to single and double isotopic substitutions. To simplify the comparison, we plotted Q_{asym} and $2Q_{sym}$ in order to offset the effect of symmetry. In this analysis, van der Waals probability in Channel 2 was split between symmetric and asymmetric isotopologues according to Equations 171 and 172. 97

Figure 27. Theoretical (green, red) and experimental (yellow) temperature dependencies of the η-effect for molecule $^{668}O_3/^{686}O_3$.[43] The orange diamond the η-effect reported in a paper of Janssen[10], the blue diamond was reported earlier[35]; the violet diamond corresponded to doubly substituted case.[10] 100

Figure 28. The pressure dependence of non-substituted ozone rate coefficient in comparison with experimental data[10,16,23]; with bath gas was taken as Ar. Red and yellow and green lines show the theoretical prediction with ΔE = 25, ΔE = 50 and 200 cm^{-1} accordingly. The measurements are in consistency with theoretical prediction with ΔE = 200 cm^{-1}. 105

Figure 29. The temperature dependence of non-substituted ozone rate coefficient in comparison with experiment.[10,16,23] Left picture corresponds to varying the P-model: 1) red curve corresponds to P-model with single covalent probability p_{cov} which multiplied by cross section in k^{stab}; 2) yellow curve corresponds to $p_{cov}+p_{vdw}$; 3) green curve – sqrt($p_{cov}+p_{vdw}$); 4) the blue curve - 5rt($p_{cov}+p_{vdw}$). Right picture corresponds to the σ_{stab} varied from red to violet as 12, 25, 50, 75, 100 and 1000 a_0^2. 106

Figure 30. The temperature dependence of non-substituted ozone rate coefficient in comparison with experimental data of Troe. Red and blue dotted lines correspond to $k_{rec}^{RC} = 1.7 \times 10^{34}\ (T/300)^{-3.2}$ cm^6 mol^{-2} s^{-1} and $k_{rec}^{ET} = 2.3 \times 10^{34}\ (T/300)^{-1.5}$ cm^6 mol^{-2} s^{-1} fitting equations. The red solid line corresponds to the sum of RC and ET mechanisms. The green line corresponds to theoretical predictions – a) theoretical curve with cross-section with T-dependent σ(T/500), ΔE = 200 cm^{-1}; b) theoretical curve with good fit of Lindeman k_{rec}^{ET}, temperature independent $\sigma = 1.5\sigma_0$ (σ_0 =154.03 a_0^2 , recommended for ozone), c) varied ΔE with constant σ_0..... 108

Figure 31. The temperature dependence of non-substituted ozone rate coefficient in comparison with experimental data of Troe[19]. Green line corresponds to theoretical prediction of k_{rec}^{ET}. Blue line corresponds to theoretical prediction of $k_{rec}^{ET} + k_{rec}^{RC}$..... 109

Figure 32. The pressure dependence of delta-effect predicted for the ΔE from 25, 50, 100 to 200 cm^{-1} (red, orange, yellow, green accordingly) compared to experimental data. The theoretical prediction involved exponential model discussed in the Appendix..... 110

Figure 33. The schematic picture of ozone formation through the metastable ozone states. The green arrows accounts for the stabilization to the all ground states from active resonance; the pink arrows describe the opposite process of repopulation of the resonance from bound. The red and violet arrows show the repopulation and dissosiation to other resonances accordingly. 113

Figure 34. Macroscopic reversibility principle compared to the theoretical prediction of Schinke[15]. Nine blue points connected with a line correspond to the table temperature range from 100 to 2500 K. Orange line corresponds to Equation 185 with $\Delta E\downarrow$ taken from Table 16..... 115

Figure 35. The effect of varying the σ_{stab} and σ_{tran}. On 35a (upper picture) σ_{stab} varies from 0.7 (red) to 1.5 a_0^2 (green) On picture 35b (lower picture) the σ_{tran} was varied from 0.9 a_0^2 (blue) to 32 a_0^2 (red). Red circles and diamond correspond to results of Lin and Leu[23] , the orange diamond of Maursberger[10], blue square, triangles and circles are from Troe.[16,46] 118

Figure 36. The effect of varying the σ_{stab} and σ_{tran}. On 32a (left picture) the pressure dependence with σ_{stab}= 1.12 a_0^2 and σ_{tran} = 6.5 a_0^2, on 32b (right picture) the temperature dependence with the same parameters. Bath gas – N_2/O_2 mixture. 121

Figure 37. The effect of varying p-creteria with Γ-criteria = 1 cm^{-1}. A black curve corresponds to the theoretical prediction without cutoff by p-creteria, the red curve correspondes to $p_{cutoff} = 10^{-5}$, the orange - $p_{cutoff} = 10^{-4}$, the green - $p_{cutoff} = 10^{-3}$, the blue - $p_{cutoff} = 10^{-2}$. 122

Figure 38. Experimental points for δ-effect with Γ-criteria = 1 cm^{-1}. A black curve corresponds to the theoretical prediction without any p-criteria, the red curve correspondes to $p_{cutoff} = 10^{-5}$, the orange - $p_{cutoff} = 10^{-4}$, the green - $p_{cutoff} = 10^{-3}$, the blue - $p_{cutoff} = 10^{-2}$. 124

Figure 39. Experimental points for temperature dependence of δ-effect. The lower two bold lines correspond to the theoretical prediction with Γ-criteria - 1 cm^{-1} and all states included. 125

Figure 40. Experimental points for pressure dependence of δ-effect with $\Gamma_{cutoff} = 1$ cm^{-1}. Left picture corresponds to singly substituted molecule with ^{18}O, right picture corresponds so substitution with ^{17}O. 126

Figure 41. Temperature dependencies of $Q_{ch2}/2Q_{ch1}$ in comparison of T-dependence of $\exp(-\Delta ZPE/kT)$. Brown curves are the ratio of partition functions in channels, purple curves are t-dependence of factors with ΔZPE. 134

Figure 42. The temperature dependence of exchange rate coefficient for doubly (orange) and singly (blue) substituted molecule in comparison with experimental data of Bella.[35] Orange and blue lines show the theoretical prediction and red dotted line is the experimental. The measurements are in consistency with theoretical prediction. 134

CHAPTER I. INTRODUCTION

I-1 Ozone in the Earth Atmosphere

Ozone (O_3) resides mainly in the stratosphere, absorbing the sun's harmful short-wavelength radiation which can cause skin cancer; this is positive role of ozone in atmosphere.[4] Widespread use of chlorofluorocarbons (aerosols and sprays), starting in the late 1970s, released molecules containing chlorine and bromine into our atmosphere, working to reduce Earth's protective ozone layer. However, a smaller amount (around 10% of all atmospheric ozone) exists in the troposphere.[5] The ozone at this level is largely anthropogenic and has become known as a dangerous air pollutant which can damage crops, cause lung illnesses as asthma. Furthermore, ozone in the troposphere can be subject to a reaction that produces the OH radical.[6] This radical can initiate cyclic reactions which damage plants and human's and animals' health or cause other effects, like photochemical degradation of rubber. Thanks to environmental protection measures, the ozone layer has luckily started to recover[7] in the recent years.

Chlorine from chlorofluorocarbons, for example, react with ozone, altering it:

$$Cl\ (g) + O_3(g) \rightarrow ClO\ (g) + O_2 \qquad (1)$$

Another example of a reaction through which ozone is broken down:

$$O_3(g) + NO_2\ (g) \rightarrow NO_3 + O_2 \qquad (2)$$

Combustion of fossil fuels is a major source of atmospheric NO_2. There are many more examples of reactions in which ozone is destroyed. However, it is formed mainly in the stratosphere through the three-body recombination reaction:

$$O_2 + O \rightarrow O_3 \qquad (3)$$

Ozone forms from oxygen. Oxygen has three stable isotopes - ^{16}O, ^{17}O and ^{18}O with the abundances of 99.76%, 0.04% and 0.2%[8], respectively. The first attempt to measure isotope composition was made in 1934, when the level of stable oxygen isotopes was estimated in samples of Precambrian magnetite.[9] Later, it was discovered that the amount of heaviest isotope (^{18}O) in the atmosphere significantly exceeds initial laboratory measurements. Although the experiment was imprecise, it produced valuable insight regarding measurements in atmospheric chemistry.

With one isotope ^{18}O included in ozone formation, initial reaction (3) splits into two possible channels $^{16}O^{18}O+^{16}O$ and $^{16}O^{16}O + ^{18}O$. The energy difference between these channels is referred to as ΔZPE, related to the difference in the reactants' masses. The experiments conducted by Janssen et al.[10] in early 2000s measured reaction rates for each channel separately, revealing a strong correlation between ΔZPE and the reaction rates. The correlation between the relative reaction rate coefficients and the size of ΔZPE between the lower and upper pathways is called ζ-effect, quantitatively defined as:

$$\zeta = \frac{\kappa_{\text{lower}}}{\kappa_{\text{upper}}} \qquad (4)$$

The ζ-effect was estimated experimentally as $\zeta = 1.55$ and $\zeta = 1.63$ for the singly- and doubly-substituted ozone molecules, respectively.[11] Another discovery from the experiment was the distinction between symmetric ozone (ex. $^{16}O^{18}O^{16}O$) from asymmetric ozone ($^{16}O^{16}O^{18}O$). This effect is called η-effect; quantitatively is defined as:

$$\eta = \frac{\kappa_{\text{asym}}}{2\kappa_{\text{sym}}} \qquad (5)$$

where κ_{asym} and κ_{sym} are the reaction rate coefficients for the asymmetric and symmetric ozone species, respectively. Experimentally measured values of η-effect are nearly identical in both singly- and doubly-substituted case at approximately $\eta = 1.16$.[11]

Isotopes have been actively studied for over 70 years, changing our understanding of physical and organic chemistry, geo- and cosmochemistry, paleoclimatology, and hydrology.[12] In 1983, Thiemens and Heidenreich[13] were the first to experimentally demonstrate the existence of chemically produced mass-independent fractionation. Study of isotopes has also led to the development of experimental isotope ratio mass spectrometry, a breakthrough with a multitude of applications. Theories regarding the origin of the Solar System were developed using measurement and interpretation of the isotope record, made by observing ancient meteorites[13]. Evolution of Earth's Precambrian mixed oxygen/ozone atmosphere, resolution of greenhouse gas sources, aerosol chemistry and transport, paleoclimate, and history of Earth's oxidative capacity (paleo ozone levels), past atmosphere-regolith interactions on Mars have all been influenced by studying isotopes. Unfortunately, a comprehensive explanation of the isotope effect does not yet exist. Its origin remains a mystery, but progress is outlined in the work of Dr. Babikov's group.[14]

I-2. Recombination Mechanisms

There are several theoretical mechanisms that describe the formation of ozone molecule in the literature. Namely, the energy-transfer or Lindeman mechanism[3]:

$$O + O_2 \underset{\kappa_{dec}}{\overset{\kappa_{form}}{\rightleftarrows}} O_3^* \quad (6)$$

$$O_3^* + M \xrightarrow{\kappa_{stab}} O_3 + M \quad (7)$$

and radical-complex (or Chaperon) mechanism[15]:

$$O + M \leftrightarrow OM^* \quad (8)$$

$$OM^* + O_2 \rightarrow O_3 + M^* \quad (9)$$

where M denotes the bath gas.

The Lindemann mechanism is commonly used at the low and high pressure limits. It involves an intermediate metastable state. The first two reactions in (6) are described by formation rate coefficient κ_{form} and κ_{dec} decay rate coefficient in the chemical kinetic. The ratio of formation and decay is known as equilibrium constant $K_{eq} = \frac{\kappa_{form}}{\kappa_{dec}}$. The third step of Lindeman mechanism is described by $\kappa_{stab,}$ which is stabilization rate coefficient. The overall rate coefficient of Lindeman mechanism is also called the recombination rate coefficient κ_{rec} can be derived from master equation. The rate of ozone formation in Lindeman mechanism depends on concentration of three concentrations [O], [O_2], [M], thus the recombination rate coefficient is the 3^d order rate coefficient according to the kinetics theory.

In the experimental data of Troe et al.[16] showed the dependence of κ_{rec} recombination rate coefficient on pressure. In Figure 1 the κ_{rec} multiplied by [M] ($k' = k_{rec}$[M] is the 2nd order in respect to [O] and [O_2]) is plotted vs concentration of the bath gas (Ar in cm^{-3}).

At the lower pressure regime, all curves show linear dependence on bath concentration up to 1022 cm^{-3} then the curve at low temperature 163 K moves toward the plateau. Such behavior pattern can be derived from Lindeman mechanism considering limits of low and high pressures. If we consider low pressure limit - κ_{rec} remains the third order in respect to O, O_2 and M, meanwhile at the high pressure it becomes second order in respect to O and O_2. On the Figure 1 it appears as the linear dependence at low pressure, meanwhile closer to the high pressure region it shows the tendency towards the plateau. However, at the higher temperatures the behavior of the curves is unusual and cannot be explained in terms of basic Lindeman mechanism (circulation in the Figure 1).

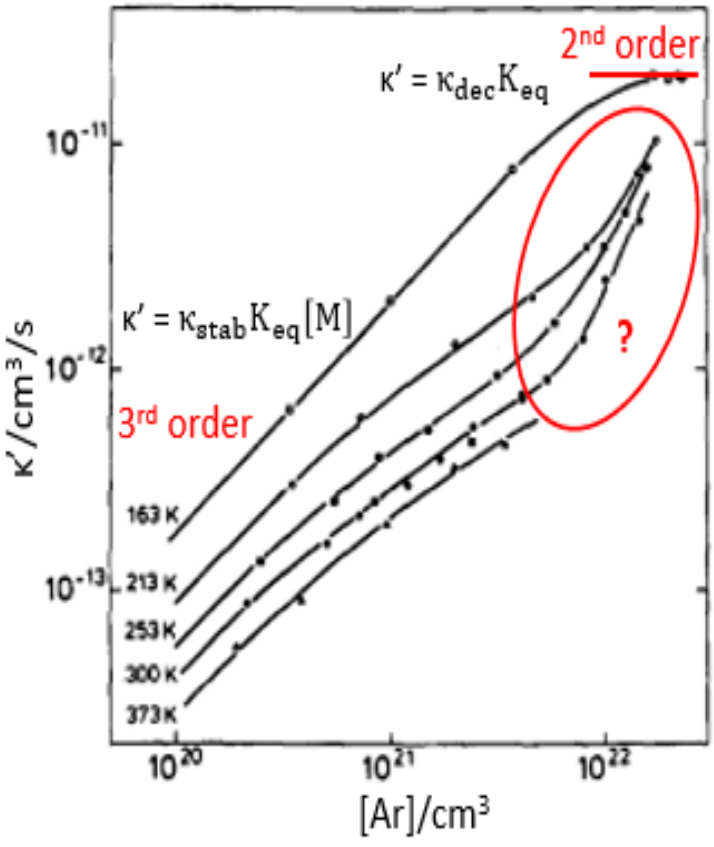

Figure 1. Pressure dependence of the recombination rate coefficient k_{rec} × [M], experimental data of Troe et al.[16] at several temperatures. The linear dependence corresponds to the second order rate coefficient k_{rec}. Plateau corresponds to the 3d order k_{rec}.

The alternative to Lindeman mechanism is known as Chaperon[17] mechanism or radical-complex mechanism. Chaperon mechanism consists of two steps just as Lindeman with intermediate metastable state, OM^*: $O + M \rightarrow OM^*$ and then $OM^* + O_2 \rightarrow O_3 + M$. In case of Lindeman mechanism intermediate metastable state O_3* is a highly excited molecule which stabilizes in covalent well by colliding with the other molecules of the bath gas. In Chaperon mechanism the radical complex is a weakly bound complex, unstable, especially at the high temperature.

In example of M. V. Ivanov and R. Schinke[18] the Chaperon mechanism was applied to description of ozone formation with Ar as the bath gas. The reaction of ozone recombination due to M. V. Ivanov and R. Schinke goes through two alternative channels

$$O + Ar \overset{K_1^{eq}}{\Longleftrightarrow} ArO^* + O_2 \overset{\kappa_1^{ex}}{\longrightarrow} O_3 + Ar,$$

$$O_2 + Ar \overset{K_2^{eq}}{\Longleftrightarrow} ArO_2{}^* + O \overset{\kappa_2^{ex}}{\longrightarrow} O_3 + Ar$$

The recombination rate coefficient in this case is given by:

$$k_{rec} = \frac{\left(k_1^{ex} K_1^{eq} + k_2^{ex} K_2^{eq}\right)}{1 + \left(K_1^{eq} + K_2^{eq}\right)[Ar]}$$

and in the low-pressure limit:

$$k_{rec} = \left(k_1^{ex} K_1^{eq} + k_2^{ex} K_2^{eq}\right)$$

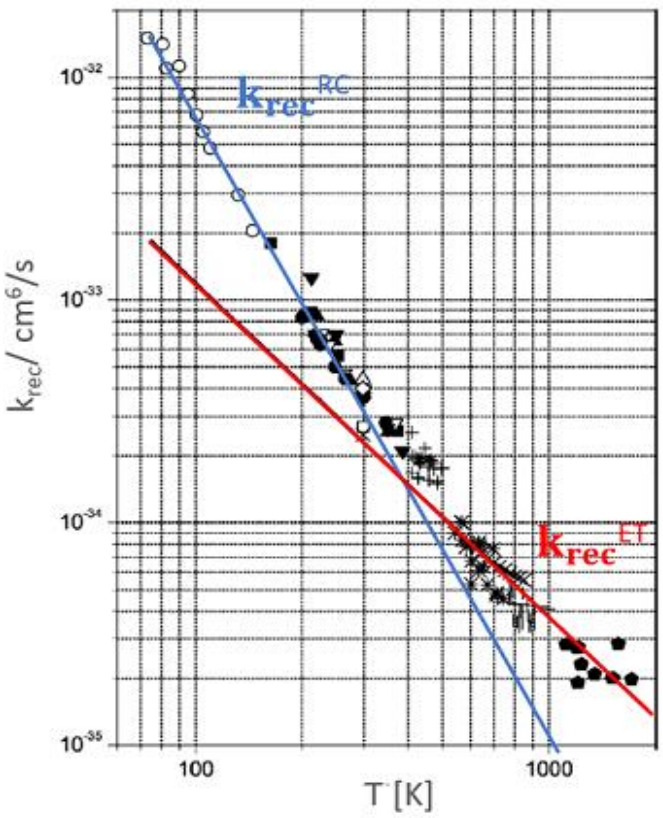

Figure 2. The fitting of experimental temperature dependence of recombination rate coefficient for ozone with Chaperon and Lindeman mechanisms with fitting Equations 7 and 8 accordingly.

Experimentally it was proven that the 2d channel is more efficient – $\kappa_2^{\text{ex}} \gg \kappa_1^{\text{ex}}$, it means κ_{rec} is determined by 2d channel. In the Figure 2 the experimental data for ozone of Luther was fitted by using both Lindeman and Chaperon mechanisms. It was found that about 40% of experimental data at the lower temperature correspond to Chaperon mechanism and only about 25% at the high temperature can be explain in terms of Chaperon in the Figure 2. It was assumed that Lindeman at higher temperature is more effective. Indeed, the Radical complex at high temperatures is not stable. Another example of application of these two competitive mechanisms to ozone formation was provided by K. Luther, K. Oum and J. Troe.[19]

Table 1. The contribution of Chaperon and Lindeman mechanism at different temperatures to ozone recombination.

T	Contribution of Chaperon mechanism	Contribution of Lindeman mechanism
100 K	83 %	17%
200 K	60 %	40%
300 K	42 %	58%
500 K	24 %	76%
1000 K	9 %	91%

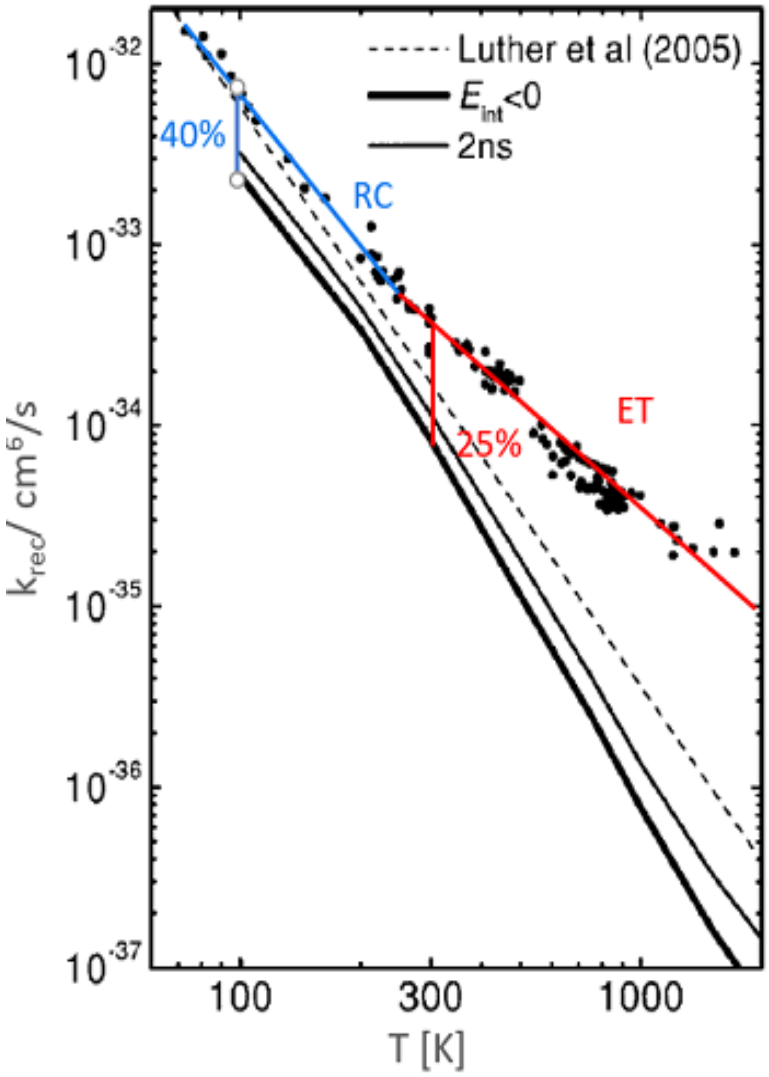

Figure 3. The temperature dependence of recombination rate coefficient. Dots are the experimental results. The lines correspond to the theoretical predictions with Chaperon mechanism. The closest coincidence with experiment lies in the area of low temperature. At the room temperature on 25% accounts for Chaperon mechanism. It assumed that alternative Lindeman mechanism dominates at the higher temperature.

Table 2. The efficiency of Lindeman and chaperon mechanisms at different temperature and pressure regimes.

	Low temperature	**Low pressure**	**High temperature**	**High pressure**
Chaperon	+	Lack of data	Low efficiency	Lack of data
Lindeman	Low efficiency	+	+	Low efficiency

The experimental points were fitted with curves corresponding to radical complex and energy transfer models as in the Figure 3. Fitting curve was estimated for Chaperon as:

$$k_{\mathrm{rec}}{}^{\mathrm{RC}} = 1.7 \times 10^{34}\,(\mathrm{T}/300)^{-3.2}\ \mathrm{cm}^6\ \mathrm{mol}^{-2}\ \mathrm{s}^{-1}$$

and for Lindeman:

$$k_{\mathrm{rec}}{}^{\mathrm{ET}} = 2.3 \times 10^{34}\,(\mathrm{T}/300)^{-1.5}\ \mathrm{cm}^6\ \mathrm{mol}^{-2}\ \mathrm{s}^{-1}$$

By analyzing the contribution of both mechanisms in recombination process at different temperatures it was concluded that at the room temperature both mechanisms contribute comparably. However, at the lower temperatures Radical Complex contributes more to the rate coefficient meanwhile at the higher temperatures Energy Transfer is highly dominant mechanism (see Table 1).

Both Lindeman and Chaperon mechanisms have the limitations can be represented as the Table 2. Chaperon mechanism describes low temperature behavior consistently, better than Lindeman mechanism. Lindeman mechanism describes behavior at the low pressure relatively accurate, however there is no data about Chaperon mechanism to compare at low pressure. Lindeman mechanism describes high temperature data better than Chaperon because the radical complex is especially unstable at the higher temperatures. In spite the availability of data about the Lindeman mechanism in the

literature, there is a gap in understanding the unconventional behavior of ozone at the high pressure regime.

I-3. Description of Quantum Resonances Using Stabilization Method

Metastable intermediate state is described by scattering resonance in quantum mechanics. Particularly, for description of ozone formation, scattering resonances can be calculated using stabilization method of Clary et al.[20] The application of this method is relatively straightforward. The stabilization approach implies the changes of energies as a functions of stabilization parameter (extension of the grid boundary, here – from 20.6 Bohr to 30.6 Bohr with a certain step). Stabilization approach implies that energies of the states above dissociation threshold decrease at a certain rate as we extend the grid boundary (see Figure 4). However, resonance energies are expected to be less dependent on the position of the grid boundary, so the decreasing rate in the resonance area becomes temporarily smaller which makes a second derivative of energy equal to zero (inflection points). Correspondingly, we can pinpoint a resonance energy by looking for points in which second derivative of energy becomes equal to zero.

Here (on the energy diagram of Figure 4) we consider three types of states – bound (the final ozone molecule O_3 – green lines) states, resonances (intermediate states O_3^* - red lines) and free particles (unbound O and O_2 molecules – black lines) and potential energy surface as the one-dimensional Morse oscillator[21] with grid from 0.6 to 20.6 Bohr (distance between the nucleuses). Energy states (eigenvalues) are showed as a

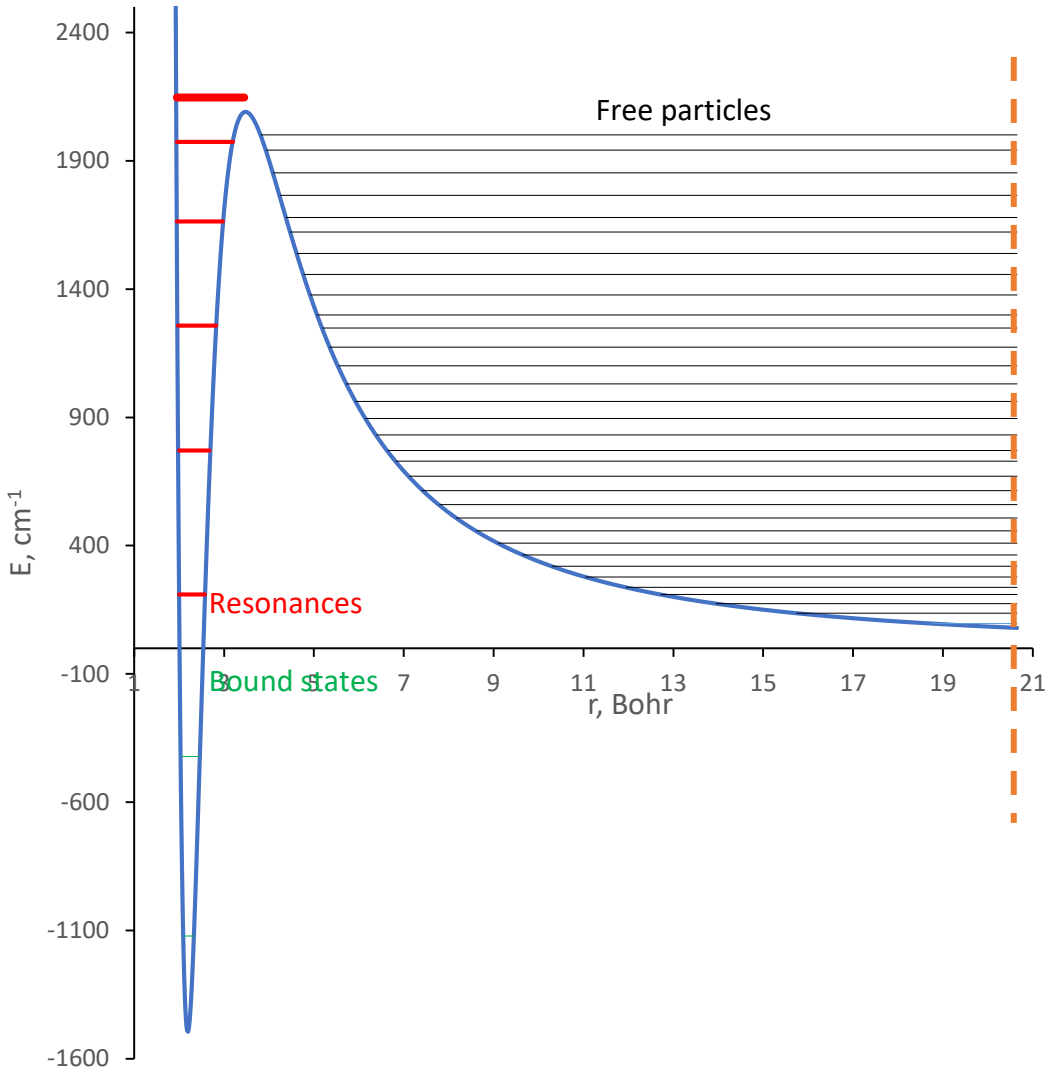

Figure 4. Energy diagram with one dimensional Morse potential with three types of states at J = 80. Green lines correspond to the bound states. Red lines correspond to the resonances and the rest are the free particle states. Orange line shows the boundary wall which was moved.

lines on energy diagram and gained from the numerical solution of Schrodinger equation.

The calculation of potential was done including centrifugal potential on equidistant grid and the final equation (blue curve):

$$V(r) = -D + D * (e^{(-a(r-r_e)-1)^2} + \frac{J(J+1)}{2\mu r^2}) \quad (10)$$

The states which are enclosed between the centrifugal barrier and repulsive wall (red lines in Figure 4) are resonance states. The resonance states are important for the research because they represent the metastable intermediate state O_3^*.

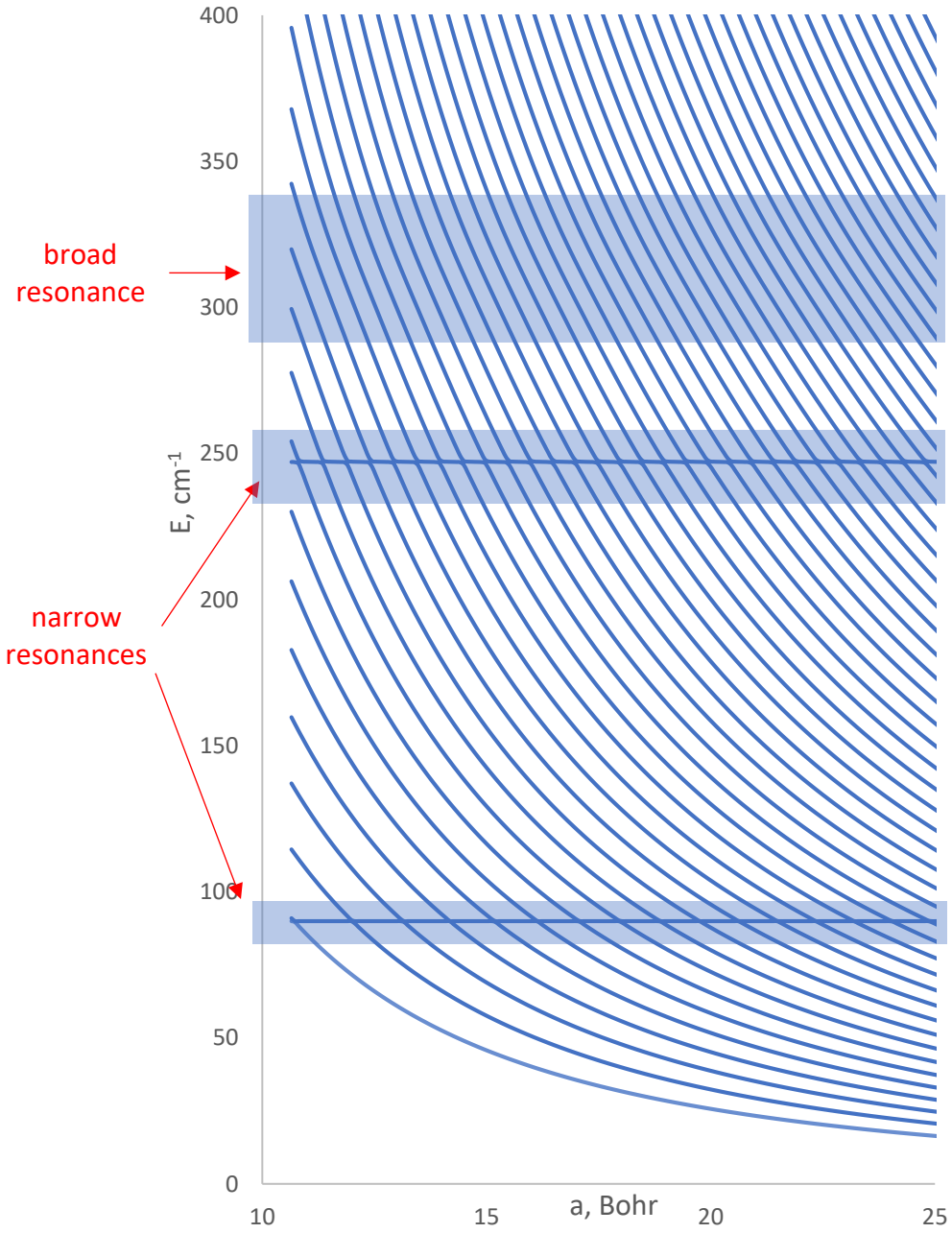

Figure 5. Diagram of $^{668}O_3$ isotope continua. Highlighted region underlines irregularly behavior and corresponds to resonance state from bottom to the top V = 12, 13, 14. First two states are distinguishable resonance narrow states, the third state is barely visible broad resonance.

If we know the energy of these states, we predict the rate of the ozone formation reaction. Then the right border of the grid was moved. The energies are gained from the numerical solution of Schrodinger equation (eigenvalues) and 200 times shifted to the right border of the greed. Two resonance states were visually detected within one *kT* (room temperature) energy region for J = 36 (rotational quantum number) and third one is barely visible (in the Figure 5).

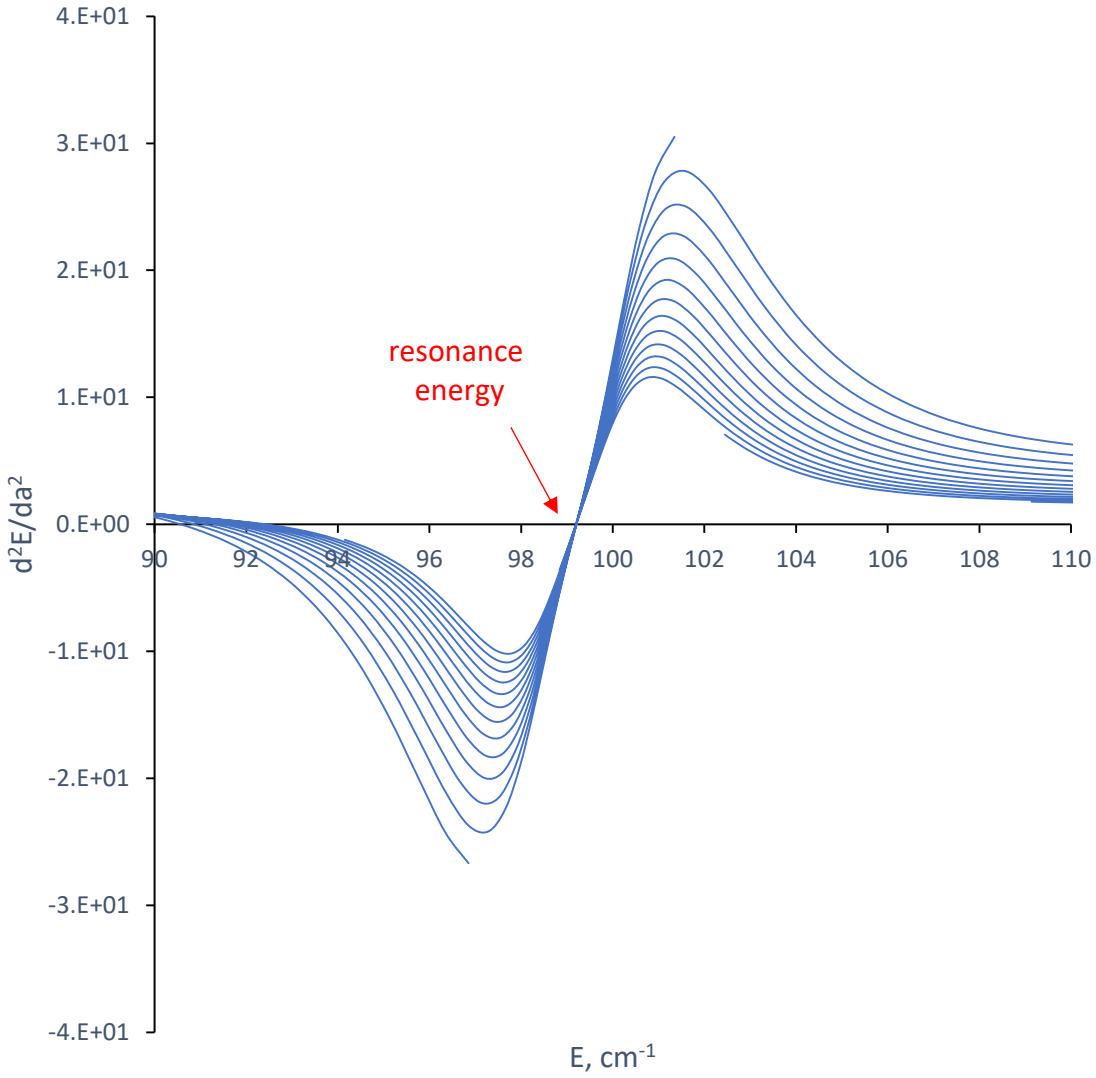

Figure 6. Second derivative of energies relative to extension of the grid boundary as a function of energies (J=24). Resonance energy corresponds intersection of x axis around 100 cm^{-1}.

Calculations were performed by extension of the grid boundary with the optimal step. Values of energies were plotted as a functions of stabilization parameter (a – optimal step, shift of the boundary). The narrow resonance energies are visible on the graph; however, the broad resonance energies look like barely noticeable curvature and is hard to define. It was assumed that by plotting the second derivative of resonance energy curves, it intersects the x axis in the resonance energies in Figure 6.

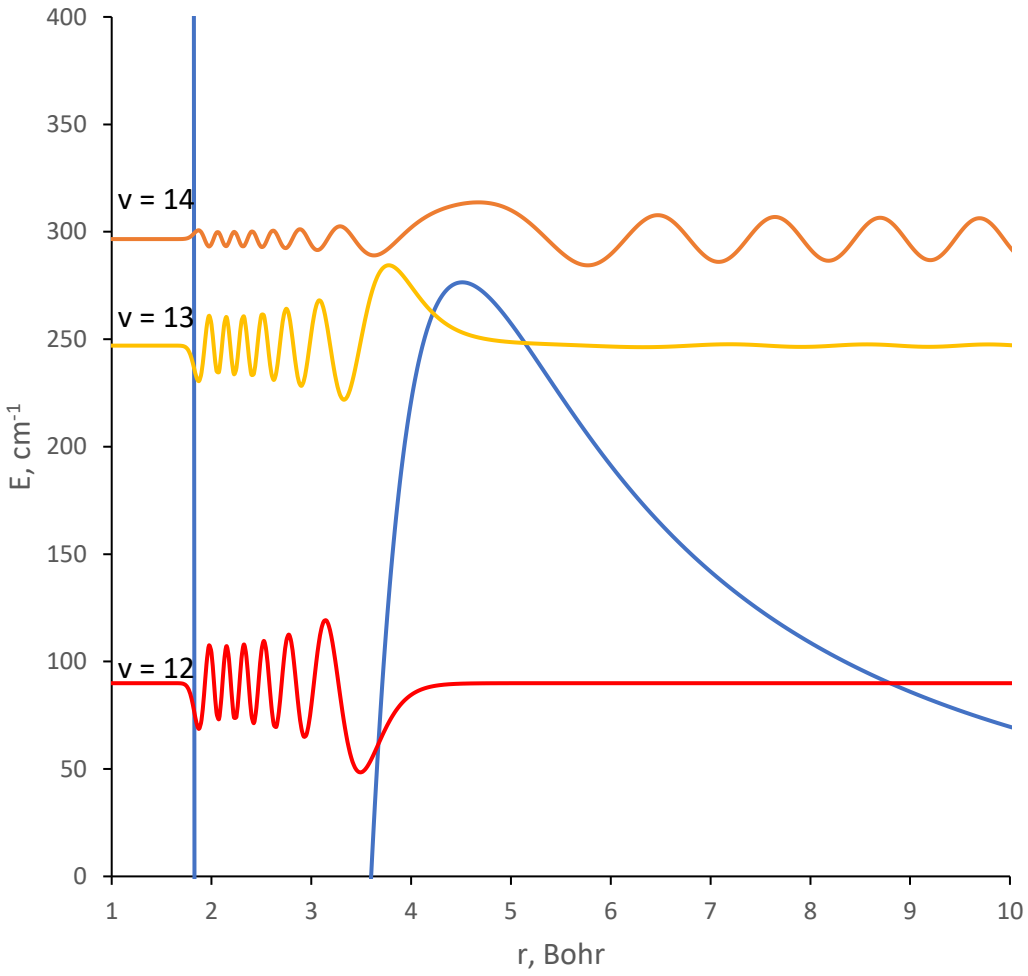

Figure 7. Wave functions for resonance states of $^{668}O_3$ isotopomer with potential energy curve. Three eigenfunctions are depicted with corresponding vibrational quantum numbers. Lower two are comparably narrow resonances under the rotational barrier, the last one is a broad resonance state above the barrier.

Indeed, in the Figure 6 the narrow resonance curves intersect the x-axis in the same point. Number of intersections increases as we increase J. J is the rotation quantum number, when it increases the rotational energy increases. For J = 36, three intersections were found. Roots were calculated with Newton's method. Example of the wavefunctions for determined eigenvalues are shown in the Figure 7.

I-4 Kinetics for Single Recombination Pathway

Consider example $^{18}O+^{16}O^{16}O \rightarrow ^{18}O^{16}O^{16}O$ with eigenvalues of resonance states the third-order recombination rate coefficient (κ_{rec}) can be calculated by using steady-state approximation (rate of intermediate metastable state formation ~ 0) and simplified kinetics model. The steady-state approximation approach will be explained in detail in the next chapter.

$$[O_3^*] = \frac{k^{\mathrm{form}}[O][O_2]}{k^{\mathrm{dec}} + k^{\mathrm{stab}}[M]} \tag{11}$$

$$\frac{d[O_3]}{dt} = k^{\mathrm{stab}}[O_3^*][M] = \frac{k^{\mathrm{stab}}k^{\mathrm{form}}[O][O_2][M]}{k^{\mathrm{dec}}+k^{\mathrm{stab}}[M]} \tag{12}$$

$$\kappa_{\mathrm{rec}} = \frac{k^{\mathrm{stab}}k^{\mathrm{form}}}{k^{\mathrm{dec}} + k^{\mathrm{stab}}[M]} \tag{13}$$

Stabilization rate coefficient k^{stab} is introduced for stabilization step and was computed using cross-section ($k^{\mathrm{stab}} \sim \sigma_{\mathrm{stab}}$ 154.03 a_0^2) [21]. Equilibrium constant is:

$$K^{\mathrm{eq}} = \frac{k^{\mathrm{form}}}{k^{\mathrm{dec}}} \tag{14}$$

$$k^{\mathrm{dec}} = \frac{\Gamma}{\hbar} \tag{15}$$

In this one-dimensional model the widths Γ^i of the scattering resonances (decay rates) are estimated analytically as a product of frequency ν_i and transmission probability

τ_i depicted in Figure 5. Frequency is the difference between two neighboring resonances state energies. Transmission probability τ_i is unitless parameter:

$$\tau_i = \frac{1}{1 + e^{-\frac{2\pi\delta E}{\omega^{\ddagger}}}} \tag{16}$$

Parameter τ_i has the limits - for broad resonance it equals approximately 1 and bound states it is about 0. Typically, resonances are trapped behind the centrifugal barrier ($\tau_i \approx \frac{1}{2}$) and are called "shape" resonances.[22]

The equilibrium constant K_{eq} corresponds to formation step and is calculated statistically for each separate resonance state from the partition ratio of metastable intermediates and reactants.

$$K_{\text{eq}}{}^{i} = \frac{Q_{\text{prod}}}{Q_{\text{react}}} = \frac{Q_{\text{2D}} Q_{\text{rovib}}}{Q_{\text{el}} Q_{\text{tr}} Q_{\text{rt}}} \tag{17}$$

$$Q_{el} = 3(5 + e^{\frac{-227.6}{\text{T}}} + e^{\frac{-325.9}{\text{T}}}) = 20.198 \tag{18}$$

$$Q_{\text{tr}} = \left(\frac{\mu k T}{2\pi\hbar}\right)^{\frac{3}{2}} = 0.346 * 10^{26} \frac{1}{\text{cm}^3} \tag{19}$$

$$Q_{\text{rt}} = \frac{kT}{B\hbar} = 153.9 \tag{20}$$

$$Q_{\text{rovib}} = (2J + 1)^2 e^{-\frac{E^i}{kT}} \tag{21}$$

Here, we split exponential factor to the product of two exponents ($E^i = \delta E^i + E^{\ddagger}$).

We introduced new moiety – the dynamical weight of a resonance. Weights determine the contribution of each resonance and introduce the pressure dependence, because it contains pressure of the bath gas [M].

$$w_i = \frac{\frac{\Gamma_i}{\hbar}}{\frac{\Gamma_i}{\hbar} + k_i^{\text{stab}}[\text{M}]} \tag{22}$$

At low pressure regime:

$k_i^{\text{stab}}[\text{M}] \ll \frac{\Gamma_i}{\hbar}$, weight → 1. At high pressure expression for weight transforms to:

$$w(\Gamma_i) = \frac{\frac{\Gamma^i}{\hbar}}{k_i^{\text{stab}}[\text{M}]} \tag{23}$$

With all that, the final Equation for the third-order recombination rate coefficient can be calculated using sums over vibrational and rotational excitations:

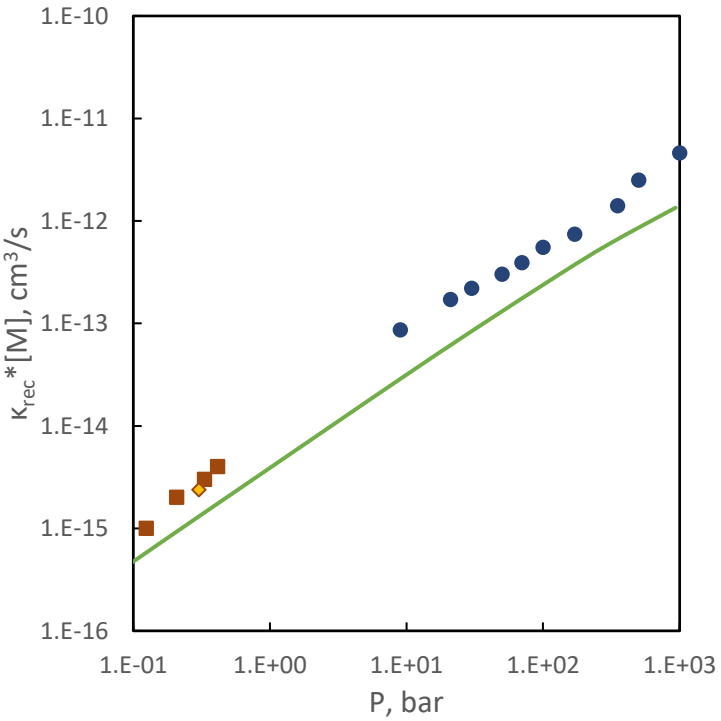

Figure 8. Pressure dependence of the second-order recombination rate coefficient $\kappa_{\text{rec}} \times$ [M]. Colored symbols depict experimental data. Green line is the result of the theoretical evaluation summarizes the 1D kinetic model.

$$k_{\mathrm{rec}} = \frac{Q_{2\mathrm{D}} k_{\mathrm{stab}}}{Q_{\mathrm{tr}} Q_{\mathrm{rot}} Q_{\mathrm{el}}} \sum_J (2J+1)^2 e^{-\frac{E_J^{\ddagger}}{kT}} \sum_v w_J^v e^{-\frac{\delta E_J^v}{kT}} \quad (24)$$

The third-order recombination coefficient was calculated. Absolute value of recombination coefficient was estimated as 20×10^{-35} cm^6/s and compared with experiment - 43×10^{-35} cm^6/s (orange symbol at Figure 8)[23,24] at 0.3 atm. Thereafter, the pressure dependence of recombination rate coefficient was studied by the change of [M] in the range starting from 0.1 atm. green line at Figure 8 corresponds to the one-dimensional model. The experimental data are provided by C. L. Lin and M. T. Leu[23] and J. Guenther, D. Krankowsky and K. Mauersberger[24]. The set of data at low temperature can be explained by energy-transfer mechanism. Simplified model seemed to be consistent with experiment, but many factors appeared to be responsible of anomalous behavior at the high-pressure limit. Some of them we study in the current research.

I-5. Objectives and the Structure of This Dissertation

The ultimate goal of dissertation is explanation of the mysterious mass-independent isotope effect. To achieve this, it is necessary to create as detailed theory, which takes into account all the properties of resonance states and reactants. The second chapter is dedicated to complex stabilization kinetic theory of ozone recombination. It covers the full description of the recombination reactions through all possible pathways including the insertion pathway previously not elucidated in the literature. The goal of the chapter to show the connection between variables and isotope effects. Especially important the connection between product-specific and channel-specific rates and isotope effects. The third chapter underlines the difference between singly- and doubly substituted isotopogues in terms of stabilization theory. It includes discussion of the way to analyze the temperature dependence of the rate coefficients from my theoretical

calculations and data from experimental work of Janssen's group. The goal is to identify the certain tendencies and correlations between the available experimental data and the theory. Fourth chapter is dedicated to discussion of experimental results and theoretical estimation. It starts with presentation the latest published theoretical data of Dr. Babikov's group, comparison with experiment. Then my theoretical data including the temperature dependence of kinetic variables is analyzed with proposed in third chapter approach. The last chapter establish the way to estimate the contribution of the certain states to the kinetic and isotope effects separately, though the example of resonance widths distribution to show the role of the certain states in the mysterious isotope effects. In early works, states only in the covalent well were investigated. Here I expand the approach and include the state in the van der Waals region and show their influence on kinetics and isotope effects.

CHAPTER II. FOUR ISOTOPICALLY LABELLED RECOMBINAETION PATHWAYS ON THE POTENTIAL ENERGY SURFACE OF OZONE

II-1. Introduction

Recombination process that forms the usual (isotopically unsubstituted) ozone molecules may look relatively simple, $O + O_2 \rightarrow O_3$, but this is only because one, the most abundant isotope of oxygen is involved, ^{16}O. When one rare isotope is introduced, say ^{18}O, several physically distinct reaction pathways can be identified[25]:

A: $$^{16}O + {}^{16}O^{18}O \rightarrow {}^{16}O^{16}O^{18}O \quad (25)$$

B: $$^{18}O + {}^{16}O^{16}O \rightarrow {}^{18}O^{16}O^{16}O \quad (26)$$

S: $$^{16}O + {}^{18}O^{16}O \rightarrow {}^{16}O^{18}O^{16}O \quad (27)$$

I: $$^{18}O + {}^{16}O^{16}O \rightarrow {}^{16}O^{18}O^{16}O \quad (28)$$

Two of these pathways, A and B, produce asymmetric ozone molecule $^{16}O^{16}O^{18}O$, while the other two, S and I, produce symmetric ozone molecule $^{16}O^{18}O^{16}O$. Three of them: A, B and S, correspond to the addition of an atom to a diatomic moiety (direct end-on processes), whereas the last one, I, represent the insertion of a rare isotope in-between the two atoms of the reagent molecule (and thus is expected to follow a more complicated indirect reaction path). If two ^{18}O isotopes are involved, then four more recombination pathways need to be considered:

A: $$^{18}O + {}^{16}O^{18}O \rightarrow {}^{16}O^{18}O^{18}O \quad (29)$$

B: $$^{16}O + {}^{18}O^{18}O \rightarrow {}^{16}O^{18}O^{18}O \quad (30)$$

S: $$^{18}O + {}^{16}O^{18}O \rightarrow {}^{18}O^{16}O^{18}O \quad (31)$$

I: $$^{16}O + {}^{18}O^{18}O \rightarrow {}^{18}O^{16}O^{18}O \quad (32)$$

with similar nomenclature, similar symmetry properties, and similar reaction mechanisms. However, as we will demonstrate further below, some properties of the reaction pathways (1-4) for singly substituted ozone molecules appear to be just opposite to those of pathways (5-8) for doubly substituted ozone molecules. The singly and doubly substituted molecules are said to represent two *isotopologues* of ozone.

Different isotopologues are relatively independent, in a sense that they can't interconvert one into another, although some of the reagents they use are the same: ^{16}O and ^{18}O atoms, and $^{16}O^{18}O$ diatomic. However, within each isotopologue the symmetric and asymmetric ozone molecules are closely related, since they can interconvert one into another, at least in principle, following some isomerization path through the potential energy surface, for example:

$$^{16}O^{16}O^{18}O \leftrightharpoons {}^{16}O^{18}O^{16}O \tag{33}$$

or

$$^{18}O\ {}^{16}O^{18}O \leftrightharpoons {}^{16}O^{18}O^{18}O \tag{34}$$

Therefore, symmetric, and asymmetric ozone molecules within the same isotopologue are called isotopomers. In Figure 9 a schematic of the potential energy surface is given for each isotopologue, with two isotopomers in each case, and four reaction pathways indicated. From this Figure 9 one can see that overall, on the global potential energy surface of a triatomic ozone molecule, there are three entrance channels, connected through six transition states to three potential energy wells. However, since two isotopes in each case are indistinguishable (two ^{16}O in the singly substituted isotopologue, or two ^{18}O in the doubly substituted isotopologue) there are only two distinguishable sets of reagents, and two distinguishable products, leading to four distinguishable reaction

pathways in each case: A, B and S and I, as introduced above. For the purpose of brevity, here and below, the notations "6" and "8" will be used to designate isotopes ^{16}O and ^{18}O respectively.

Experimental studies started by the Mauersberger group[2] and continued by Janssen and coworkers[10], gave us unique information about the magnitudes of recombination rate coefficients for the four pathways: κ_A, κ_B, κ_S and κ_I in both singly and doubly substituted cases. Experimentally measured rate coefficients indicate large and intricate isotope effects, with several definite isotope related phenomena, namely: quantum ΔZPE-effect, responsible for large difference, about 60%, between kA and k_B of

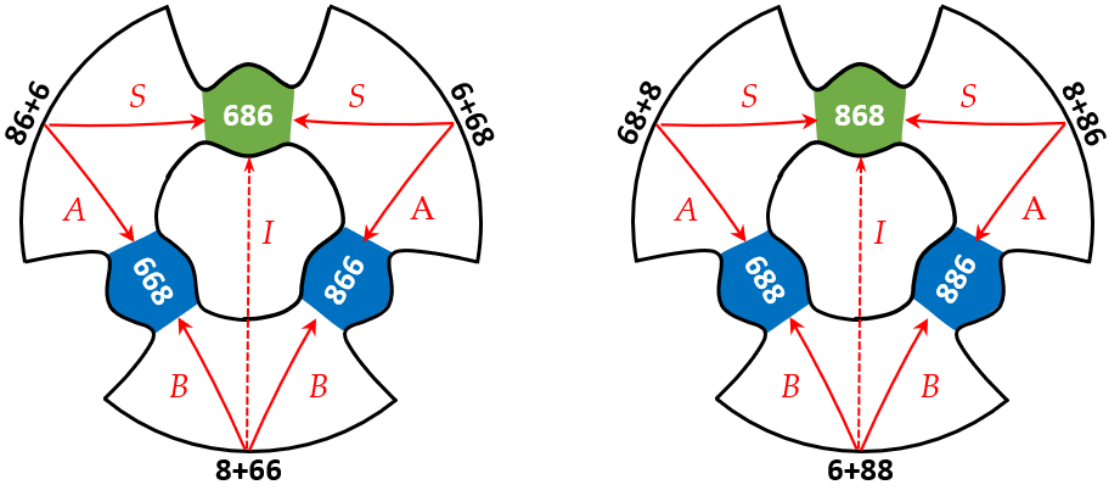

Figure 9. Schematic of the global PES of ozone that possesses a three-fold symmetry with respect to the entrance channels and product wells. The channels and wells are labeled for singly substituted (left) and doubly substituted (right) isotopologues. Reagents are indicated by black letters, the product ozone molecules by white letters. Four distinguishable reaction pathways are also indicated in each case, by red letters and arrows. The "insertion" pathway is shown schematically by the dashed arrow.

the pathways *A* and *B* that are just slightly endo/exothermic.[11]

1) symmetry-driven η-effect[26], that favors formation of asymmetric molecules, $^{16}O^{16}O^{18}O$ and $^{16}O^{18}O^{18}O$, compared to the symmetric once, $^{16}O^{18}O^{16}O$ and $^{18}O^{16}O^{18}O$, by about 16%.
2) very large difference, by a factor of ×5, between the insertion rate coefficients k_I in the singly and doubly substituted cases.[27]

The first two effects received a lot of attention from the theory community.[28] Large ΔZPE-effect was shown to originate from quantum mechanics[29] and thus is fundamentally important for our understanding of the chemical reaction rate laws in general. Nowadays this phenomenon is understood relatively well[28] and will naturally emerge as a part of the theory developed below. The symmetry-driven η-effect, practically important for atmospheric chemistry[12], remains mysterious, despite of significant efforts dedicated to finding its origin.[1] One of the goals of this work is to develop theoretical grounds for the description of this effect (although at present time we can't say that we understand it).

In sharp contrast with the first two phenomena, the third and the largest isotope effect, related to the insertion pathway in singly and doubly substituted isotopologues, has never been discussed in the literature. The rate coefficient κ_I of insertion has never been computed theoretically by anyone. One reason for this is that in the experiment the values of κ_I are smaller than those of κ_A, κ_B and κ_S, roughly, by two orders of magnitude[27], and therefore for theorists it is very tempting to neglect κ_I. But then the relevant isotope effect is also lost. In this work we develop a theory that includes all pathways of ozone formation, without neglecting anything a priory.

Another reason for the absence of any theoretical work on the insertion pathway is that this process is not a simple direct reaction. In the Figure 9 above, for simplicity, this process is shown by a straight arrow but, in reality, the reaction path can't cross the origin of this figure (at any relevant temperature) since the PES is extremely repulsive in that part of the configuration space. The insertion path must be indirect, akin to the roaming mechanism[27], when the reagents enter through one channel, form an excited complex in the adjacent well, then roam through the other channel, isomerizing into the other well, where the second complex is formed and finally stabilized by bath gas collisions. For example, in the case of singly substituted isotopologue this process can be represented as:

$$^{18}O + {}^{16}O^{16}O \rightarrow {}^{18}O\cdots{}^{16}O^{16}O \rightarrow {}^{18}O^{16}O\cdots{}^{16}O \xrightarrow{\text{roam}} {}^{16}O\cdots{}^{18}O^{16}O \xrightarrow{\text{stab}} {}^{16}O^{18}O^{16}O \quad (35)$$

In the doubly substituted case:

$$^{16}O + {}^{18}O^{18}O \rightarrow {}^{16}O\cdots{}^{18}O^{18}O \rightarrow {}^{16}O^{18}O\cdots{}^{18}O \xrightarrow{\text{roam}} {}^{18}O\cdots{}^{16}O^{18}O \xrightarrow{\text{stab}} {}^{18}O^{16}O^{18}O \quad (36)$$

How to describe these processes theoretically? Classical trajectories are used for the description of roaming,[27] but this approach is efficient and accurate only if roaming is the dominant mechanism of the reaction, or the only one possible. In the case of ozone, the insertion by roaming it is a minor pathway, with small probability. Prediction of rare events using classical trajectories is problematic on its own, and therefore is not expected to be helpful in the case of ozone. The quantum dynamics treatment, such as the wave packet method,[30] is usually employed for the description of direct reactions, which proceed through the transition state relatively fast, without formation of a long-lived complex. The propagation of wave packets through the extended parts of the potential

energy landscape, in particular over the deep wells where the long-lived complexes (scattering resonances) are formed, is numerically inefficient. Therefore, the quantum dynamical description of roaming is not routinely done.[27] It appears that all previously developed theoretical models of ozone formation either used an approximate treatment for scattering resonances or did not include the lifetimes at all, appealing to the low-pressure regime.[31]

II-2. Channel-Specific and Product-Specific Rate Coefficients

In this work, for theoretical description of the insertion process we employed a general time-independent quantum mechanical approach, in which the metastable ozone states above dissociation threshold are described by scattering resonances. Complex absorbing potential is introduced in the asymptotic part of the PES, and the widths of individual scattering resonances Γ_i are obtained from complex parts of the total energy, which are used to compute the decay rate coefficients (spontaneous, first order) of the individual resonances as:

$$k_i^{\mathrm{dec}} = \frac{\Gamma_i}{\hbar} \tag{37}$$

Importantly, within this approach, we can setup complex potential in the individual channels on the PES, in order to split the resonance width and the corresponding decay rate coefficient onto two channel-specific contributions:

$$\Gamma_i^{\mathrm{tot}} = \Gamma_i^{\mathrm{ch1}} + \Gamma_i^{\mathrm{ch2}} \tag{38}$$

$$k_i^{\mathrm{dec}} = k_i^{\mathrm{dec,ch1}} + k_i^{\mathrm{dec,ch2}} \tag{39}$$

Here $k_i^{\mathrm{dec,ch1}} = \Gamma_i^{\mathrm{ch1}}/\hbar$, whereas $k_i^{\mathrm{dec,ch2}} = \Gamma_i^{\mathrm{ch2}}/\hbar$. For example, in the singly substituted case $k_i^{\mathrm{dec,ch1}}$ corresponds to the decay of metastable ozone onto $^{18}O + {}^{16}O^{16}O$

through one channel at the bottom of Figure 9, while $k_i^{\mathrm{dec,ch2}}$ corresponds to the decay of a metastable ozone onto $^{16}O + {}^{16}O^{18}O$ through two indistinguishable channels at the top of Figure 9. Similar, in the doubly substituted case $k_i^{\mathrm{dec,ch1}}$ corresponds to the decay of ozone onto $^{16}O + {}^{18}O^{18}O$ through one channel at the bottom of Figure 9, while $k_i^{\mathrm{dec,ch2}}$ corresponds to the decay of a resonance onto $^{18}O + {}^{18}O^{16}O$ through two indistinguishable channels at the top of Figure 9. Using the equilibrium constant (computed statistically), the rate coefficients of *decay* can be converted into the rate coefficients for *formation* of the metastable ozone states. Note that this part of the method is based on rigorous quantum mechanical calculations.

The second component required for our theory is splitting the rate coefficients for *stabilization* of scattering resonances (second order, by collisions with bath gas) onto two components, those that produce symmetric and asymmetric ozone molecules. This is done semi-empirically, by assuming that stabilization rate coefficient for scattering resonance is proportional to the probability amplitude over certain arear of the PES. Namely, integrating the moduli squared of wavefunctions of the individual scattering resonances over the parts of the PES associated with symmetric and asymmetric ozone molecules[32], we can determine the product-specific probabilities p_i^{sym} and p_i^{asym}, and the total probability:

$$p_i^{\mathrm{tot}} = p_i^{\mathrm{sym}} + p_i^{\mathrm{asym}} \tag{40}$$

The two product-specific stabilization rate coefficients, and their total, are then computed as:

$$k_i^{\mathrm{stab}} = k^{\mathrm{stab}} p_i^{\mathrm{tot}}, \tag{41}$$

$$k_i^{\mathrm{stab}} = k^{\mathrm{stab}}\left(p_i^{\mathrm{sym}} + p_i^{\mathrm{asym}}\right) = k^{\mathrm{stab}} p_i^{\mathrm{sym}} + k^{\mathrm{stab}} p_i^{\mathrm{asym}}, \quad (42)$$

$$k_i^{\mathrm{stab,sym}} = k^{\mathrm{stab}} p_i^{\mathrm{sym}}, \quad (43)$$

$$k_i^{\mathrm{stab,asym}} = k^{\mathrm{stab}} p_i^{\mathrm{asym}} \quad (44)$$

$$k_i^{\mathrm{stab}} = k_i^{\mathrm{stab,sym}} + k_i^{\mathrm{stab,asym}}, \quad (45)$$

The values of probabilities p_i^{sym} and p_i^{asym} are rigorously determined for individual scattering resonances, by integrating their wave functions. In the singly substituted case p_i^{sym} and p_i^{asym} are associated with $^{16}O^{18}O^{16}O$ and $^{16}O^{16}O^{18}O$, while in the doubly substituted case they correspond to $^{18}O^{16}O^{18}O$ and $^{16}O^{18}O^{18}O$, respectively. One single value of $k^{\mathrm{stab}} = v\sigma_{\mathrm{stab}}$, where $v = \sqrt{8kT/(\pi\mu)}$, μ is reduced mass and σ_{stab} = 154.03 a_0^2 [21] is used for all resonances, as was recommended earlier in the mixed quantum/classical study of collisional energy transfer.[33]

Combination of the two channel-specific rate coefficients for decay of resonances, with two product-specific stabilization rate coefficients permits to express four pathway-specific recombination rate coefficients κ_{A}, κ_{B}, κ_{S} and κ_{I} through Γ_i^{ch1}, Γ_i^{ch2}, p_i^{sym} and p_i^{asym} (for each resonance). In addition, we will introduce and derive expressions for the channel specific recombination rate coefficients κ_{ch1} and κ_{ch2} for two physically distinguishable channels. Finally, we will operate with the product-specific recombination rate coefficients κ_{sym} and κ_{asym} for production of symmetric and asymmetric ozone molecules.

According to the Lindemann mechanism discussed in Chapter 1, the rate of a recombination process R is a product of the concentration of metastable species $[O_3^*]$

represented here by scattering resonances, the concentration of bath gas particles [M], and the stabilization rate coefficient k^{stab} (see Equation 46). If we assume that different resonances are populated and stabilized independently, the total rate is given by the sum over scattering resonances (labelled by index i):

$$R = \sum_i k_i^{\mathrm{stab}}[\mathrm{M}][\mathrm{O}_3^*]_i \tag{46}$$

Using Equation 42 this formula splits onto two contributions that correspond to the rates of production of symmetric and asymmetric ozone molecules, as follows:

$$\begin{aligned} R &= \sum_{\mathrm{i}} k^{\mathrm{stab}} (p_i^{\mathrm{sym}} + p_i^{\mathrm{asym}})[\mathrm{M}]\,[\mathrm{O}_3^*]_i \\ &= k^{\mathrm{stab}}[\mathrm{M}] \sum_i [\mathrm{O}_3^*]_i\, p_i^{\mathrm{sym}} + k^{\mathrm{stab}}[\mathrm{M}] \sum_i [\mathrm{O}_3^*]_i\, p_i^{\mathrm{asym}} \end{aligned} \tag{47}$$

If we define the corresponding rates as

$$R_{\mathrm{sym}} = k^{\mathrm{stab}}[\mathrm{M}] \sum_i [\mathrm{O}_3^*]_i\, p_i^{\mathrm{sym}} \tag{48}$$

$$R_{\mathrm{asym}} = k^{\mathrm{stab}}[\mathrm{M}] \sum_i [\mathrm{O}_3^*]_i\, p_i^{\mathrm{asym}} \tag{49}$$

then the total rate is simply the sum of two:

$$R_{\mathrm{tot}} = R_{\mathrm{sym}} + R_{\mathrm{asym}} \tag{50}$$

Note that sumation in Equations 48 and 49 goes trough all resonances, through exactly the same set of states in both Equation 48 and in Equation 49. What differentiates R_{sym} from R_{asym} are the values of stabilization provabilities defined for each state i: p_i^{sym} in Equation 48 vs. p_i^{asym} in Equation 49. Some states may contribute exclusively to R_{sym},

others exculsively to R_{asym}, while some resonances with delocalized wavefunctions may contribute to both R_{sym} and R_{asym} with sertain probabilities. Our description is general enough to incorporate all these cases.

II.3. Recombination Rate Expression for Single Substitution

Since two physically distinct reaction channels are present for each isotopologue, the concentration of metastable ozone species $[\mathrm{O}_3^*]$ is influenced by five processes indicated in the following Equation 51 (for the singly substituted case):

$$66 + 8 \underset{k^{\mathrm{dec,ch1}}}{\overset{k^{\mathrm{form,ch1}}}{\rightleftharpoons}} [668/686]^* \underset{k^{\mathrm{dec,ch2}}}{\overset{k^{\mathrm{form,ch2}}}{\rightleftharpoons}} 68 + 6 \qquad [668/686]^* \xrightarrow{k^{\mathrm{stab}}[\mathrm{M}]} \text{ozone} \tag{51}$$

This includes the processes of formation and decay through each channel, and the processes of stabilization by bath gas collisions into the stable symmetric and asymmetric ozone molecules. These processes can be accounted for as follows:

$$\begin{aligned}\frac{d[\mathrm{O}_3^*]_i}{dt} = {} & k_i^{\mathrm{form,ch1}}[66][8] + k_i^{\mathrm{form,ch2}}[68][6] - k_i^{\mathrm{dec,ch1}}[\mathrm{O}_3^*]_i \\ & - k_i^{\mathrm{dec,ch2}}[\mathrm{O}_3^*]_i - k_i^{\mathrm{stab,sym}}[\mathrm{M}][\mathrm{O}_3^*]_i - k_i^{\mathrm{stab,asym}}[\mathrm{M}][\mathrm{O}_3^*]_i\end{aligned} \tag{52}$$

Employing the steady state approximation, and, using Equations 39 and 45 for the total rates of decay and stabilization, we can write:

$$0 = k_i^{\mathrm{form,ch1}}[66][8] + k_i^{\mathrm{form,ch2}}[68][6] - k_i^{\mathrm{dec}}[\mathrm{O}_3^*]_i - k_i^{\mathrm{stab}}[\mathrm{M}][\mathrm{O}_3^*]_i \tag{53}$$

Solving for $[\mathrm{O}_3^*]_i$ we end up with expression for the steady state concentration of each metastable state:

$$[O_3^*]_i = \frac{k_i^{\text{form,ch1}}[66][8] + k_i^{\text{form,ch2}}[68][6]}{k_i^{\text{dec}} + k_i^{\text{stab}}[\text{M}]} \tag{54}$$

It is convenient to introduce, for each scattering resonance, the equilibrium constants for two reaction channels, as follows:

$$K_i^{\text{eq,ch1}} = \frac{k_i^{\text{form,ch1}}}{k_i^{\text{dec,ch1}}} \tag{55}$$

$$K_i^{\text{eq,ch2}} = \frac{k_i^{\text{form,ch2}}}{k_i^{\text{dec,ch2}}} \tag{56}$$

This permits to express concentration through the rates of decay only (that are fundamental properties of resonances, related to their widths):

$$[O_3^*]_i = \frac{k_i^{\text{dec,ch1}} K_i^{\text{eq,ch1}}}{k_i^{\text{dec}} + k_i^{\text{stab}}[\text{M}]}[66][8] + \frac{k_i^{\text{dec,ch2}} K_i^{\text{eq,ch2}}}{k_i^{\text{dec}} + k_i^{\text{stab}}[\text{M}]}[68][6] \tag{57}$$

Note that these are microcanonical equilibrium constants that do not include Boltzmann average over the states of ozone, but instead are introduced for every individual state of a product at given energy E_i of a resonance:

Calculations of the reagent partition functions for two channels, Q_{ch1} and Q_{ch2}, is

$$K_i^{\text{eq,ch1}} = \frac{(2J+1)\, e^{-E_i/kT}}{Q_{\text{ch1}}\, e^{-\Delta\text{ZPE}/kT}} \tag{58}$$

$$K_i^{\text{eq,ch2}} = \frac{(2J+1)\, e^{-E_i/kT}}{Q_{\text{ch2}}} \tag{59}$$

discussed in detail in Appendix. The factor $2J+1$ accounts for space degeneracy, related to the quantum number M_J of the symmetric-top rotor. One important element to discuss

is a factor $e^{-\Delta \mathrm{ZPE}/kT}$ in the denominator of the first of these expressions. Figure 10 is used to emphasize that the two reaction channels are not entirely exoergic.

Although electronic energies of the reagents in two channels are exactly the same, their vibrational zero-point energies are different. For example, in the singly substituted case, lower energy channel corresponds to the heavier diatomic $^{16}O^{18}O$, which defines threshold of the recombination process. Higher energy channel corresponds to the lighter diatomic $^{16}O^{16}O$. The difference of their vibrational zero-point energies is defined as (for single substitution):

$$\Delta \mathrm{ZPE} = \mathrm{ZPE}(66) - \mathrm{ZPE}(68) = 22.27 \mathrm{cm}^{-1}$$

Qualitatively, one may say that in the case of single isotopic substitution the Channel 1 is lifted above threshold, defined by the Channel 2, as shown in Figure 10. This energy difference, ΔZPE, enters our formalism through the expressions for the equilibrium constant of Channel 1.

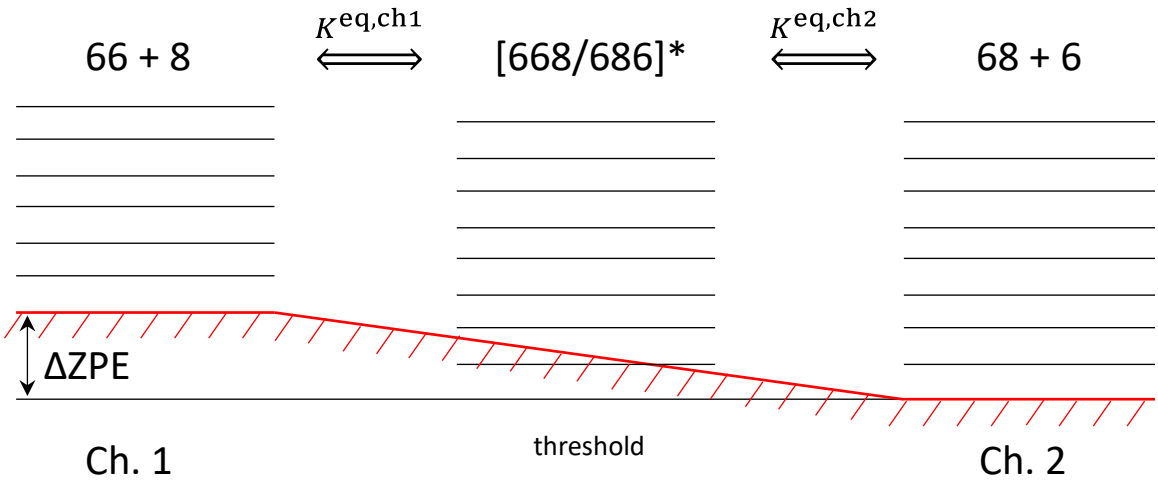

Figure 10. Two distinct channels of ozone formation (left and right) and the metastable ozone states (middle) in the case of singly isotopic substitution. Here "6" denotes ^{16}O whereas "8" denotes ^{18}O. Lower energy channel corresponds to the heavier diatomic reagent $^{16}O^{18}O$ with smaller zero-point energy. Upper channel corresponds to the lighter diatomic reagent $^{16}O^{16}O$. Energy difference of the two channels, ΔZPE, is indicated.

Putting together Equations 48-49 and 54-56, we obtain:

$$R_{\mathrm{sym}} = [\mathrm{M}][68][6]\frac{k^{\mathrm{stab}}}{Q_{\mathrm{ch2}}}\sum_i (2J+1)p_i^{\mathrm{sym}}\frac{\frac{\Gamma_i^{\mathrm{ch2}}}{\hbar}}{\frac{\Gamma_i^{\mathrm{tot}}}{\hbar}+k_i^{\mathrm{stab}}[\mathrm{M}]}e^{-\frac{E_i}{kT}} + [\mathrm{M}][66][8]\frac{k^{\mathrm{stab}}}{Q_{\mathrm{ch1}}}\sum_i (2J+1)p_i^{\mathrm{sym}}\frac{\frac{\Gamma_i^{\mathrm{ch1}}}{\hbar}}{\frac{\Gamma_i^{\mathrm{tot}}}{\hbar}+k_i^{\mathrm{stab}}[M]}e^{-\frac{E_i-\Delta\mathrm{ZPE}}{kT}} \quad (60)$$

$$R_{\mathrm{asym}} = [\mathrm{M}][68][6]\frac{k^{\mathrm{stab}}}{Q_{\mathrm{ch2}}}\sum_i (2J+1)p_i^{\mathrm{asym}}\frac{\frac{\Gamma_i^{\mathrm{ch2}}}{\hbar}}{\frac{\Gamma_i^{\mathrm{tot}}}{\hbar}+k_i^{\mathrm{stab}}[M]}e^{-\frac{E_i}{kT}} + [\mathrm{M}][66][8]\frac{k^{\mathrm{stab}}}{Q_{\mathrm{ch1}}}\sum_i (2J+1)p_i^{\mathrm{asym}}\frac{\frac{\Gamma_i^{\mathrm{ch1}}}{\hbar}}{\frac{\Gamma_i^{\mathrm{tot}}}{\hbar}+k_i^{\mathrm{stab}}[M]}e^{-\frac{E_i-\Delta\mathrm{ZPE}}{kT}} \quad (61)$$

Note that the term $e^{-\Delta\mathrm{ZPE}/kT}$ was moved to the numerator, to appear together with $\Gamma_i^{\mathrm{ch1}}/\hbar$. The reason behind this move is that the decay of resonances through Channel 1, given by $\Gamma_i^{\mathrm{ch1}}/\hbar$, is efficient only at energies above threshold for this channel, which is ΔZPE (see Figure 10). Therefore, it makes sense to measure energies of such resonances relative to the threshold of this channel, writing the Boltzmann factor as $e^{-(E_i-\Delta\mathrm{ZPE})/kT}$.

At this point it becomes clear that the two terms in Equation 60 for R_{sym} correspond to R_{S} and R_{I}, whereas the two terms in Equation 61 for R_{asym} correspond to R_{A} and R_{B}. This is because R_{S} and R_{A} correspond to the reagents in Channel 2, whereas R_{I} and R_{B} correspond to the reagents in Channel 1. But the Equations 60 and 61 are bulky. In order to make them more intuitive, we will introduce into the formalism several new handy moieties.

II.4. Kinetic Weight of a Resonance

The values of ratios in Equations 60-61 depend on the relative efficiencies of resonance formation, decay, and stabilization. It is convenient to name this moiety the dynamical weight of a resonance, or simply the *weight*. If there would be only one channel of resonance formation/decay, the expression for the weight would be:

$$w_i = \frac{\frac{\Gamma_i}{\hbar}}{\frac{\Gamma_i}{\hbar} + k_i^{\mathrm{stab}}[\mathrm{M}]} \tag{62}$$

In low-pressure limit, $k_i^{\mathrm{stab}}[\mathrm{M}] \ll \Gamma_i/\hbar$, the weight reaches its maximum value, $w_i \longrightarrow 1$, and the role of a resonance in the recombination process is maximized. In contrast, in the high-pressure limit, $k_i^{\mathrm{stab}}[\mathrm{M}] \gg \Gamma_i/\hbar$, the weight is $w_i \longrightarrow 0$, and the contribution of a resonance may be small.

At given finite pressure, different resonances have different weights, determined by their widths Γ_i. Broader resonances have larger weights, while narrower resonances have lower weights. One can consider a limiting case of a bound state with zero width, $\Gamma_i = 0$. Such states would have $w_i = 0$ at any pressure. This makes sense, the bound states do not decay spontaneously and are not formed directly from the reagents, making no contribution to the recombination process.

When multiple (in our case two) decay channels are present, one can still use Equation 62 to define the weight, but with the total width Γ_i^{tot} instead of Γ_i. This can be introduced into Equation 60-61 by factoring out the channel specific ratios $\Gamma_i^{\mathrm{ch1}}/\Gamma_i^{\mathrm{tot}}$ and $\Gamma_i^{\mathrm{ch2}}/\Gamma_i^{\mathrm{tot}}$ as we will demonstrate further below.

II.5. Dynamical Partition Function

Summation in Equations 60-61 goes over the metastable states of ozone, multiplied by Boltzmann factors and degeneracy factors, and thus very much resembles a partition function at the transition state, $Q^{\ddagger}$, used in the RRKM theory[34], except that our formula takes into account the processes of formation, decay, and stabilization of scattering resonances, and therefore are more general. Inspired by this similarity, we found it instructive to introduce the *dynamical partition functions*, $\tilde{Q}$, for four pathways of ozone formation, defined as follows:

$$\tilde{Q}_A \equiv \sum_i (2J+1)\, w_i \frac{\Gamma_i^{\mathrm{ch2}}}{\Gamma_i^{\mathrm{tot}}}\, p_i^{\mathrm{asym}}\, e^{-\frac{E_i}{kT}} \tag{63}$$

$$\tilde{Q}_B \equiv \sum_i (2J+1)\, w_i \frac{\Gamma_i^{\mathrm{ch1}}}{\Gamma_i^{\mathrm{tot}}}\, p_i^{\mathrm{asym}}\, e^{-\frac{E_i-\Delta\mathrm{ZPE}}{kT}} \tag{64}$$

$$\tilde{Q}_S \equiv \sum_i (2J+1)\, w_i \frac{\Gamma_i^{\mathrm{ch2}}}{\Gamma_i^{\mathrm{tot}}}\, p_i^{\mathrm{sym}} e^{-\frac{E_i}{kT}} \tag{65}$$

$$\tilde{Q}_I \equiv \sum_i (2J+1)\, w_i \frac{\Gamma_i^{\mathrm{ch1}}}{\Gamma_i^{\mathrm{tot}}}\, p_i^{\mathrm{sym}}\, e^{-\frac{E_i-\Delta\mathrm{ZPE}}{kT}} \tag{66}$$

Note that each factor in the definition of the dynamical partition function is unitless. Each $\tilde{Q}$ includes the degeneracy, the weight of a resonance (determined by the pressure of bath gas [M] and by the resonance width Γ_i^{tot}, see Equations 63-66 above, and the Boltzmann factor (including the ΔZPE shift for pathways *B* and *I* that originate in the upper Channel 1, see Figure 10). The values of $\tilde{Q}$ for four pathways are obtained from four combinations of the relative decay rate through one of two reagent channels (either $\Gamma_i^{\mathrm{ch1}}/\Gamma_i^{\mathrm{tot}}$ or $\Gamma_i^{\mathrm{ch2}}/\Gamma_i^{\mathrm{tot}}$) with two stabilization probabilities (either p_i^{sym} or p_i^{asym}).

II.6. Concise Rate Expressions

Now, the Equations 60-61 can be rewritten in a concise and intuitive form:

$$R_{\mathrm{sym}} = R_{\mathrm{S}} + R_{\mathrm{I}} \tag{67}$$

$$R_{\mathrm{asym}} = R_{\mathrm{A}} + R_{\mathrm{B}} \tag{68}$$

where the rates of recombination through four pathways were introduced as:

$$R_{\mathrm{A}} \equiv \kappa_{\mathrm{A}}[\mathrm{M}][68][6] \qquad R_{\mathrm{S}} \equiv \kappa_{\mathrm{S}}[\mathrm{M}][68][6] \tag{69), (70}$$

$$R_{\mathrm{B}} \equiv \kappa_{\mathrm{B}}[\mathrm{M}][66][8] \qquad R_{\mathrm{I}} \equiv \kappa_{\mathrm{I}}[\mathrm{M}][66][8] \tag{71), (72}$$

with four rate coefficients defined through four dynamical partition functions:

$$\kappa_{\mathrm{A}} \equiv k^{\mathrm{stab}} \frac{\tilde{Q}_{\mathrm{A}}}{Q_{\mathrm{ch2}}} \qquad \kappa_{\mathrm{S}} \equiv k^{\mathrm{stab}} \frac{\tilde{Q}_{\mathrm{S}}}{Q_{\mathrm{ch2}}} \tag{73), (74}$$

$$\kappa_{\mathrm{B}} \equiv k^{\mathrm{stab}} \frac{\tilde{Q}_{\mathrm{B}}}{Q_{\mathrm{ch1}}} \qquad \kappa_{\mathrm{I}} \equiv k^{\mathrm{stab}} \frac{\tilde{Q}_{\mathrm{I}}}{Q_{\mathrm{ch1}}} \tag{75), (76}$$

Note that each of these formulas has a simple intuitive form: recombination rate coefficient is a product of stabilization rate coefficient and the ratio of the partition functions for products over reagents. All complexity is absorbed by the dynamical partition functions of four recombination pathways: $\tilde{Q}_{\mathrm{A}}$, $\tilde{Q}_{\mathrm{B}}$, $\tilde{Q}_{\mathrm{S}}$, $\tilde{Q}_{\mathrm{I}}$.

II.7. Isotope Exchange

One has to realize that both R_{sym} and R_{asym} include contributions from two reaction channels with different reagents, [66][8] in Channel 1 and [68][6] in Channel 2, see Equations 69-72. Therefore, rate coefficient κ_{sym} is not a simple sum of κ_{S} and κ_{I}, and likewise κ_{asym} is not a simple sum of κ_{A} and κ_{B}. The following manipulations, however, permit to derive the needed expression:

$$R_{\mathrm{sym}} = R_{\mathrm{S}} + R_{\mathrm{I}} = \kappa_{\mathrm{S}}[\mathrm{M}][68][6] + \kappa_{\mathrm{I}}[\mathrm{M}][66][8]$$
$$= (\kappa_{\mathrm{S}} + \kappa_{\mathrm{I}}\frac{[66][8]}{[68][6]})[68][6][\mathrm{M}] = \kappa_{\mathrm{sym}}[68][6][\mathrm{M}] \quad (77)$$

$$R_{\mathrm{asym}} = R_{\mathrm{A}} + R_{\mathrm{B}} = \kappa_{\mathrm{A}}[\mathrm{M}][68][6] + \kappa_{\mathrm{B}}[\mathrm{M}][66][8]$$
$$= (\kappa_{\mathrm{A}} + \kappa_{\mathrm{B}}\frac{[66][8]}{[68][6]})[68][6][\mathrm{M}] = \kappa_{\mathrm{asym}}[68][6][\mathrm{M}] \quad (78)$$

In this approach the contributions of two reaction channels are added together, by re-expressing the two rates through the concentrations of reagents in the lowest energy channel (Channel 2 in the singly substituted case).

Note that the ratio of four concentrations in these expressions represents the equilibrium constant for isotope exchange between the two channels, with forward direction defined to be from Channel 2 to Channel 1:

$$68 + 6 \rightleftharpoons 66 + 8 \quad (79)$$

$$K^{\mathrm{ex}} = \frac{[66][8]}{[68][6]} = \frac{Q_{\mathrm{ch1}}e^{-\Delta\mathrm{ZPE}/kT}}{Q_{\mathrm{ch2}}} \quad (80)$$

The value of this equilibrium constant is expected to be on the order of 1/2 due to symmetry of the homonuclear diatomic reagent in the Channel 1, in which every other rotational state is forbidden by symmetry.

With this definition, the expressions for product-specific recombination rate coefficients are:

$$\kappa_{\mathrm{sym}} \equiv \kappa_{\mathrm{S}} + \kappa_{\mathrm{I}}K^{\mathrm{ex}} \quad (81)$$

$$\kappa_{\mathrm{asym}} \equiv \kappa_{\mathrm{A}} + \kappa_{\mathrm{B}}K^{\mathrm{ex}} \quad (82)$$

Indeed, neither of these expressions is a simple sum. The isotope exchange constant K^{ex} enters these expressions, multiplying the rate constant for upper channel.

II-8 Product Specific Recombination Rate Coefficients

Substitution of Equations 73-76 for four rate constants into Equations 81-82 permits to obtain the following expressions:

$$\kappa_{\mathrm{sym}} = k^{\mathrm{stab}} \frac{\tilde{Q}_{\mathrm{S}}}{Q_{\mathrm{ch2}}} + k^{\mathrm{stab}} \frac{\tilde{Q}_{\mathrm{I}}}{Q_{\mathrm{ch1}}} \frac{Q_{\mathrm{ch1}} e^{-\frac{\Delta \mathrm{ZPE}}{kT}}}{Q_{\mathrm{ch2}}} = k^{\mathrm{stab}} \frac{\tilde{Q}_{\mathrm{S}} + \tilde{Q}_{\mathrm{I}} e^{-\frac{\Delta \mathrm{ZPE}}{kT}}}{Q_{\mathrm{ch2}}} \qquad (83)$$

$$\kappa_{\mathrm{asym}} = k^{\mathrm{stab}} \frac{\tilde{Q}_{\mathrm{A}}}{Q_{\mathrm{ch2}}} + k^{\mathrm{stab}} \frac{\tilde{Q}_{\mathrm{B}}}{Q_{\mathrm{ch1}}} \frac{Q_{\mathrm{ch1}} e^{-\frac{\Delta \mathrm{ZPE}}{kT}}}{Q_{\mathrm{ch2}}} = k^{\mathrm{stab}} \frac{\tilde{Q}_{\mathrm{A}} + \tilde{Q}_{\mathrm{B}} e^{-\frac{\Delta \mathrm{ZPE}}{kT}}}{Q_{\mathrm{ch2}}} \qquad (84)$$

These expressions suggest that the dynamical partition functions for the formation of symmetric and asymmetric ozone molecules can be defined as:

$$\tilde{Q}_{\mathrm{sym}} \equiv \tilde{Q}_{\mathrm{S}} + \tilde{Q}_{\mathrm{I}} e^{-\frac{\Delta \mathrm{ZPE}}{kT}} \qquad \tilde{Q}_{\mathrm{asym}} \equiv \tilde{Q}_{\mathrm{A}} + \tilde{Q}_{\mathrm{B}} e^{-\frac{\Delta \mathrm{ZPE}}{kT}} \qquad (85), (86)$$

Then:

$$\kappa_{\mathrm{sym}} \equiv k^{\mathrm{stab}} \frac{\tilde{Q}_{\mathrm{sym}}}{Q_{\mathrm{ch2}}} \qquad \kappa_{\mathrm{asym}} \equiv k^{\mathrm{stab}} \frac{\tilde{Q}_{\mathrm{asym}}}{Q_{\mathrm{ch2}}} \qquad (87), (88)$$

Note that κ_{sym} and κ_{asym} use the same reference channel, namely, the lower energy Channel 2, so the partition function of this channel, Q_{ch2}, shows up in the denominator of both expressions. Also note, that in $\tilde{Q}_{\mathrm{sym}}$ or $\tilde{Q}_{\mathrm{asym}}$ the two contributions come not as a simple sum; the contribution of the upper channel is multiplied by $e^{-\Delta \mathrm{ZPE}/kT}$.

It is instructive to express $\tilde{Q}_{\mathrm{sym}}$ and $\tilde{Q}_{\mathrm{asym}}$ through the properties of individual resonances. Substitution of Equations 38-41 into 60-61 gives us:

$$\tilde{Q}_{\mathrm{sym}} = \sum_i (2J+1)\, w_i \frac{\Gamma_i^{\mathrm{ch2}}}{\Gamma_i^{\mathrm{tot}}}\, p_i^{\mathrm{sym}} e^{-\frac{E_i}{kT}} + e^{-\frac{\Delta\mathrm{ZPE}}{kT}} \sum_i (2J+1)\, w_i \frac{\Gamma_i^{\mathrm{ch1}}}{\Gamma_i^{\mathrm{tot}}}\, p_i^{\mathrm{sym}} e^{-\frac{E_i - \Delta\mathrm{ZPE}}{kT}} \quad (89)$$

$$= \sum_i (2J+1)\, w_i\, p_i^{\mathrm{sym}}\, e^{-\frac{E_i}{kT}};$$

$$\tilde{Q}_{\mathrm{asym}} = \sum_i (2J+1)\, w_i \frac{\Gamma_i^{\mathrm{ch2}}}{\Gamma_i^{\mathrm{tot}}}\, p_i^{\mathrm{asym}} e^{-\frac{E_i}{kT}} + e^{-\frac{\Delta\mathrm{ZPE}}{kT}} \sum_i (2J+1)\, w_i \frac{\Gamma_i^{\mathrm{ch1}}}{\Gamma_i^{\mathrm{tot}}}\, p_i^{\mathrm{asym}} e^{-\frac{E_i - \Delta\mathrm{ZPE}}{kT}} \quad (90)$$

$$= \sum_i (2J+1)\, w_i\, p_i^{\mathrm{asym}}\, e^{-\frac{E_i}{kT}}.$$

This result is very interesting, since several moieties disappeared in the final expressions for $\tilde{Q}_{\mathrm{sym}}$ and $\tilde{Q}_{\mathrm{asym}}$. First, all ΔZPE factors cancel analytically. Then, two contributions to the total width, Γ_i^{ch1} and Γ_i^{ch2}, added up and cancelled with Γ_i^{tot}. This means that, for the description of symmetry driven isotope effects, the widths (lifetimes) of scattering resonances are not important. They still enter the weight w_i, but the same weights enter $\tilde{Q}_{\mathrm{sym}}$ and $\tilde{Q}_{\mathrm{asym}}$. The only difference between $\tilde{Q}_{\mathrm{sym}}$ and $\tilde{Q}_{\mathrm{asym}}$ comes from stabilization probabilities, p_i^{sym} vs. p_i^{asym}.

II-9 Channel Specific Recombination Rate Coefficients

Since $R_{\mathrm{tot}} = R_{\mathrm{A}} + R_{\mathrm{B}} + R_{\mathrm{S}} + R_{\mathrm{I}}$, we can regroup the four contributions into two rates that correspond to two entrance channels:

$$R_{\mathrm{ch1}} = R_{\mathrm{A}} + R_{\mathrm{S}} \quad (91)$$

$$R_{\mathrm{ch2}} = R_{\mathrm{B}} + R_{\mathrm{I}} \quad (92)$$

Using the definitions of Equations 69-72 one immediately obtains expressions for the corresponding rate coefficients:

$$\kappa_{\mathrm{ch1}} = \kappa_{\mathrm{B}} + \kappa_{\mathrm{I}} = k^{\mathrm{stab}} \frac{\tilde{Q}_{\mathrm{B}} + \tilde{Q}_{\mathrm{I}}}{Q_{\mathrm{ch1}}} \tag{93}$$

$$\kappa_{\mathrm{ch2}} = \kappa_{\mathrm{A}} + \kappa_{\mathrm{S}} = k^{\mathrm{stab}} \frac{\tilde{Q}_{\mathrm{A}} + \tilde{Q}_{\mathrm{S}}}{Q_{\mathrm{ch2}}} \tag{94}$$

Two dynamical partition functions for these processes can be defined as a simple sum:

$$\tilde{Q}_{\mathrm{ch1}} \equiv \tilde{Q}_{\mathrm{B}} + \tilde{Q}_{\mathrm{I}} \tag{95}$$

$$\tilde{Q}_{\mathrm{ch2}} \equiv \tilde{Q}_{\mathrm{A}} + \tilde{Q}_{\mathrm{S}} \tag{96}$$

Using Equation 63-66 we obtain the following expressions (through properties of the individual resonances):

$$\tilde{Q}_{\mathrm{ch1}} \equiv \sum_i (2J+1)\, w_i \frac{\Gamma_i^{\mathrm{ch1}}}{\Gamma_i^{\mathrm{tot}}}\, p_i^{\mathrm{tot}}\, e^{-\frac{E_i - \Delta\mathrm{ZPE}}{kT}} \tag{97}$$

$$\tilde{Q}_{\mathrm{ch2}} \equiv \sum_i (2J+1)\, w_i \frac{\Gamma_i^{\mathrm{ch2}}}{\Gamma_i^{\mathrm{tot}}}\, p_i^{\mathrm{tot}}\, e^{-\frac{E_i}{kT}} \tag{98}$$

This result is also quite interesting. These expressions indicate that the splitting of p_i^{tot} onto p_i^{sym} and p_i^{asym} has no influence on $\tilde{Q}_{\mathrm{ch1}}$ vs. $\tilde{Q}_{\mathrm{ch2}}$ since the same overall stabilization probability enters both expressions. In this case the difference between $\tilde{Q}_{\mathrm{ch1}}$ and $\tilde{Q}_{\mathrm{ch2}}$ comes entirely from splitting of Γ_i^{tot} onto Γ_i^{ch1} and Γ_i^{ch2}, for individual resonances. In this procedure, Γ_i^{ch1} comes with the ΔZPE sift of energy reference, as emphasized above.

II-10 Zero-Pressure vs. High-Pressure Limits

Low-pressure limit is relevant to the atmospheric chemistry, to some laboratory studies, but is also important methodologically. In the limit of zero pressure of bath gas,

$[\mathrm{M}] = 0$, the weights of all resonances achieve their maximum value $w_i = 1$, which simplifies the equations as follows. All Equations from the summary transform accordingly.

$$\tilde{Q}^{\circ}_{\mathrm{tot}} = \sum_i (2J+1)\, p_i^{\mathrm{tot}}\, e^{-\frac{E_i}{kT}} \tag{99}$$

$$\tilde{Q}^{\circ}_{\mathrm{sym}} = \sum_i (2J+1)\, p_i^{\mathrm{sym}}\, e^{-\frac{E_i}{kT}} \tag{100}$$

$$\tilde{Q}^{\circ}_{\mathrm{asym}} = \sum_i (2J+1)\, p_i^{\mathrm{asym}}\, e^{-\frac{E_i}{kT}} \tag{101}$$

$$\tilde{Q}^{\circ}_{\mathrm{ch1}} = \sum_i (2J+1)\, \frac{\Gamma_i^{\mathrm{ch1}}}{\Gamma_i^{\mathrm{tot}}}\, p_i^{\mathrm{tot}}\, e^{-\frac{E_i - \Delta\mathrm{ZPE}}{kT}} \tag{102}$$

$$\tilde{Q}^{\circ}_{\mathrm{ch2}} = \sum_i (2J+1)\, \frac{\Gamma_i^{\mathrm{ch2}}}{\Gamma_i^{\mathrm{tot}}}\, p_i^{\mathrm{tot}}\, e^{-\frac{E_i}{kT}} \tag{103}$$

$$\tilde{Q}^{\circ}_{\mathrm{A}} = \sum_i (2J+1) \frac{\Gamma_i^{\mathrm{ch2}}}{\Gamma_i^{\mathrm{tot}}}\, p_i^{\mathrm{asym}}\, e^{-\frac{E_i}{kT}} \tag{104}$$

$$\tilde{Q}^{\circ}_{\mathrm{B}} = \sum_i (2J+1)\, \frac{\Gamma_i^{\mathrm{ch1}}}{\Gamma_i^{\mathrm{tot}}} p_i^{\mathrm{asym}} e^{-\frac{E_i - \Delta\mathrm{ZPE}}{kT}} \tag{105}$$

$$\tilde{Q}^{\circ}_{\mathrm{S}} = \sum_i (2J+1)\, \frac{\Gamma_i^{\mathrm{ch2}}}{\Gamma_i^{\mathrm{tot}}} p_i^{\mathrm{sym}} e^{-\frac{E_i}{kT}} \tag{106}$$

$$\tilde{Q}^{\circ}_{\mathrm{I}} = \sum_i (2J+1) \frac{\Gamma_i^{\mathrm{ch1}}}{\Gamma_i^{\mathrm{tot}}} p_i^{\mathrm{sym}}\, e^{-\frac{E_i - \Delta\mathrm{ZPE}}{kT}} \tag{107}$$

An important point to emphasize is that $\tilde{Q}^{\circ}_{\mathrm{tot}}$, $\tilde{Q}^{\circ}_{\mathrm{sym}}$ and $\tilde{Q}^{\circ}_{\mathrm{asym}}$ do not include the widths of resonances, at all. Therefore, in the limit of zero-pressure any isotope effects in symmetric vs. asymmetric ozone molecules driven by resonance width (lifetimes of the

metastable states) are expected to disappear. The expressions for $\tilde{Q}^{\circ}_{\mathrm{ch1}}$, $\tilde{Q}^{\circ}_{\mathrm{ch2}}$, $\tilde{Q}^{\circ}_{\mathrm{A}}$, $\tilde{Q}^{\circ}_{\mathrm{B}}$, $\tilde{Q}^{\circ}_{\mathrm{S}}$ and $\tilde{Q}^{\circ}_{\mathrm{I}}$ still contain resonance widths, but only in the relative ratios $\Gamma_i^{\mathrm{ch1}}/\Gamma_i^{\mathrm{tot}}$ and $\Gamma_i^{\mathrm{ch2}}/\Gamma_i^{\mathrm{tot}}$. Therefore, the absolute values of widths do not really matter. What remains important is a partition (splitting) of Γ_i^{tot} between the two reaction channels.

In the high-pressure limit [M] $\rightarrow \infty$ the resonance weight decreases as a function of pressure and increases as a function of width:

$$w_i \approx \frac{\frac{\Gamma_i^{\mathrm{tot}}}{\hbar}}{k_i^{\mathrm{stab}}[\mathrm{M}]} \tag{108}$$

This leads to the following expressions:

$$\tilde{Q}^{\infty}_{\mathrm{tot}} = \sum_i (2J+1)\frac{\Gamma_i^{\mathrm{tot}}}{\hbar k^{\mathrm{stab}}[\mathrm{M}]}\, e^{-\frac{E_i}{kT}} \tag{109}$$

$$\tilde{Q}^{\infty}_{\mathrm{sym}} = \sum_i (2J+1)\frac{\Gamma_i^{\mathrm{tot}}}{\hbar k^{\mathrm{stab}}[\mathrm{M}]}\frac{p_i^{\mathrm{sym}}}{p_i^{\mathrm{tot}}}\, e^{-\frac{E_i}{kT}} \tag{110}$$

$$\tilde{Q}^{\infty}_{\mathrm{asym}} = \sum_i (2J+1)\frac{\Gamma_i^{\mathrm{tot}}}{\hbar k^{\mathrm{stab}}[\mathrm{M}]}\frac{p_i^{\mathrm{asym}}}{p_i^{\mathrm{tot}}}\, e^{-\frac{E_i}{kT}} \tag{111}$$

$$\tilde{Q}^{\infty}_{\mathrm{ch1}} = \sum_i (2J+1)\,\frac{\Gamma_i^{\mathrm{ch1}}}{\hbar k^{\mathrm{stab}}[\mathrm{M}]}\, e^{-\frac{E_i - \Delta\mathrm{ZPE}}{kT}} \tag{112}$$

$$\tilde{Q}^{\infty}_{\mathrm{ch2}} = \sum_i (2J+1)\,\frac{\Gamma_i^{\mathrm{ch2}}}{\hbar k^{\mathrm{stab}}[\mathrm{M}]}\, e^{-\frac{E_i}{kT}} \tag{113}$$

$$\tilde{Q}^{\infty}_{\mathrm{A}} = \sum_i (2J+1)\frac{\Gamma_i^{\mathrm{ch2}}}{\hbar k^{\mathrm{stab}}[\mathrm{M}]}\frac{p_i^{\mathrm{asym}}}{p_i^{\mathrm{tot}}} e^{-\frac{E_i}{kT}} \tag{114}$$

$$\tilde{Q}^{\infty}_{\mathrm{B}} = \sum_i (2J+1)\frac{\Gamma_i^{\mathrm{ch1}}}{\hbar k^{\mathrm{stab}}[\mathrm{M}]}\frac{p_i^{\mathrm{asym}}}{p_i^{\mathrm{tot}}} e^{-\frac{E_i - \Delta\mathrm{ZPE}}{kT}} \tag{115}$$

$$\tilde{Q}_{\mathrm{S}}^{\infty} = \sum_i (2J+1) \frac{\Gamma_i^{\mathrm{ch2}}}{\hbar k^{\mathrm{stab}}[\mathrm{M}]} \frac{p_i^{\mathrm{sym}}}{p_i^{\mathrm{tot}}} e^{-\frac{E_i}{kT}} \tag{116}$$

$$\tilde{Q}_{\mathrm{I}}^{\infty} = \sum_i (2J+1) \frac{\Gamma_i^{\mathrm{ch1}}}{\hbar k^{\mathrm{stab}}[\mathrm{M}]} \frac{p_i^{\mathrm{sym}}}{p_i^{\mathrm{tot}}} e^{-\frac{E_i - \Delta\mathrm{ZPE}}{kT}} \tag{117}$$

We see that in this limiting case $\tilde{Q}_{\mathrm{tot}}^{\infty}$, $\tilde{Q}_{\mathrm{sym}}^{\infty}$ and $\tilde{Q}_{\mathrm{asym}}^{\infty}$ contain Γ_i^{tot}, while $\tilde{Q}_{\mathrm{ch1}}^{\infty}$, $\tilde{Q}_{\mathrm{ch2}}^{\infty}$, $\tilde{Q}_{\mathrm{A}}^{\infty}$, $\tilde{Q}_{\mathrm{B}}^{\infty}$, $\tilde{Q}_{\mathrm{S}}^{\infty}$ and $\tilde{Q}_{\mathrm{I}}^{\infty}$ contain either Γ_i^{ch1} or Γ_i^{ch2}. But, neither of these come as a ratio, so, the absolute values of resonance widths are important in the high-pressure regime. In contrast, the absolute values of stabilization probabilities become unimportant. They either completely cancel, as in $\tilde{Q}_{\mathrm{tot}}^{\infty}$, $\tilde{Q}_{\mathrm{ch1}}^{\infty}$ and $\tilde{Q}_{\mathrm{ch2}}^{\infty}$, or come to play but only as relative ratios $p_i^{\mathrm{sym}}/p_i^{\mathrm{tot}}$ and $p_i^{\mathrm{sym}}/p_i^{\mathrm{tot}}$ in expressions for $\tilde{Q}_{\mathrm{sym}}^{\infty}$, $\tilde{Q}_{\mathrm{asym}}^{\infty}$, $\tilde{Q}_{\mathrm{A}}^{\infty}$, $\tilde{Q}_{\mathrm{B}}^{\infty}$, $\tilde{Q}_{\mathrm{S}}^{\infty}$ and $\tilde{Q}_{\mathrm{I}}^{\infty}$.

II-11 Isotope Effects

The definition of isotopic enrichment is $\delta = \frac{f_p}{f_r} - 1$, where f_p is fractionation of the products and f_r is a fractionation of the reactants.[3] The fractionation of the product can be calculated from the ratio of the isotopes per one molecule. In singly substituted molecule, there is one heavy atom ^{18}O per one molecule in nominator and three ^{16}O in unsubstituted molecule in denominator; the two ^{16}O in singly substituted molecule can be neglected in denominator.

$$f_p = \frac{1 \times [668] + 1 \times [686]}{3 \times [666] + 2 \times [668] + 2 \times [686]} = \frac{[668] + [686]}{3 \times [666]} \tag{118}$$

Thus, the fractionation of the reactants:

$$f_r = \frac{1 \times [68]}{2 \times [66] + 1 \times [68]} = \frac{[68]}{2[66]} \tag{119}$$

Substituting the fractionation of product and reactants into the Equations for enrichment:

$$\delta = \frac{2}{3}\left(\frac{[668] + [686]}{[666]}\right)\frac{[66]}{[68]} - 1 \tag{120}$$

At the initial time, the concentration of the product can be defined through the rate $[668] = R_{\text{asym}}\Delta t$, accordingly for $[686] = R_{\text{sym}}\Delta t$ and $[666] = R_{666}\Delta t$. The rate for substituted molecule depends on the [6], [66], [M] and 3[d] order rate coefficient κ_{666}:

$$R_{666} = \kappa_{666}[6][66][M] \tag{121}$$

Roughly the 3d order rate coefficient equals $\kappa_{666} \approx 2\kappa_{\text{sym}}$.

Substituting all the above Equations into the Equation for isotopic enrichment, we finally obtain:

$$\begin{aligned}\delta &= \frac{2}{3}\left(\frac{R_{\text{asym}} + R_{\text{sym}}}{R_{666}}\right)\frac{[66]}{[68]} - 1 \\ &= \frac{2}{3}\left(\frac{\kappa_{\text{asym}} + \kappa_{\text{sym}}}{\kappa_{666}}\right)\frac{[68][6][66][\text{M}]\Delta t}{[66][6][68][\text{M}]\Delta t} - 1 \\ &= \frac{2}{3}\left(\frac{\kappa_{\text{asym}}}{2\kappa_{\text{sym}}} - 1\right)\end{aligned} \tag{122}$$

The ratio in the bracket accounts for the so-called η-effect:

$$\eta = \frac{\kappa_{\text{asym}}}{2\kappa_{\text{sym}}} = \frac{\kappa_{\text{A}} + \kappa_{\text{B}}K^{\text{ex}}}{2(\kappa_{\text{S}} + \kappa_{\text{I}}K^{\text{ex}})} = \frac{\tilde{Q}_{\text{A}} + \tilde{Q}_{\text{B}}e^{-\frac{\Delta\text{ZPE}}{kT}}}{2\left(\tilde{Q}_{\text{S}} + \tilde{Q}_{\text{I}}e^{-\frac{\Delta\text{ZPE}}{kT}}\right)} = \frac{\tilde{Q}_{\text{asym}}}{2\tilde{Q}_{\text{sym}}} \tag{123}$$

Similar, the ΔZPE effect can be measured by the following ratio:

$$\zeta = \frac{\kappa_{\text{A}}}{\kappa_{\text{B}}K^{\text{ex}}} = \frac{\tilde{Q}_{\text{A}}}{\tilde{Q}_{\text{B}}e^{-\frac{\Delta\text{ZPE}}{kT}}} \tag{124}$$

Finally, the isotope effect on insertion is given by

$$\xi = \frac{\kappa_{\text{I}}^{(\text{d})}}{\kappa_{\text{I}}^{(\text{s})}} \tag{125}$$

Where indexes (s) and (d) correspond to single and double substitution.

II-12 Summary

When one isotope ^{18}O is introduced in ozone formation reaction, several physically distinct *pathways* can be identified. Two of these pathways, A and B, produce asymmetric ozone molecule $^{16}O^{16}O^{18}O$, while the other two, S and I, produce symmetric ozone molecule $^{16}O^{18}O^{16}O$. Importantly, theory allows to split the resonance width and the corresponding decay rate coefficient onto two channel-specific contributions and rate coefficients for *stabilization* of scattering resonances onto two components, those that produce symmetric and asymmetric ozone molecules. With Γ_i^{ch1}, Γ_i^{ch2}, p_i^{sym} and p_i^{asym} in hands, it permits to express four pathway-specific recombination rate coefficients κ_{A}, κ_{B}, κ_{S} and κ_{I}. The rate coefficient κ_{I} of insertion has never been computed theoretically before. The product-specific recombination rate coefficients κ_{sym} and κ_{asym} were derived for symmetric and asymmetric ozone molecules. The product-specific κ_{sym} and κ_{asym} use the same reference channel, namely, the lower energy Channel 2. Additionally, the channel specific recombination rate coefficients κ_{ch1} and κ_{ch2} for two physically distinguishable channels were derived.

Summation over the metastable states of ozone, multiplied by Boltzmann factors and degeneracy factors was introduced as dynamical partition functions $\tilde{Q}$ for four pathways of ozone formation. One important element is a factor $e^{-\Delta\mathrm{ZPE}/kT}$ appears in $\tilde{Q}_{\mathrm{B}}$ and $\tilde{Q}_{\mathrm{I}}$, but not in $\tilde{Q}_{\mathrm{A}}$ and $\tilde{Q}_{\mathrm{S}}$. This energy difference, ΔZPE, entered the theory through the expressions for the equilibrium constant of Channel 1. This result is very interesting for κ_{sym} and κ_{asym} - since several moieties disappeared, the final expressions have the only stabilization probabilities p_i^{sym} vs. p_i^{asym}. It means that product specific rates don't

depend on resonance width, while channel specific recombination rate coefficients κ_{ch1} and κ_{ch2} has no influence probabilities but depend entirely on Γ_i^{ch1} and Γ_i^{ch2}.

New moiety the dynamical weight was introduced. In low-pressure limit $w_i \longrightarrow 1$, and the role of a resonance in the recombination process is maximized. An important point to emphasize is that $\tilde{Q}_{\mathrm{tot}}^{\circ}$, $\tilde{Q}_{\mathrm{sym}}^{\circ}$ and $\tilde{Q}_{\mathrm{asym}}^{\circ}$ do not include the widths of resonances. Therefore, at low pressure any isotope effects in symmetric vs. asymmetric ozone molecules driven by resonance characterized by width are expected to disappear. Therefore, the absolute values of widths do not really matter. What remains important is contribution to Γ_i^{tot} of two reaction channels. In the high-pressure limit [M] $\rightarrow \infty$ the resonance weight decreases as a function of pressure and increases as a function of width: At high pressure $\tilde{Q}_{\mathrm{tot}}^{\infty}$, $\tilde{Q}_{\mathrm{sym}}^{\infty}$ and $\tilde{Q}_{\mathrm{asym}}^{\infty}$ contain Γ_i^{tot}, while $\tilde{Q}_{\mathrm{ch1}}^{\infty}$, $\tilde{Q}_{\mathrm{ch2}}^{\infty}$, $\tilde{Q}_{\mathrm{A}}^{\infty}$, $\tilde{Q}_{\mathrm{B}}^{\infty}$, $\tilde{Q}_{\mathrm{S}}^{\infty}$ and $\tilde{Q}_{\mathrm{I}}^{\infty}$ contain either Γ_i^{ch1} or Γ_i^{ch2}. The absolute values of resonance widths are important in the high-pressure regime. In contrast, the absolute values of stabilization probabilities become unimportant, only contribution to symmetrical or asymmetrical wells.

CHAPTER III. DOUBLY SUBSTITUTED ISOTOPOLOGUE OF OZONE

III-1. Introduction

In many aspects the theoretical treatment of the doubly substituted isotopologue of ozone is similar to that of the singly substituted isotopologue (developed in Chapter II above), but there is one critical difference that makes this case important on its own and requires a careful revamp of all relevant Equations. Namely, in the doubly substituted case, Channel 1 that hosts the reagents with symmetric homonuclear oxygen molecule ($^{18}O^{18}O + {}^{16}O$, see Figure 11) becomes the lower energy channel and has to be taken as a reference of energy for all the metastable reaction intermediates (scattering resonances). This is demonstrated by Figure 11 below and is different from Figure 10 for the singly

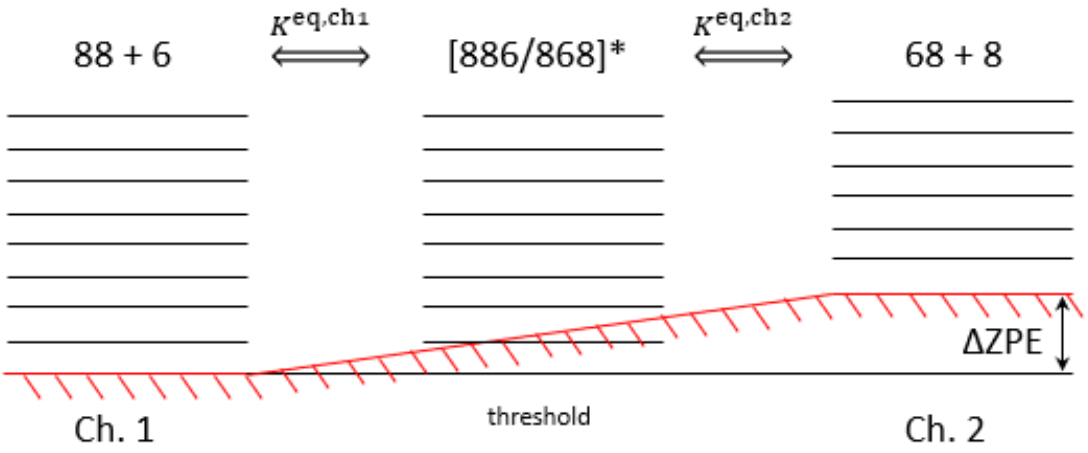

Figure 11. Two distinct channels of ozone formation (left and right) and the metastable ozone states (middle) in the case of double isotopic substitution. Here "6" denotes ^{16}O whereas "8" denotes ^{18}O. Lower energy channel corresponds to the heavier diatomic reagent $^{18}O^{18}O$ with smaller zero-point energy. Upper channel corresponds to the lighter diatomic reagent $^{16}O^{18}O$. Energy difference of the two channels, ΔZPE, is indicated.

substituted case.

Due to this difference, the ΔZPE effect in the experiment switches its direction in the doubly substituted case, compared to the singly substituted case.[11] The theoretical treatment of this effect should also be modified appropriately, as follows.

III-2. Kinetics Expressions for Double Isotopic Substitution

In the doubly substituted case the processes of formation, decay, and stabilization of scattering resonances (metastable intermediates) of ozone are represented by the following reaction scheme:

$$88 + 6 \underset{k^{\mathrm{dec,ch1}}}{\overset{k^{\mathrm{form,ch1}}}{\rightleftharpoons}} [886/868]^{*} \underset{k^{\mathrm{dec,ch2}}}{\overset{k^{\mathrm{form,ch2}}}{\rightleftharpoons}} 68 + 8 \qquad [886/868]^{*} \xrightarrow{k^{\mathrm{stab}}[\mathrm{M}]} \text{ozone} \tag{126}$$

Including these processes in the rate of change expression for the concentrations of intermediate species we can write:

$$\frac{d[\mathrm{O}_3^*]_i}{dt} = k_i^{\mathrm{form,ch1}}[88][6] + k_i^{\mathrm{form,ch2}}[68][8] - k_i^{\mathrm{dec,ch1}}[\mathrm{O}_3^*]_i - k_i^{\mathrm{dec,ch2}}[\mathrm{O}_3^*]_i - k_i^{\mathrm{stab,sym}}[\mathrm{M}][\mathrm{O}_3^*]_i - k_i^{\mathrm{stab,asym}}[\mathrm{M}][\mathrm{O}_3^*]_i \tag{127}$$

In the steady state conditions, applicable to ozone formation reaction, we have:

$$0 = k_i^{\mathrm{form,ch1}}[88][6] + k_i^{\mathrm{form,ch2}}[68][8] - k_i^{\mathrm{dec}}[\mathrm{O}_3^*]_i - k_i^{\mathrm{stab}}[\mathrm{M}][\mathrm{O}_3^*]_i \tag{128}$$

$$[\mathrm{O}_3^*]_i = \frac{k_i^{\mathrm{form,ch1}}[88][6] + k_i^{\mathrm{form,ch2}}[68][8]}{k_i^{\mathrm{dec}} + k_i^{\mathrm{stab}}[\mathrm{M}]} \tag{129}$$

As before, the rate coefficients for formation of resonances through two channels are converted into the corresponding rate coefficients of decay using two equilibrium constants, but here, in the case of double isotopic substitutions, the expressions are

different:

$$K_i^{\mathrm{eq,ch1}} = \frac{(2J+1)\, e^{-E_i/kT}}{Q_{\mathrm{ch1}}} \tag{130}$$

$$K_i^{\mathrm{eq,ch2}} = \frac{(2J+1)\, e^{-E_i/kT}}{Q_{\mathrm{ch2}} e^{-\Delta\mathrm{ZPE}/kT}} \tag{132}$$

Namely, here the $e^{-\Delta\mathrm{ZPE}/kT}$ factor shows up in Channel 2 (in contrast with the singly substituted case, where it appears in Channel 1). The value of ΔZPE itself in the doubly substituted case is also slightly different than in the singly substituted case. Here we have:

$$\Delta\mathrm{ZPE} = \mathrm{ZPE}(68) - \mathrm{ZPE}(88) = 22.94\ \mathrm{cm}^{-1}$$

Using these formulae, we obtain the following expressions for two product-specific rates of recombination process:

$$\begin{aligned} R_{\mathrm{sym}} = {} & [\mathrm{M}][68][8]\frac{k^{\mathrm{stab}}}{Q_{\mathrm{ch2}}}\sum_i (2J+1)p_i^{\mathrm{sym}}\frac{\frac{\Gamma_i^{\mathrm{ch2}}}{\hbar}}{\frac{\Gamma_i^{\mathrm{tot}}}{\hbar}+k_i^{\mathrm{stab}}[\mathrm{M}]}e^{-\frac{E_i-\Delta\mathrm{ZPE}}{kT}} \\ & + [\mathrm{M}][88][6]\frac{k^{\mathrm{stab}}}{Q_{\mathrm{ch1}}}\sum_i (2J+1)p_i^{\mathrm{sym}}\frac{\frac{\Gamma_i^{\mathrm{ch1}}}{\hbar}}{\frac{\Gamma_i^{\mathrm{tot}}}{\hbar}+k_i^{\mathrm{stab}}[\mathrm{M}]}e^{-\frac{E_i}{kT}} \end{aligned} \tag{133}$$

$$\begin{aligned} R_{\mathrm{asym}} = {} & [\mathrm{M}][68][8]\,\frac{k^{\mathrm{stab}}}{Q_{\mathrm{ch2}}}\sum_i (2J+1)p_i^{\mathrm{asym}}\frac{\frac{\Gamma_i^{\mathrm{ch2}}}{\hbar}}{\frac{\Gamma_i^{\mathrm{tot}}}{\hbar}+k_i^{\mathrm{stab}}[\mathrm{M}]}\,e^{-\frac{E_i-\Delta\mathrm{ZPE}}{kT}} \\ & + [\mathrm{M}][88][6]\,\frac{k^{\mathrm{stab}}}{Q_{\mathrm{ch1}}}\sum_i (2J+1)p_i^{\mathrm{asym}}\frac{\frac{\Gamma_i^{\mathrm{ch1}}}{\hbar}}{\frac{\Gamma_i^{\mathrm{tot}}}{\hbar}+k_i^{\mathrm{stab}}[\mathrm{M}]}\,e^{-\frac{E_i}{kT}} \end{aligned} \tag{134}$$

The following four pathway-specific dynamical partition functions can be introduced to simplify these expressions:

$$\tilde{Q}_{\mathrm{A}} \equiv \sum_i (2J+1)\, w_i \frac{\Gamma_i^{\mathrm{ch2}}}{\Gamma_i^{\mathrm{tot}}}\, p_i^{\mathrm{asym}}\, e^{-\frac{E_i-\Delta\mathrm{ZPE}}{kT}} \tag{135}$$

$$\tilde{Q}_{\mathrm{B}} \equiv \sum_i (2J+1)\, w_i \frac{\Gamma_i^{\mathrm{ch1}}}{\Gamma_i^{\mathrm{tot}}}\, p_i^{\mathrm{asym}} e^{-\frac{E_i}{kT}} \tag{136}$$

$$\tilde{Q}_{\mathrm{S}} \equiv \sum_i (2J+1)\, w_i \frac{\Gamma_i^{\mathrm{ch2}}}{\Gamma_i^{\mathrm{tot}}}\, p_i^{\mathrm{sym}} e^{-\frac{E_i-\Delta\mathrm{ZPE}}{kT}} \tag{137}$$

$$\tilde{Q}_{\mathrm{I}} \equiv \sum_i (2J+1)\, w_i \frac{\Gamma_i^{\mathrm{ch1}}}{\Gamma_i^{\mathrm{tot}}}\, p_i^{\mathrm{sym}} e^{-\frac{E_i}{kT}} \tag{138}$$

Note that here the ΔZPE shifts appear in the expressions for $\tilde{Q}_{\mathrm{A}}$ and $\tilde{Q}_{\mathrm{S}}$, while in the case of single isotopic substitution they appeared in $\tilde{Q}_{\mathrm{B}}$ and $\tilde{Q}_{\mathrm{I}}$.

The isotope exchange process, and the corresponding equilibrium constant, in the case of double substitution are:

$$88 + 6 \rightleftharpoons 68 + 8 \tag{139}$$

$$K^{\mathrm{ex}} = \frac{[68][8]}{[88][6]} = \frac{Q_{\mathrm{ch2}} e^{-\Delta\mathrm{ZPE}/kT}}{Q_{\mathrm{ch1}}} \tag{140}$$

where the factor $e^{-\Delta\mathrm{ZPE}/kT}$ is used in Channel 2. The forward direction of the isotope exchange here is defined as from Channel 1 to Channel 2, opposite to the singly substituted case. The value of this equilibrium constant is expected to be on the order of 2 due to symmetry of the homonuclear diatomic reagent in the Channel 1, in which every other rotational state is forbidden by symmetry. Using this expression, we can rewrite formula for the rates in the way where all pathways are referenced relative to the lowest energy channel, as follows:

$$R_{\mathrm{sym}} = R_{\mathrm{S}} + R_{\mathrm{I}} = \kappa_{\mathrm{S}}[\mathrm{M}][68][8] + \kappa_{\mathrm{I}}[\mathrm{M}][88][6] = (\kappa_{\mathrm{S}}\frac{[68][8]}{[88][6]} + \kappa_{\mathrm{I}})[88][6][\mathrm{M}] = \kappa_{\mathrm{sym}}[88][6][\mathrm{M}] \quad (141)$$

$$R_{\mathrm{asym}} = R_{\mathrm{A}} + R_{\mathrm{B}} = \kappa_{\mathrm{A}}[\mathrm{M}][68][8] + \kappa_{\mathrm{B}}[\mathrm{M}][88][6] = (\kappa_{\mathrm{A}}\frac{[68][8]}{[88][6]} + \kappa_{\mathrm{B}})[88][6][\mathrm{M}] = \kappa_{\mathrm{asym}}[88][6][\mathrm{M}] \quad (142)$$

A relationship between the pathway-specific rate coefficients and the product-specific rate coefficients then looks as follows:

$$\kappa_{\mathrm{sym}} = \kappa_{\mathrm{S}}K^{\mathrm{ex}} + \kappa_{\mathrm{I}} = k^{\mathrm{stab}}\frac{\tilde{Q}_{\mathrm{sym}}}{Q_{\mathrm{ch1}}} \quad (143)$$

$$\kappa_{\mathrm{asym}} = \kappa_{\mathrm{A}}K^{\mathrm{ex}} + \kappa_{\mathrm{B}} = k^{\mathrm{stab}}\frac{\tilde{Q}_{\mathrm{asym}}}{Q_{\mathrm{ch1}}} \quad (144)$$

Note that here, in the doubly substituted case, the K^{ex} sticks to the rate coefficients of pathways A and S that originate in the higher energy channel, the Channel 2. Interestingly, the equations for product-specific dynamical partition functions $\tilde{Q}_{\mathrm{sym}}$ and $\tilde{Q}_{\mathrm{asym}}$ in the doubly-substituted case appear to be entirely identical to those derived for the singly-substituted case, simply because these formula do not contain any $e^{-\Delta\mathrm{ZPE}/kT}$ factors (they analytically cancel, as it was discussed in Chapter II). Therefore, they will not be repeated here.

The equations for channel-specific dynamical partition functions and rate coefficients are obtained by regrouping of the four pathway-specific contributions κ_{A}, κ_{B}, κ_{S} and κ_{I}, which gives:

$$\kappa_{\mathrm{ch1}} = \kappa_{\mathrm{B}} + \kappa_{\mathrm{I}} = k^{\mathrm{stab}} \frac{\tilde{Q}_{\mathrm{ch1}}}{Q_{\mathrm{ch1}}} \tag{145}$$

$$\kappa_{\mathrm{ch2}} = \kappa_{\mathrm{A}} + \kappa_{\mathrm{S}} = k^{\mathrm{stab}} \frac{\tilde{Q}_{\mathrm{ch2}}}{Q_{\mathrm{ch2}}} \tag{146}$$

Where the dynamic partition functions for both channels:

$$\tilde{Q}_{\mathrm{ch1}} \equiv \tilde{Q}_{\mathrm{B}} + \tilde{Q}_{\mathrm{I}} = \sum_i (2J+1)\, w_i \frac{\Gamma_i^{\mathrm{ch1}}}{\Gamma_i^{\mathrm{tot}}}\, p_i^{\mathrm{tot}}\, e^{-\frac{E_i}{kT}} \tag{147}$$

$$\tilde{Q}_{\mathrm{ch2}} \equiv \tilde{Q}_{\mathrm{A}} + \tilde{Q}_{\mathrm{S}} = \sum_i (2J+1)\, w_i \frac{\Gamma_i^{\mathrm{ch2}}}{\Gamma_i^{\mathrm{tot}}}\, p_i^{\mathrm{tot}}\, e^{-\frac{E_i - \Delta\mathrm{ZPE}}{kT}} \tag{148}$$

Again, the difference from the singly substituted case is that here the $e^{-\Delta\mathrm{ZPE}/kT}$ factor comes with the upper Channel 2.

For completeness, we list all formula for the low- and high-pressure limits:

$$\tilde{Q}^{\circ}_{\mathrm{tot}} = \sum_i (2J+1)\, p_i^{\mathrm{tot}}\, e^{-\frac{E_i}{kT}} \tag{149}$$

$$\tilde{Q}^{\circ}_{\mathrm{sym}} = \sum_i (2J+1)\, p_i^{\mathrm{sym}}\, e^{-\frac{E_i}{kT}} \tag{150}$$

$$\tilde{Q}^{\circ}_{\mathrm{asym}} = \sum_i (2J+1)\, p_i^{\mathrm{asym}}\, e^{-\frac{E_i}{kT}} \tag{151}$$

$$\tilde{Q}^{\circ}_{\mathrm{ch1}} = \sum_i (2J+1)\, \frac{\Gamma_i^{\mathrm{ch1}}}{\Gamma_i^{\mathrm{tot}}}\, p_i^{\mathrm{tot}}\, e^{-\frac{E_i}{kT}} \tag{152}$$

$$\tilde{Q}^{\circ}_{\mathrm{ch2}} = \sum_i (2J+1)\, \frac{\Gamma_i^{\mathrm{ch2}}}{\Gamma_i^{\mathrm{tot}}}\, p_i^{\mathrm{tot}}\, e^{-\frac{E_i - \Delta\mathrm{ZPE}}{kT}} \tag{153}$$

$$\tilde{Q}_{\mathrm{A}}^{\circ} = \sum_i (2J+1) \frac{\Gamma_i^{\mathrm{ch2}}}{\Gamma_i^{\mathrm{tot}}} p_i^{\mathrm{asym}} e^{-\frac{E_i - \Delta\mathrm{ZPE}}{kT}} \quad (154)$$

$$\tilde{Q}_{\mathrm{B}}^{\circ} = \sum_i (2J+1) \frac{\Gamma_i^{\mathrm{ch1}}}{\Gamma_i^{\mathrm{tot}}} p_i^{\mathrm{asym}} e^{-\frac{E_i}{kT}} \quad (155)$$

$$\tilde{Q}_{\mathrm{S}}^{\circ} = \sum_i (2J+1) \frac{\Gamma_i^{\mathrm{ch2}}}{\Gamma_i^{\mathrm{tot}}} p_i^{\mathrm{sym}} e^{-\frac{E_i - \Delta\mathrm{ZPE}}{kT}} \quad (156)$$

$$\tilde{Q}_{\mathrm{I}}^{\circ} = \sum_i (2J+1) \frac{\Gamma_i^{\mathrm{ch1}}}{\Gamma_i^{\mathrm{tot}}} p_i^{\mathrm{sym}} e^{-\frac{E_i}{kT}} \quad (157)$$

$$\tilde{Q}_{\mathrm{tot}}^{\infty} = \sum_i (2J+1) \frac{\Gamma_i^{\mathrm{tot}}}{\hbar k^{\mathrm{stab}}[\mathrm{M}]} e^{-\frac{E_i}{kT}} \quad (158)$$

$$\tilde{Q}_{\mathrm{sym}}^{\infty} = \sum_i (2J+1) \frac{\Gamma_i^{\mathrm{tot}}}{\hbar k^{\mathrm{stab}}[\mathrm{M}]} \frac{p_i^{\mathrm{sym}}}{p_i^{\mathrm{tot}}} e^{-\frac{E_i}{kT}} \quad (159)$$

$$\tilde{Q}_{\mathrm{asym}}^{\infty} = \sum_i (2J+1) \frac{\Gamma_i^{\mathrm{tot}}}{\hbar k^{\mathrm{stab}}[\mathrm{M}]} \frac{p_i^{\mathrm{asym}}}{p_i^{\mathrm{tot}}} e^{-\frac{E_i}{kT}} \quad (160)$$

$$\tilde{Q}_{\mathrm{ch1}}^{\infty} = \sum_i (2J+1) \frac{\Gamma_i^{\mathrm{ch1}}}{\hbar k^{\mathrm{stab}}[\mathrm{M}]} e^{-\frac{E_i}{kT}} \quad (161)$$

$$\tilde{Q}_{\mathrm{ch2}}^{\infty} = \sum_i (2J+1) \frac{\Gamma_i^{\mathrm{ch2}}}{\hbar k^{\mathrm{stab}}[\mathrm{M}]} e^{-\frac{E_i - \Delta\mathrm{ZPE}}{kT}} \quad (162)$$

$$\tilde{Q}_{\mathrm{A}}^{\infty} = \sum_i (2J+1) \frac{\Gamma_i^{\mathrm{ch2}}}{\hbar k^{\mathrm{stab}}[\mathrm{M}]} \frac{p_i^{\mathrm{asym}}}{p_i^{\mathrm{tot}}} e^{-\frac{E_i - \Delta\mathrm{ZPE}}{kT}} \quad (163)$$

$$\tilde{Q}_{\mathrm{B}}^{\infty} = \sum_i (2J+1) \frac{\Gamma_i^{\mathrm{ch1}}}{\hbar k^{\mathrm{stab}}[\mathrm{M}]} \frac{p_i^{\mathrm{asym}}}{p_i^{\mathrm{tot}}} e^{-\frac{E_i}{kT}} \tag{164}$$

$$\tilde{Q}_{\mathrm{S}}^{\infty} = \sum_i (2J+1) \frac{\Gamma_i^{\mathrm{ch2}}}{\hbar k^{\mathrm{stab}}[\mathrm{M}]} \frac{p_i^{\mathrm{sym}}}{p_i^{\mathrm{tot}}} e^{-\frac{E_i - \Delta\mathrm{ZPE}}{kT}} \tag{165}$$

$$\tilde{Q}_{\mathrm{I}}^{\infty} = \sum_i (2J+1) \frac{\Gamma_i^{\mathrm{ch1}}}{\hbar k^{\mathrm{stab}}[\mathrm{M}]} \frac{p_i^{\mathrm{sym}}}{p_i^{\mathrm{tot}}} e^{-\frac{E_i}{kT}} \tag{166}$$

The measures for two isotope effects in the case of double substitution are defined as follows:

$$\eta = \frac{\kappa_{\mathrm{asym}}}{2\kappa_{\mathrm{sym}}} = \frac{\kappa_{\mathrm{A}} K^{\mathrm{ex}} + \kappa_{\mathrm{B}}}{2(\kappa_{\mathrm{S}} K^{\mathrm{ex}} + \kappa_{\mathrm{I}})} = \frac{\tilde{Q}_{\mathrm{A}} e^{-\frac{\Delta\mathrm{ZPE}}{kT}} + \tilde{Q}_{\mathrm{B}}}{2\left(\tilde{Q}_{\mathrm{S}} e^{-\frac{\Delta\mathrm{ZPE}}{kT}} + \tilde{Q}_{\mathrm{I}}\right)} = \frac{\tilde{Q}_{\mathrm{asym}}}{2\tilde{Q}_{\mathrm{sym}}} \tag{167}$$

$$\zeta = \frac{\kappa_{\mathrm{B}}}{\kappa_{\mathrm{A}} K^{\mathrm{ex}}} = \frac{\tilde{Q}_{\mathrm{B}}}{\tilde{Q}_{\mathrm{A}} e^{-\Delta\mathrm{ZPE}/kT}} \tag{168}$$

Note that expression for the symmetry-driven η-effect is exactly the same as in the case of single isotopic substitution, while the formula for ζ-effect driven by $\Delta\mathrm{ZPE}$ is different. Now the $e^{-\Delta\mathrm{ZPE}/kT}$ factor comes with $\tilde{Q}_{\mathrm{A}}$ for the upper channel. Also, the ratio of κ_{A} and κ_{B} is also inverted in this case, in order to have $\zeta > 1$, to stay consistent with experimental definitions.[1]

III-3. Analysis of Temperature Dependencies.

Analysis of Figure 10 and Figure 11 suggests that among the four pathways of ozone forming reaction (A, B, S and I) some pathways may be more exo-ergic or endo-ergic than others, and this happens differently in the singly and doubly substituted cases. It should be pointed out, however, that in both singly and doubly substituted cases the pathway S is expected to be *iso-ergic*, because the isotope exchange reaction associated

with it has the same species on both sides, that correspond to two physically indistinguishable components of the Channel 2 (see Figure 9). For example, for the singly substituted case:

$$68 + 6 \overset{K^{\mathrm{eq,ch2}}}{\Longleftrightarrow} [686]^{*} \overset{K^{\mathrm{eq,ch2}}}{\Longleftrightarrow} 6 + 86$$

and for the doubly substituted case:

$$86 + 8 \overset{K^{\mathrm{eq,ch2}}}{\Longleftrightarrow} [868]^{*} \overset{K^{\mathrm{eq,ch2}}}{\Longleftrightarrow} 8 + 68$$

Therefore, when we want to look at the temperature dependence, it is useful to use pathway S as a reference for all other recombination pathways. Table 3 lists the ratios of rate coefficients for exo-ergic and endo-ergic pathways A and B, over that for the iso-ergic pathway S, and their corresponding expressions in terms of the dynamical partition functions of the reaction pathways, for both single and double isotopic substitutions. The values of all these ratios are expected to be on the order of 1 because, if the isotope effects are neglected, we expect that $\kappa_{\mathrm{A}} \approx \kappa_{\mathrm{S}}$ while $\kappa_{\mathrm{B}} \approx 2\kappa_{\mathrm{S}}$ (is twice larger), due to symmetry of the homonuclear reagent in the Channel 1. Alternatively, inspired by Equations 81-82 and 143-144 where some rate coefficients show up multiplied by K^{ex}, we could compare their relative contributions, instead of the *ad hoc* multiplication by a factor of 2. The relevant formula is given in the last row of Table 3. Note that this approach cancels the ratio of the reagent partition functions for two channels $Q_{\mathrm{ch2}}/Q_{\mathrm{ch1}}$, but introduces the $e^{-\Delta \mathrm{ZPE}/kT}$ factor.

Table 3. The ratios of rate coefficients for exo- and endo-ergic pathways A and B over the rate coefficient for an iso-ergic pathway S, for singly and doubly substituted cases, and their expressions in terms of the dynamical partition functions.

Definition		Equation	
Single subst.	Double subst.	Single subst.	Double subst.
$\frac{\kappa_{\mathrm{A}}}{\kappa_{\mathrm{S}}}$	$\frac{\kappa_{\mathrm{A}}}{\kappa_{\mathrm{S}}}$	$\left(\frac{\tilde{Q}_{\mathrm{A}}}{\tilde{Q}_{\mathrm{S}}}\right)$	$\left(\frac{\tilde{Q}_{\mathrm{A}}}{\tilde{Q}_{\mathrm{S}}}\right)$
$\frac{\kappa_{\mathrm{B}}}{2\kappa_{\mathrm{S}}}$	$\frac{\kappa_{\mathrm{B}}}{2\kappa_{\mathrm{S}}}$	$\frac{Q_{\mathrm{ch2}}}{2Q_{\mathrm{ch1}}}\left(\frac{\tilde{Q}_{\mathrm{B}}}{\tilde{Q}_{\mathrm{S}}}\right)$	$\frac{Q_{\mathrm{ch2}}}{2Q_{\mathrm{ch1}}}\left(\frac{\tilde{Q}_{\mathrm{B}}}{\tilde{Q}_{\mathrm{S}}}\right)$
$\frac{K^{\mathrm{ex}}\kappa_{\mathrm{B}}}{\kappa_{\mathrm{S}}}$	$\frac{\kappa_{\mathrm{B}}}{K^{\mathrm{ex}}\kappa_{\mathrm{S}}}$	$e^{-\Delta\mathrm{ZPE}/kT}\left(\frac{\tilde{Q}_{\mathrm{B}}}{\tilde{Q}_{\mathrm{S}}}\right)$	$\frac{1}{e^{-\Delta\mathrm{ZPE}/kT}}\left(\frac{\tilde{Q}_{\mathrm{B}}}{\tilde{Q}_{\mathrm{S}}}\right)$
$\frac{\kappa_{\mathrm{B}}}{2\kappa_{\mathrm{A}}}$	$\frac{\kappa_{\mathrm{B}}}{2\kappa_{\mathrm{A}}}$	$\frac{Q_{\mathrm{ch2}}}{2Q_{\mathrm{ch1}}}\left(\frac{\tilde{Q}_{\mathrm{B}}}{\tilde{Q}_{\mathrm{A}}}\right)$	$\frac{Q_{\mathrm{ch2}}}{2Q_{\mathrm{ch1}}}\left(\frac{\tilde{Q}_{\mathrm{B}}}{\tilde{Q}_{\mathrm{A}}}\right)$
$\frac{\kappa_{\mathrm{B}}K^{\mathrm{ex}}}{\kappa_{\mathrm{A}}}$	$\frac{\kappa_{\mathrm{B}}}{\kappa_{\mathrm{A}}K^{\mathrm{ex}}}$	$e^{-\Delta\mathrm{ZPE}/kT}\left(\frac{\tilde{Q}_{\mathrm{B}}}{\tilde{Q}_{\mathrm{A}}}\right)$	$\frac{1}{e^{-\Delta\mathrm{ZPE}/kT}}\left(\frac{\tilde{Q}_{\mathrm{B}}}{\tilde{Q}_{\mathrm{A}}}\right)$

Table 4. The ratios of rate coefficients for singly and doubly substituted cases, using exo- and endo-ergic pathways A and B, and an iso-ergic pathway S, and their expressions in terms of the dynamical partition functions.

Definition	Equation
$\frac{\kappa_{\mathrm{S}}^{(\mathrm{s})}}{\kappa_{\mathrm{S}}^{(\mathrm{d})}}$	$\left(\frac{\tilde{Q}_{\mathrm{S}}^{(\mathrm{s})}}{\tilde{Q}_{\mathrm{S}}^{(\mathrm{d})}}\right)$
$\frac{\kappa_{\mathrm{A}}^{(\mathrm{s})}}{\kappa_{\mathrm{A}}^{(\mathrm{d})}}$	$\left(\frac{\tilde{Q}_{\mathrm{A}}^{(\mathrm{s})}}{\tilde{Q}_{\mathrm{A}}^{(\mathrm{d})}}\right)$
$\frac{\kappa_{\mathrm{B}}^{(\mathrm{d})}}{\kappa_{\mathrm{B}}^{(\mathrm{s})}}$	$\frac{\tilde{Q}_{\mathrm{ch1}}^{(\mathrm{s})}}{\tilde{Q}_{\mathrm{ch1}}^{(\mathrm{d})}}\left(\frac{\tilde{Q}_{\mathrm{B}}^{(\mathrm{d})}}{\tilde{Q}_{\mathrm{B}}^{(\mathrm{s})}}\right)$
$\frac{\kappa_{\mathrm{B}}^{(\mathrm{d})}}{2\kappa_{\mathrm{A}}^{(\mathrm{s})}}$	$\frac{\tilde{Q}_{\mathrm{ch2}}^{(\mathrm{s})}}{2\tilde{Q}_{\mathrm{ch1}}^{(\mathrm{d})}}\left(\frac{\tilde{Q}_{\mathrm{B}}^{(\mathrm{d})}}{\tilde{Q}_{\mathrm{A}}^{(\mathrm{s})}}\right)$
$\frac{\kappa_{\mathrm{B}}^{(\mathrm{s})}}{2\kappa_{\mathrm{A}}^{(\mathrm{d})}}$	$\frac{\tilde{Q}_{\mathrm{ch2}}^{(\mathrm{d})}}{2\tilde{Q}_{\mathrm{ch1}}^{(\mathrm{s})}}\left(\frac{\tilde{Q}_{\mathrm{B}}^{(\mathrm{s})}}{\tilde{Q}_{\mathrm{A}}^{(\mathrm{d})}}\right)$

More insight into temperature-dependence of exo- and endo-ergic recombination pathways can be obtained if one compares and contrasts the pathways in singly and doubly substituted cases, by taking their rations. This is done in Table 4, where the symbol "(s)" is used for the single isotope substitution, while the symbol "(d)" is used for the double isotope substitution.

Table 5. The ratios of rate coefficients in singly and doubly substituted cases, using lower and upper Channels 1 and 2, and their expressions in terms of the dynamical partition functions.

Definition		Equation	
Singly subst.	Doubly subst.	Singly subst.	Doubly subst.
$\frac{\kappa_{\mathrm{ch1}}}{\kappa_{\mathrm{ch2}}}$	$\frac{\kappa_{\mathrm{ch1}}}{\kappa_{\mathrm{ch2}}}$	$\frac{Q_{\mathrm{ch2}}}{Q_{\mathrm{ch1}}}\left(\frac{\tilde{Q}_{\mathrm{ch1}}}{\tilde{Q}_{\mathrm{ch2}}}\right)$	$\frac{Q_{\mathrm{ch2}}}{Q_{\mathrm{ch1}}}\left(\frac{\tilde{Q}_{\mathrm{ch1}}}{\tilde{Q}_{\mathrm{ch2}}}\right)$
$2K^{\mathrm{ex}}\frac{\kappa_{\mathrm{ch1}}}{\kappa_{\mathrm{ch2}}}$	$\frac{2}{K^{\mathrm{ex}}}\frac{\kappa_{\mathrm{ch1}}}{\kappa_{\mathrm{ch2}}}$	$e^{-\Delta\mathrm{ZPE}/kT}\left(\frac{2\tilde{Q}_{\mathrm{ch1}}}{\tilde{Q}_{\mathrm{ch2}}}\right)$	$\frac{1}{e^{-\Delta\mathrm{ZPE}/kT}}\left(\frac{2\tilde{Q}_{\mathrm{ch1}}}{\tilde{Q}_{\mathrm{ch2}}}\right)$
$2\frac{\kappa_{\mathrm{tot}}^{(\mathrm{s})}}{\kappa_{\mathrm{tot}}^{(\mathrm{d})}}$		$\frac{2Q_{\mathrm{ch1}}^{(\mathrm{d})}}{Q_{\mathrm{ch2}}^{(\mathrm{s})}}\left(\frac{\tilde{Q}_{\mathrm{ch1}}^{(\mathrm{s})}e^{-\Delta\mathrm{ZPE}/kT}+\tilde{Q}_{\mathrm{ch2}}^{(\mathrm{s})}}{\tilde{Q}_{\mathrm{ch1}}^{(\mathrm{d})}+\tilde{Q}_{\mathrm{ch2}}^{(\mathrm{d})}e^{-\Delta\mathrm{ZPE}/kT}}\right)$	

Finally, we can study the temperature dependence of channel-specific rate coefficients for the lower and upper channels (Channel 1 vs Channel 2) in the singly and doubly substituted cases, by taking their ratios. The reference case, with no temperature dependence can be represented by the ratio of the total recombination rate coefficient that includes both channels. The formula needed for this analysis are summarized in are summarized in Table 5.

III-4. Summary

Doubly substituted isotopologue of ozone is similar to that of the singly substituted isotopologue, but the lower Channel 1 became a reference of energy for all the IMS. Because of factor $e^{-\Delta\mathrm{ZPE}/kT}$ which appears in Channel 2, in contra, pathway-specific rates appeared to be referenced relative to the lowest energy Channel 1. Within

dynamic partition functions $e^{-\Delta \mathrm{ZPE}/kT}$ factor comes with the upper Channel 2. The formula for the low- and high-pressure limits transform accordingly to that. Finally, symmetry-driven η-effect is the same as in the case of single isotopic substitution, while the pathway-driven η-effect changes according to pathway-specific rates. The ζ-effect driven by ΔZPE changes as well. Now the $e^{-\Delta \mathrm{ZPE}/kT}$ factor sticks to upper channel $\tilde{Q}_{\mathrm{A}}$. Knowing that the ratio of κ_{A} and κ_{B} is also inverted in this case in the sake of consistency with experimental definitions.

The exoergicity and endoergicity of four ozone formation pathways in the singly and doubly isotopologues were found to be different. The pathway S shows up as *iso-ergic*, that makes it useful as a reference for all other recombination pathways. The values of all these ratios are expected to be on the order of 1 and $\kappa_{\mathrm{A}} \approx \kappa_{\mathrm{S}}$ while $\kappa_{\mathrm{B}} \approx 2\kappa_{\mathrm{S}}$. The ratio approach cancels the reagent partition functions $Q_{\mathrm{ch2}}/Q_{\mathrm{ch1}}$, but introduces the $e^{-\Delta \mathrm{ZPE}/kT}$ factor. Some interesting ratios were proposed for further analysis, particularly, of the pathway-specific rates and channel-specific rate coefficients for the lower and upper channels.

CHAPTER IV. NUMERICAL RESULTS: ISOTOPE EFFECTS, INSERTION PATHWAY, AND TEMPERATURE DEPENDENCE

IV-1. Introduction

While many reports of experimental measurements of the anomalous enrichments of ozone in rare isotopes of oxygen exists in the literature, some of which were conducted in the lab and some in the atmosphere[35], the only truly systematic experimental study of the pathway-specific recombination rates belongs to the group of Konrad Mauersberger at the University of Heidelberg in Germany[2], now inherited by his younger colleague Christoff Janssen and collaborators at the University of Pierre and Marie Curie, Paris, France.[11] They published the experimental rate coefficients κ_{A}, κ_{B}, κ_{S} and κ_{I} for singly and doubly substituted ozone isotopologues in the famous PCCP paper[10], but some of those were later remeasured (namely, κ_{A} and κ_{S} in the singly substituted case) and the updated values reported in the PhD dissertation of Tuzson.[35] All their rate coefficients were reported unitless, relative to the third order rate coefficient κ_{666} for the formation of the "normal" ozone $^{16}O^{16}O^{16}O$, and were multiplied by two in the cases of heteronuclear diatomic reagent (in order to offset the effect of symmetry). In Table 6 we converted their data back into the absolute rate coefficients using experimental value $\kappa_{666} = 60\times10^{-35}$ cm^6/s and dividing by 2 the data for pathways A and S.

Experimental data presented in Table 6 indicate a broad variation of recombination rate coefficients through isotopomers and isotopologues of ozone. In the first data-column we collected the values of κ_{S} for iso-ergic pathways that can be used as a convenient reference for each case (all very close to $\kappa_{666}/2$).

Table 6. Experimental and theoretical rate coefficients (in the units of 10^{-35} cm^6/s) for different pathways of ozone formation at room temperature in the cases of single and double isotopic substitution, and the corresponding isotope effects.

Source	Isotope subst.	κ_S	κ_A	κ_B	κ_I	ζ-effect	η-effect	ξ-effect
Experiment, Janssen et al[10]	single	30	43	55	0.36	1.55	1.16	4.83
	double	31	28	90	1.74	1.63	1.13	
Theory, Teplukhin et al[14,25]	single	31	38	~~51~~		1.49	1.03	
	double	31	29	~~78~~		1.38	1.12	

The values of rate coefficients κ_A and κ_B for exo-ergic and endo-ergic pathways deviate significantly from κ_S, and, importantly, these deviations occur in the opposite directions in the cases of single and double isotopic substitutions. Finally, the values of κ_I for the insertion pathway in the last column of experimental data are much smaller than the other three, by up to two orders of magnitude.

We reanalyzed these experimental data using the definitions of three distinct isotope effects introduced in Chapter II and Chapter III above. Namely, the variation of rate coefficient for exo-ergic and endo-ergic pathways A and B is given by the ratio $\zeta = \kappa_A/(\kappa_B K^{ex})$ in the case of single substitution or $\zeta = \kappa_B/(\kappa_A K^{ex})$ in the case of double substitution (see Equations 125 and 168 above). Experimental values of this zeta-effect driven by ΔZPE are similar in singly and doubly substituted cases and are pretty large, around $\zeta = 1.59 \mp 0.04$, which is rather surprising taking into account small mass differences between oxygen isotopes ^{16}O and ^{18}O. Next, the difference between formation

of asymmetric and symmetric ozone molecules, is given by the ratio $\eta = \frac{1}{2}\,(\kappa_A + \kappa_B K^{\mathrm{ex}})/(\kappa_S + \kappa_I K^{\mathrm{ex}})$ in the case of single substitution or $\eta = \frac{1}{2}(\kappa_{\mathrm{A}} K^{\mathrm{ex}} + \kappa_{\mathrm{B}})/(\kappa_{\mathrm{S}} K^{\mathrm{ex}} + \kappa_{\mathrm{I}})$ in the case of double substitution (see Equations 124 and 167 above). Experimental values of this *eta-effec*t driven by symmetry are smaller but are still quite significant, and again are similar in the singly and doubly substituted cases, about $\eta = 1.14 \pm 0.01$. Finally, the difference of the insertion rates in singly and doubly substituted cases is given by the ratio $\xi = \kappa_{\mathrm{I}}^{(\mathrm{d})}/\kappa_{\mathrm{I}}^{(\mathrm{s})}$, Eq. (125). In the experiment this *xsi-effect*, as we think driven by tunneling, is ξ =4.83, which is particularly notable.

Zeta-effect, driven by quantum ΔZPE, has received the most of attention from the theory side, including the empirical work of Marcus group[36], the early work of Babikov[37], and the work of Schinke group.[38] Eta-effect, postulated empirically by Marcus and co-workers[39], is not yet entirely understood, although it is clear that it must somehow be related to the symmetries of ozone isotopomers. Alternative theories were developed by several other workers, among which the dimensionally-reduced treatment of Clary and co.[40] and the sudden-approximation calculations of Bowman and co.[41], are worth mentioning recent work of Robert and co-workers[42] lacks the rigor of computational chemistry. The most sophisticated and systematic theoretical treatment of these processes was developed by Teplukhin and co-workers[3], except that they have chosen to neglect the insertion pathway (to our best knowledge, the insertion process in the ozone-forming reaction has never been studied by anyone). The lower part of Table 6 contains the theoretical results of Teplukhin et al.[14] They reproduce ζ-effect relatively well, giving correct direction ($\zeta > 1$) and the magnitudes of ζ for both singly and doubly substituted cases, in reasonable agreement with experiments (see Table 6). This theoretical approach

also holds some promise for reproducing η-effect, since it gives correct direction of the effect ($\eta > 1$), although the magnitude is not systematically correct: it is reasonably good in the case of double substitution but is too small in the case of single substitution (see Table 6). Two boxes for κ_{I} (in singly and doubly substituted cases) and the box for ξ are left blank. Two entries, for κ_{B} (in the singly and doubly substituted cases) are crossed through because, after that work was published, a mistake in the code was found that introduced some error into the treatment of those pathways. One of the goals of this work is to update theory predictions in Table 6 and to fill the blanks for insertion pathway.

Alexander Teplukhin carried out rather sophisticated quantum mechanical calculations of the spectra of scattering resonances in ozone (their energies E_i, channel-specific widths Γ_i^{ch1} and Γ_i^{ch2}, product specific probabilities p_i^{sym} and p_i^{asym}), conducted in a systematic way for single and double substitutions, in a broad range of resonance energies (vibrational excitations) for a broad range or rotational states (up to $J = 60$). But, before graduating and leaving he was only able to plug these data into one simplest kinetics model of the recombination reaction, without exploring all possibilities.

I inherited his database, and the goals of my project are:

1) To tie loose ends of the previous work, by updating the table with isotope effects but then going beyond the previous work to fill the gaps by computing the data for insertion;
2) Studying the dependencies of pathway-specific rate coefficients (κ_{A}, κ_{B}, κ_{S}, κ_{I}) and isotope effects (ζ, η, ξ) on temperature and pressure of bath gas [M], and comparing with experiments;

3) Testing various models for the stabilization step of the recombination reaction, trying several definitions of stabilization probabilities p_i^{sym} and p_i^{asym}, and possibly more sophisticated models for k_i^{stab};
4) Classifying the properties of scattering resonances by splitting them onto the groups with certain distributions of resonance lifetimes Γ_i^{ch1} and Γ_i^{ch2}, and determining how they influence the isotope effects;
5) Determining the role of weakly bound van der Waals states of ozone, in the process of the ozone forming recombination reaction and in the isotope effects associated with it;

In this Chapter the topics 1 and 2 in the list above are discussed.

IV-2. Updated Values of Pathway-Specific Rate Coefficients

The following changes were made in this work, relative to the earlier work of Teplukhin et al.[14]:

a) The value of temperature was changed from 296 K used by Teplukhin to $T = 293$ K used here, since the experiments of Mauersberger were conducted at this temperature. Note that temperature enters the factor $e^{-\Delta \mathrm{ZPE}/kT}$ in all the equations derived above, the standard expressions for electronic Q_{el} and translational Q_{tr} partition functions (see Appendix), the ideal gas equation to determine concentration [M] at given pressure, and the formula for RMS speed of molecules to express k^{stab} through σ_{stab}. Since *T*-dependences are relatively smooth (the reactions are only slightly exo-ergic and endo-ergic), this correction resulted in a relatively small change.

b) In order to treat the upper and lower channels of the recombination reaction equally, the contributions of resonances below dissociation thresholds were neglected. Such contributions are typically small and originate from the numerical errors of calculations, that predict some non-zero widths (decay rates) to the states slightly below dissociation threshold, which is unphysical. In the previous work all bound states below the lower dissociation threshold ($E_i < 0$) were correctly neglected, but the resonances within ΔZPE energy range were allowed to decay onto both Channels 1 and 2. This is unphysical since the upper channel (Channel 1 in the singly substituted case and Channel 2 in the doubly substituted case) is still closed at energies $0 < E_i < \Delta\text{ZPE}$. Therefore, it makes sense to neglect the decay of resonances through the upper channel for $E_i < \Delta\text{ZPE}$. Moreover, the energy of dissociation thresholds grows with the quantum number K (body-fixed Z-projection of J), since for the symmetric-top rotor case this is a good quantum number that correlates with rotational quantum number j of the diatomic reagent (66, 68 or 88). For ozone molecule with the quantum number K only the states of a diatomic reagent with $j \geq K$ are permitted asymptotically, making the threshold energies rotation-dependent: $E_i > K(K+1)B_{\text{lower}}$ for the lower channel and $E_i > \Delta\text{ZPE} + K(K+1)B_{\text{upper}}$ for the upper channels. Note that the values of diatomic rotational constant B are different for the two channels and are different in the singly and doubly substituted cases too. The values of vibrational ΔZPE are also different in the singly and doubly substituted cases. And the upper and lower

Table 7. Theoretical and experimental and rate coefficients (in the units of 10^{-35} cm^6/s) for various pathways of ozone formation at room temperature in the cases of single and double isotopic substitution, and the corresponding isotope effects.

Source	Isotope subst.	κ_S	κ_A	κ_B	κ_I	ζ-effect	η-effect	ξ-effect
Theory, this work.	single	30	37	55	0.18	1.45	1.02	7.8
	double	31	29	73	1.41	1.38	1.08	
Experiment, Janssen et al[10]	single	30	43	55	0.36	1.55	1.16	4.8
	double	31	28	90	1.74	1.63	1.13	

channels switch in the singly and doubly substituted cases. Since the overall picture is this complex and it is hard to estimate the overall effect of all these

a) details, we decided, in the updated version of theory, to take into account all these factors, in order to avoid any bias. This modification also resulted in a relatively small change.

b) Finally, a bug was discovered in the code of Teplukhin, where the reduced mass of $^{16}O^{16}O$ was used erroneously for the pathway B in the doubly substituted case (should be $^{18}O^{18}O$). This was corrected in the updated version of the code and resulted in a significant change of κ_B and K^{ex}, but no change in the isotope effects where these two moieties enter together and the effect of the diatomic mass cancels.

My results for four pathways and three isotope effects are summarized in Table 7. The most significant new addition to the previous work is theoretical prediction of rate coefficients for the insertion pathways, κ_I, never computed before by anyone else. In agreement with experiment, our theory predicts very small rate coefficients for the

insertion pathway, in the range of two orders of magnitude smaller than rate coefficients for other three pathways. This is consistent with an *indirect* reaction path, that circles the origin in Figure 9, going from the reagent channel at the bottom of the figure (Channel 1 with a homonuclear diatomic) into the product well at the top of the figure (to form a symmetric ozone molecule). Absolute value of theoretically predicted κ_I is quite close to the experimental value in the case of double isotopic substitution (see Table 7), whereas it deviates more in the case of single isotopic substitution. One must remember, however, that dealing with the insertion pathway we look at relatively small rate coefficients influenced by both theoretical assumptions and experimental limitations.

Also, in agreement with experiment, our results indicate that the insertion is much slower in the singly substituted case compared to the doubly substituted case. In the experiment this ratio is larger than one, and its magnitude is $\xi = 4.8$. Importantly, our theory shows the same effect ($\xi > 1$) with even larger magnitude, $\xi = 7.8$.

The difference of experimental and theoretical absolute values of ξ-effect may originate in the approximate theoretical treatment of stabilization step (since we assume the same value of stabilization cross section for single and double isotopic substitutions, while they may be different in reality), or in the details of potential energy surface (since this indirect reaction path crosses several transition states, and thus is expected to be sensitive to the reaction landscape), or in the difficulties of experimental measurements (since this is a minor pathway with very small rate coefficient). Despite of these multiple uncertainties, a semiquantitative agreement of theory with experiment is obtained, which is already a successful first step.

An important qualitative question is why the insertion is much faster in the doubly substituted case:

$$6 + 88 \xrightarrow{\kappa_I} 868$$

compared to the singly substituted case:

$$8 + 66 \xrightarrow{\kappa_I} 686$$

Our tentative explanation is that this is because the insertion process is largely driven by quantum tunneling through several transition states, which is exponentially sensitive to the masses of isotopes. It may be counterintuitive at first, but it appears that the effective (reduced) mass of reagents in the doubly substituted case:

$$\mu^{(d)} = \frac{16\times36}{16+36} \approx 11.07 \text{ (amu)} \quad (169)$$

is appreciably smaller than in the singly substituted case:

$$\mu^{(s)} = \frac{18\times32}{18+32} \approx 11.52 \text{ (amu)} \quad (170)$$

Smaller effective mass is associated with more efficient tunneling, which may be a simple explanation of this phenomenon.

The rate coefficients κ_A, κ_B and κ_S for other three recombination pathways, as predicted by my calculations in Table 8, follow closely the trends we saw in the earlier work by Teplukhin et al.[14] Namely, ζ-effect driven by ΔZPE goes in the same direction as in the experiment ($\zeta > 1$) in both singly and doubly substituted cases, although in our calculations its magnitude is somewhat smaller, about $\zeta = 1.42 \pm 0.03$ in the singly and doubly substituted cases, respectively. Concerning the mysterious η-effect driven by symmetry, our updated results are still far from the experiment, giving rather small values of $\eta = 1.2$ and 1.8 in the singly and doubly substituted cases, respectively. The direction is consistent with experiment, though ($\eta > 1$ in both cases).

IV-3. Temperature Dependencies of Recombination Rates

Experimental data on temperature dependence of pathway-specific rate coefficients are very sparse. Janssen *et al* measured temperature dependencies of κ_B in singly and doubly substituted cases.[10] Note that this pathway is exo-ergic in the case of single substitution but is endo-ergic in the case of double substitution. In these experiments it was easier (and more accurate) to measure and report these rate coefficients not as absolute values, but relative to the temperature dependence on another pathways that is iso-ergic. Namely, for the case of single substitution they measured the ratio κ_B/κ_{888} whereas in the case of double substitution they measured the ratio κ_B/κ_{666}, where κ_{666} and κ_{888} correspond to the processes that involve only one isotope:

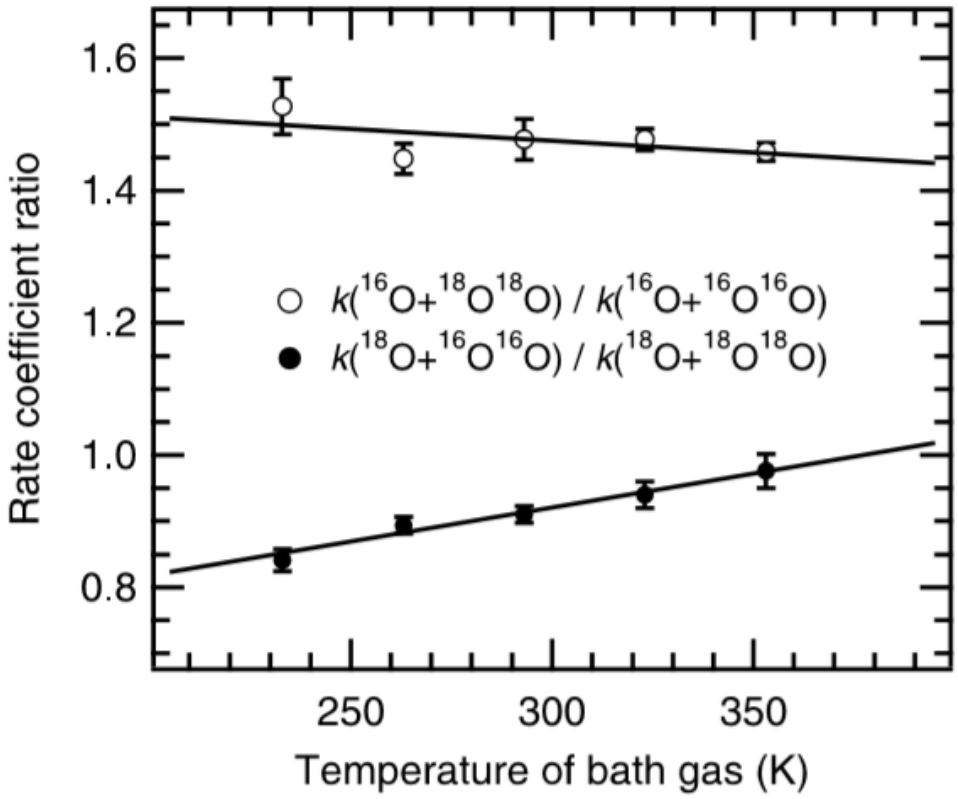

Figure 12. Experimental temperature dependence of k_B (rate coefficient for pathway B) relative to k_{888} in the case of single substitution, and relative to k_{666} in the case of double substitution.

Table 8. Experimental and theoretical slopes (gradients per 1000 K) obtained from temperature dependencies of pathway-specific rate coefficients at 300 K. Note that experiment and theory use different reference pathways.

Source	Reference pathway	Isotope subst.	κ_S/κ_{ref}	κ_A/κ_{ref}	κ_B/κ_{ref}	$\kappa_{ch2}/\kappa_{ref}$
Experiment, Janssen et al[10]	κ_{666}	single	~0.23(11)	?	+1.03(42)	~0.02(07)
		double	?	+1.3(6)	–0.15(48)	+0.66(32)
Theory, this work	κ_S	single	0.0d0	–0.302	+0.035	–0.311
		double		+0.085	–0.211	~0.087
	κ_{tot}	single	–0.004	–0.106	~0.015	–0.110
		double	–0.028	–0.011	–0.138	–0.039

$$6 + 66 \xrightarrow{\kappa_{666}} 666$$

$$8 + 88 \xrightarrow{\kappa_{888}} 888$$

Temperature dependence of the rate coefficient for formation of normal ozone is well known:[16]

$$\kappa_{666} = (60. \pm 10.) \times 10^{-35}\ (300\ \mathrm{K} / T)^{2.5\pm0.5}\ \mathrm{cm}^6/\mathrm{s}$$

The temperature dependence of κ_{888} is assumed to be roughly the same, with just a slightly larger absolute value of the rate coefficient: $\kappa_{888} = 1.02\ \kappa_{666}$.

Janssen *et al* argued that only exo-ergic pathways should have *T*-dependence, while endo-ergic and iso-ergic pathways should not. We don't quite agree with their logic. From Figure 12 clearly see that $\kappa_B^{(s)}$ for an exo-ergic pathway, indeed, exhibits

stronger positive *T*-dependence, but $\kappa_{\mathrm{B}}^{(\mathrm{d})}$ for an endo-ergic pathway also shows some negative *T*-dependence, although it is considerably weaker. Janssen *et al* claimed that this dependence is within experimental error and decided not to assign any meaning to it. Based on the entire bulk of data available for ozone isotopomers and isotopologues, some of which come from their group and some from other groups, they reported a list of slopes for *T*-dependencies of the pathway specific rate coefficients κ_{A}, κ_{B} and κ_{S} for single and double isotopic substitution, all relative to κ_{666}, which we reproduce here in Table 8. Most of these data were specifically reported by Janssen et al, but two entries marked by "?" were not. In principle they can be derived from experimental data alone, which we will do in the future.

Our theoretical predictions of temperature dependence for four pathway specific rate coefficients in the cases of single and double substitution are collected in Table 9. It is interesting to note that the values of rate coefficients κ_{S} for an iso-ergic recombination pathway S remain nearly the same in the cases of single and double substitution. So, this reaction pathway represents a convenient reference process (independent on the number of isotopic substitutions), relative to which the rate coefficients computed for all other pathways may be gaged.

Comparing T-dependence of the experimental reference pathway κ_{666} (see above) with T-dependence of κ_{S} (used as a reference for theoretical data), we found that experimental temperature dependence of κ_{666} is significantly sharper. This means that some of experimental T-dependence originates in the stabilization process, that in our calculations is treated in a simplified manner, using one constant value of stabilization cross section for all scattering resonances. In principle, introducing the dependence of

stabilization cross section on collision energy (on temperature of the bath gas) and on energy of the metastable state (energy of a resonance E_i) may help to improve comparison with experiment. This is one of our possible research directions that will be pursued soon. One can try to devise a semi-empirical stabilization model and tune the fitting parameters in order to match experimental T-dependence. For now, our analysis will be limited to the ratios of the rate coefficients, that are expected to be insensitive to the details of the stabilization model, since the same stabilization cross section enters numerator and denominator of a ratio and thus cancels. The exception to this would only be the model in which stabilization cross sections would depend on energies of the individual resonances, and thus would not factor out of the sum over resonances (Equations 48-49). Still, even in this most complicated case the ratio of rate coefficients would be less sensitive to the details of stabilization model, than the rate coefficients themselves.

In Table 10 we listed five ratios between various pathway-specific rate coefficients that we set up for the analysis of temperature dependence. Theoretical expressions for these ratios in terms of partition functions were obtained in Chapter III and collected in 8 above. In Figure 13 the temperature dependencies of all these ratios were plotted in the range $200 \leq T \leq 400$ K, fitted by quadratic function, and the value of slope at $T = 300$ K was determined and reported in Table 9.

Table 9. Temperature dependence of pathway specific recombination rate coefficients (3rd order, 10^{-35} cm^6/s) for singly and doubly substituted cases, computed theoretically for the range $200 \leq T \leq 400$ K.

T (K)	Singly substituted				Doubly substituted			
	κ_A	κ_B	κ_S	κ_I	κ_A	κ_B	κ_S	κ_I
200	46	66	37	0.29	35	92	38	2.63
250	41	60	33	0.22	31	81	34	1.84
300	36	54	30	0.17	28	72	30	1.36
350	32	49	27	0.14	26	64	27	1.05
400	29	44	25	0.12	23	58	25	0.83

Table 10. The slopes (gradients per 1000 K, at $T = 300$ K) for various ratios of the pathway-specific rate coefficients obtained from theoretically computed temperature dependencies.

Numbering of the ratios and their colors in Figure 13	Definition of the ratio		Gradient per 1000 K	
	Single subst.	Double subst.	Single subst.	Double subst.
R_1, red	$\frac{\kappa_A}{\kappa_S}$	$\frac{\kappa_A}{\kappa_S}$	–0.302	+0.085
R_2, green	$\frac{\kappa_B}{2\kappa_S}$	$\frac{\kappa_B}{2\kappa_S}$	+0.035	–0.211
R_3, blue	$\frac{K^{ex}\kappa_B}{\kappa_S}$	$\frac{\kappa_B}{K^{ex}\kappa_S}$	+0.475	–0.741
R_4, gray	$\frac{\kappa_B}{2\kappa_A}$	$\frac{\kappa_B}{2\kappa_A}$	+0.214	–0.341
R_5, black	$\frac{\kappa_B K^{ex}}{\kappa_A}$	$\frac{\kappa_B}{\kappa_A K^{ex}}$	+0.458	–0.920

From this figure we see that the ratios of exo-ergic and endo-ergic pathways, A or B, over the iso-ergic pathway S (given by R_1 and R_2, red and green curves), indicate positive and negative temperature dependencies, as expected, and this behavior is reversed in the cases of single and double substitutions (dashed and solid curves swap).Moreover, when the ratio of κ_{B} over κ_{A} is considered, the slop becomes larger in both

Table 11. The slopes (gradients per 1000 K, at $T = 300$ K) of the ratios of rate coefficients for singly and doubly substituted cases, using exo- and endo-ergic pathways A and B, and an iso-ergic pathway S.

Numbering of the ratios and their colors in Figure 14	Definition of the ratio	Gradient per 1000 K
R_1, red	$\frac{\kappa_{\mathrm{S}}^{(\mathrm{s})}}{\kappa_{\mathrm{S}}^{(\mathrm{d})}}$	+0.103
R_2, green	$\frac{\kappa_{\mathrm{A}}^{(\mathrm{s})}}{\kappa_{\mathrm{A}}^{(\mathrm{d})}}$	–0.303
R_3, blue	$\frac{\kappa_{\mathrm{B}}^{(\mathrm{s})}}{\kappa_{\mathrm{B}}^{(\mathrm{d})}}$	+0.239
R_4, gray	$\frac{\kappa_{\mathrm{B}}^{(\mathrm{d})}}{2\kappa_{\mathrm{A}}^{(\mathrm{s})}}$	–0.0331
R_5, black	$\frac{\kappa_{\mathrm{B}}^{(\mathrm{s})}}{2\kappa_{\mathrm{A}}^{(\mathrm{d})}}$	+0.0491

single and double substitutions (given by R_4, gray curves). Even larger slopes are obtained if we include in the ratio, with one of two competing pathways, the equilibrium

constant of isotope exchange K^{ex} (see R_3 and R_5, blue and black curves). In this case, the slopes close to 1.00 per 1000 K are obtained, close to the experimentally reported slopes.

We also tried to mix into one ratio the rate coefficients from singly and doubly

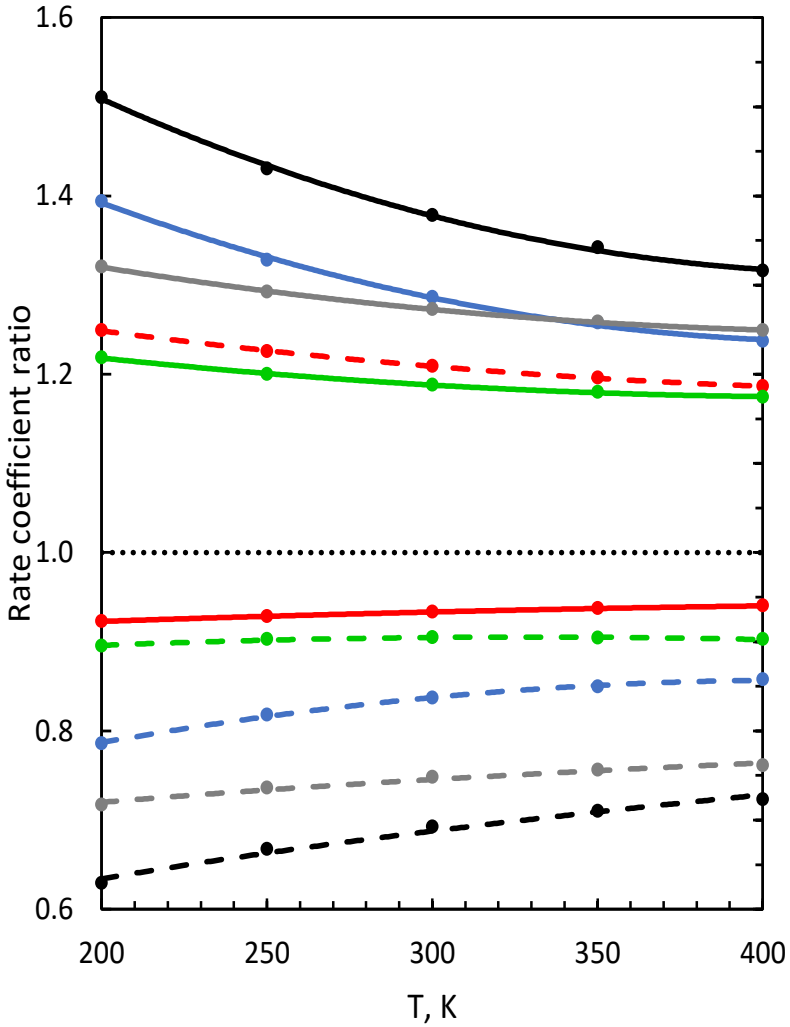

Figure 13. Temperature dependencies of the ratios of pathway-specific rate coefficients defined in Table 10 (see the Table for color assignments). Single and double isotopic substitutions are plotted by dashed and solid lines, respectively.

substituted cases, as summarized in Table 10.

Theoretical expressions for these ratios in terms of partition functions were

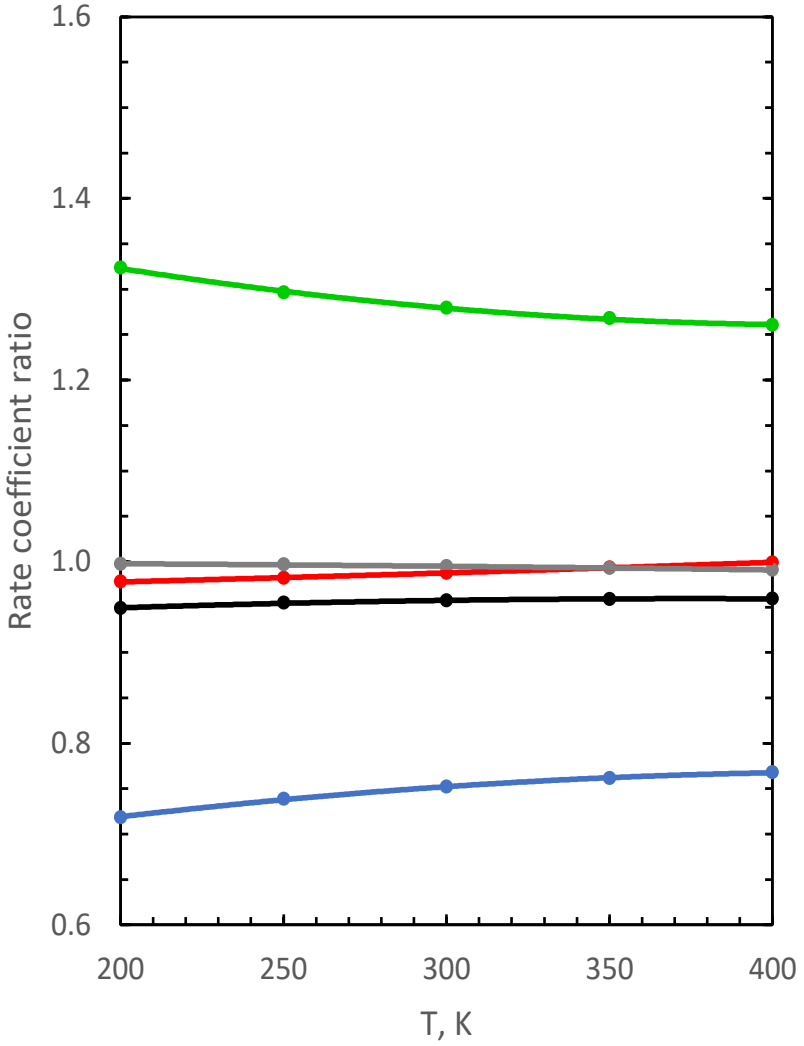

Figure 14. Temperature dependencies of various ratios of the pathway specific rate coefficients in singly and doubly substituted isotopologues, as defined in Table 11. Colors are assigned in the Table 11.

obtained in Chapter III and collected in Table 8 above. In Figure 14 the temperature dependencies of all these ratios were plotted in the range $200 \leq T \leq 400$ K, fitted by quadratic function, and the value of slope at $T = 300$ K was determined and reported in Table 11.

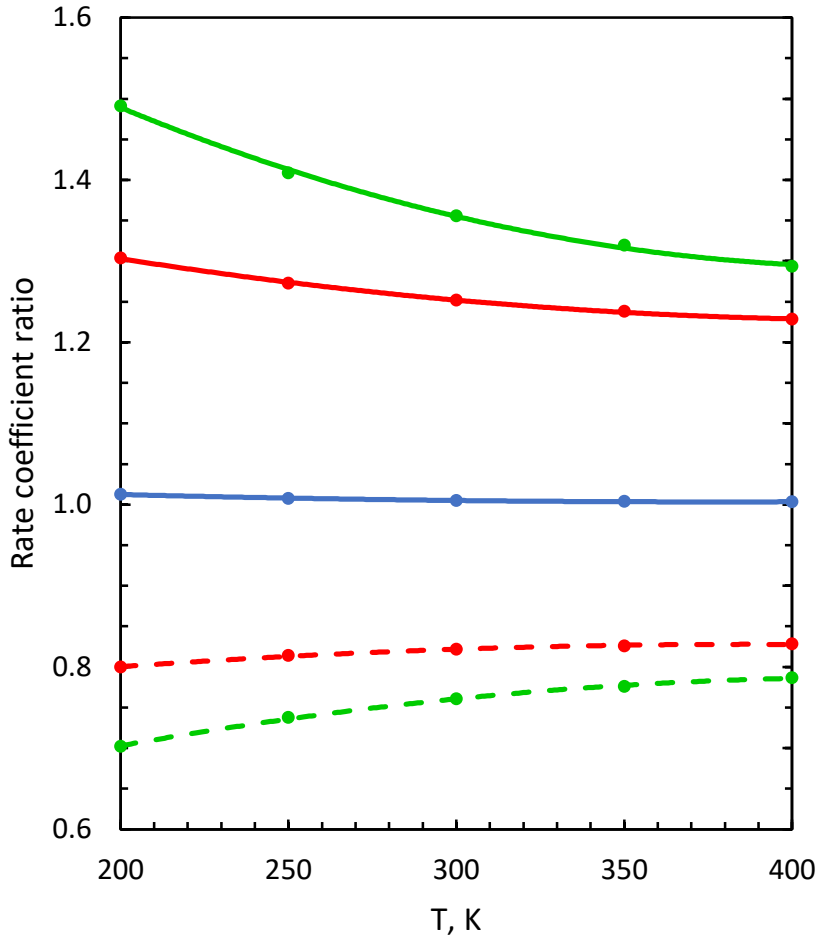

Figure 15. Temperature dependencies of various ratios of channel-specific rate coefficients (upper vs lower channels), as defined in Table 12. Colors are assigned in Table 12. Single and double isotopic substitutions are plotted by dashed and solid lines, respectively.

In this figure, one of the ratios, that of two iso-ergic pathways S in the cases of single and double substitution, has basically no *T*-dependence (given by R_1, red). Two ratios of endo- to endo-ergic and exo- to exo-ergic exhibit relatively weak *T*-dependence (given by R_4 and R_5, gray and black). The remaining two ratios (given by R_2 and R_3, green and blue) correspond to endo- to exo-ergic and exo- to endo-ergic and show significant slopes.

Finally, we will check the temperature dependence of the ratios of channel-specific rate coefficients for the lower and upper channels (Channel 1 vs Channel 2) in the singly and doubly substituted cases. Theoretical expressions for these ratios in terms of partition functions were obtained in Chapter III and collected in Table 8 above. In Figure 15 the temperature dependencies of all these ratios were plotted in the range $200 \leq T \leq 400$ K, fitted by quadratic function, and the value of slope at $T = 300$ K was determined and reported in Table 12.

Recall that the upper and lower channels switch when we go from single to double substitution of isotopes. From Figure 15 we see that *T*-dependence switches from positive to negative, accordingly (given by R_1, red dashed and solid lines). Larger slopes are obtained if we include in the ratio the equilibrium constant of isotope exchange K^{ex} between the two channels (see R_2, green curves). Again, large slopes close to 1.00 per 1000 K are obtained, close to the experimentally reported slopes. The last curve (R_2, blue) has no slope, indicating similar *T*-dependencies of the total reaction rate coefficients for single and double isotopic substitutions.

Table 12. The slopes (gradients per 1000 K, at $T = 300$ K) for the ratios of channel-specific rate coefficients obtained from theoretically computed temperature dependencies.

Numbering of the ratios and their colors in Figure 15	Definition of the ratio		Gradient per 1000 K	
	Singly subst.	Doubly subst.	Singly subst.	Doubly subst.
R_1, red	$\frac{\kappa_{\mathrm{ch1}}}{\kappa_{\mathrm{ch2}}}$	$\frac{\kappa_{\mathrm{ch1}}}{\kappa_{\mathrm{ch2}}}$	+0.137	–0.360
R_2, green	$2K^{\mathrm{ex}}\frac{\kappa_{\mathrm{ch1}}}{\kappa_{\mathrm{ch2}}}$	$\frac{2}{K^{\mathrm{ex}}}\frac{\kappa_{\mathrm{ch1}}}{\kappa_{\mathrm{ch2}}}$	+0.413	–0.932

R_3, blue	$2\frac{\kappa_{\mathrm{tot}}^{(\mathrm{s})}}{\kappa_{\mathrm{tot}}^{(\mathrm{d})}}$	–0.0437

These theoretically derived data are in qualitative agreement with experimental temperature dependencies, but not in quantitative agreement. Which make us to believe that, in order to improve comparison with experiment, we have to modify our description of the stabilization step, making it *T*-dependent and may be sensitive to the energy difference between the two channels. This idea is further developed in the Summary section of this chapter.

IV-4. Temperature Dependencies of Isotope Effects

Theoretically predicted temperature dependencies of the three distinct isotope effects in ozone (ζ-effect, η-effect and ξ-effect, as defined in Chapter III), are reported in Table 13 below. The value of ξ drops significantly at temperature is raised, which is consistent with our interpretation of ξ-effect as being driven by quantum tunneling, since the role of tunneling is expected to reduce at higher temperatures. The value of ζ-effect, driven by quantum zero-point energy difference, also drops as temperature is raised. This is expected, since the role of a narrow ΔZPE energy range at the lower part of the resonance spectrum is expected to decrease as temperature is raised and the equilibrium population of the upper states increases. Unfortunately, there are no experimental data on temperature-dependencies of these two isotope effects. A direct comparison with experiment is not readily possible at this time. It makes sense, however, that two isotope effects that originate in quantum mechanics tend to reduce at high temperature, when the system becomes more classical.

In contrast, with the other two isotope effects, η-effect remains relatively stable with respect to the variations of temperature. This, again, is consistent with the hypothesis that symmetry is somehow responsible for this isotope effect. In Figure 16 temperature dependencies of ζ-effect and η-effect are plotted for singly and doubly substituted cases. We see that as temperature is raised, the values of η-effect in the singly and doubly substituted cases approach each other, both remaining relatively small.

Table 13. Temperature dependence of isotope effects for singly and doubly substituted cases, computed theoretically for the range $200 \leq T \leq 400$ K.

T, K	ζ-effect		η-effect		ξ-effect
	Singly subst.	Doubly subst.	Singly subst.	Doubly subst.	
100	2.12	1.90	0.973	1.218	10.08
150	1.76	1.64	1.001	1.147	9.76
200	1.59	1.51	1.014	1.114	9.15
250	1.50	1.43	1.019	1.095	8.46
300	1.44	1.38	1.020	1.084	7.81
350	1.41	1.34	1.020	1.075	7.25
400	1.38	1.32	1.020	1.070	6.77

Experimental data on temperature dependence of η-effect are available from the work of Janssen[43] for the case of single substitution. This phenomenon received more attention because it is directly responsible for generation of the anomalous mass independent fractionations of oxygen isotopes in Earth's atmosphere. Experimental data of Janssen are reproduced here in Figure 18, although it should be mentioned that his definition of isotope effect is different from ours, by a factor of two. His values of "r_{50}" are on the order of two, with a perfect 2.00 corresponding to no anomalous isotope effect. For us, the values of η are on the order of one, with perfect 1.00 being the reference for no anomalous isotope effect.

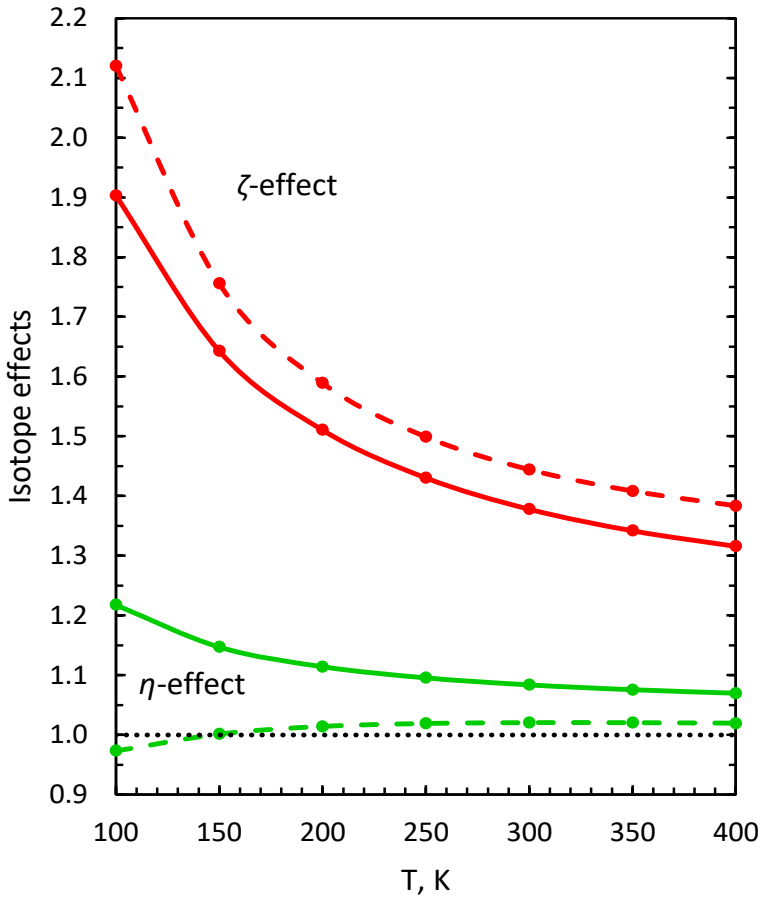

Figure 16. Temperature dependencies of isotope effects in singly (dashed line) and doubly (solid line) substituted ozone molecules, computed using our theoretical model.

In order to make a one-to-one comparison, we took his raw data, divided by two, and plotted together with our data in Figure 17 below. From this graph we see that our theoretical prediction behaves qualitatively similar to the experimental dependence in the low temperature range of the interval. At $T \sim 200$ K, which is the temperature of Earth's stratosphere, the magnitude of η-effect predicted by our theory is in very good agreement with experimentally derived data. The difference increases at temperature is raised, which again can be attributed to the approximate treatment of the stabilization step in the present version of our theory, where one value of stabilization cross section is used, without any temperature dependence included.

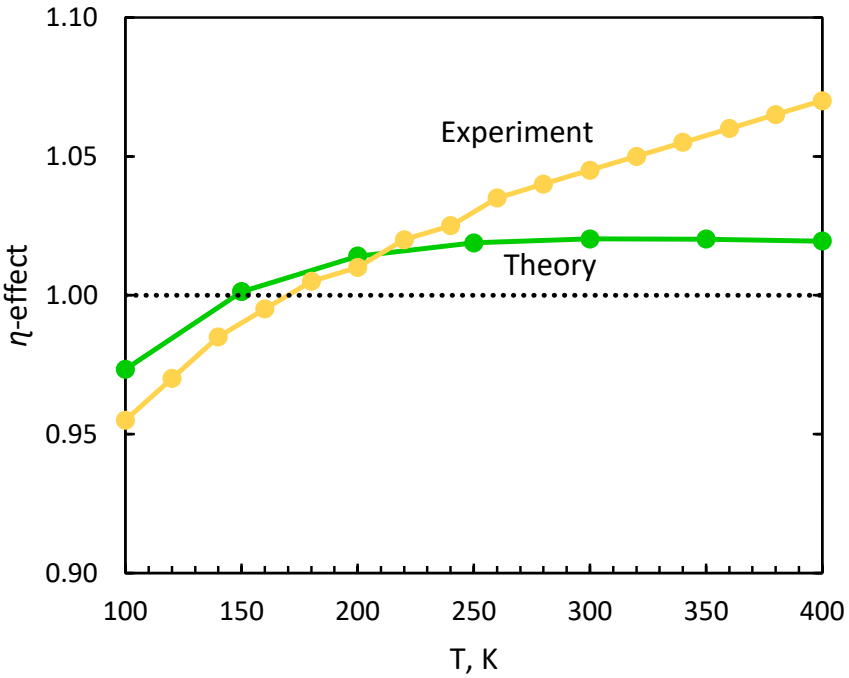

Figure 17. Theoretical (green) and experimental (orange) temperature dependencies of symmetry-driven isotope effect, the η-effect, in the case of single isotopic substitution.

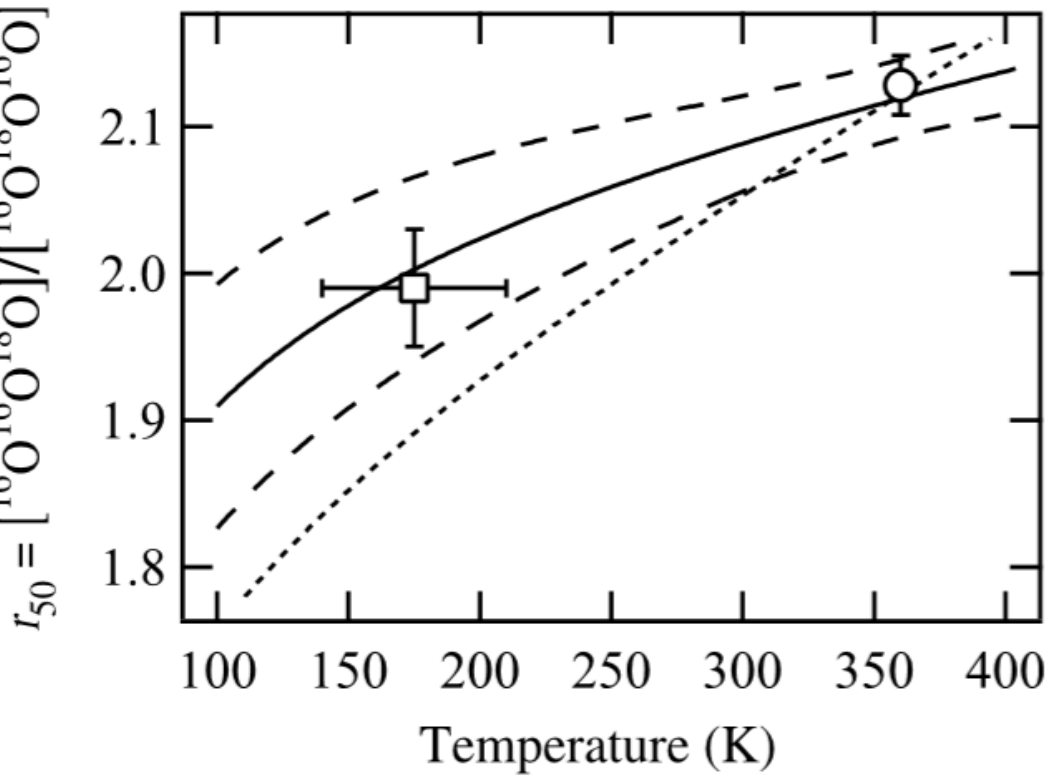

Figure 18. Temperature dependencies of isotope η-effect according to Janssen[10] for singly substituted molecule.

IV-5. Summary

The general theory of four pathways-specific rates of the recombination reaction that forms ozone, developed in Chapters II and III, was employed here to compute all possible rate coefficients for singly and doubly substituted ozone molecules. This includes a (minor) insertion pathway for singly and doubly substituted cases, which was theoretically studied for the first time, to our best knowledge. Insertion is an indirect reaction path that crosses several wells and transition states on the PES and includes isomerization by roaming. Such process is a rare event with small rate coefficient, that is hard to compute theoretically. We captured this process using a rigorous quantum mechanical approach that permits to split the overall decay rate onto the channel-specific decay rates, by setting the complex absorbing potentials in the individual channels, one at a time. The values of predicted rate coefficients κ_{I} are in good agreement with experiment. This is encouraging, given complexity of the process from both experimental and theoretical study standpoints. Moreover, the large isotope effect associated with the insertion of a light atom into a heavy diatom, vs the insertion of a heavy atom into a light diatom, also seems to be in a qualitative agreement with experiment. This is particularly encouraging since isotope effect represents a very sensitive probe of a chemical process.

Rate coefficients for the other three (major) reaction paths, κ_{A}, κ_{B} and κ_{S}, were updated to fix several issues discovered in the earlier implementation of our theory. Absolute values of these rate coefficients are also in good agreement with experimental data. They indicate two definite isotope effects, driven by quantum zero-point energy difference, and by molecular symmetry. In particular, quantum ζ-effect is in good agreement with experiment for both single and double isotopic substitution. The

mysterious η-effect is also qualitatively correct, featuring formation of asymmetric ozone molecule over symmetric once, but in comparison with experiment its magnitude is too small. This question is extremely important for explanation of the anomalous mass-independent enrichments of oxygen atoms in the atmosphere, and therefore it will be in a focus of the future work.

Systematic study of temperature dependence of the pathway-specific rate coefficients, and of the isotope effect associated with formation of symmetric and asymmetric ozone molecules, and the comparison of theoretically predicted data *vs* available experimental information, all suggest that an improvement of a simplified stabilization model that we use in the present version of our theory is needed. Incorporation of temperature dependent stabilization cross section is likely to improve comparison with experiment. Moreover, making stabilization model sensitive to the type of a reaction channel (upper vs lower channel on the PES, Channel 1 vs Channel 2) is likely to help too. These questions will be addressed in the next stage of the project.

CHAPTER V. PROPERTIES OF SCATTERING RESONANCES IN OZONE AND THEIR ROLE IN THE ISOTOPE EFFECTS

V-1. Introduction

Our database of the rovibrational states[44] of ozone includes 380434 states of singly substituted isotopologue and 400183 states of doubly substituted isotopologue, at energies up to 800 cm^{-1} above dissociation threshold, computed for the values of total angular momentum of the molecule from $J = 4$ to $J = 56$ with a step of 4, within the symmetric-top rotor approximation for the values of K from zero to $K = J$, with a step of 2. Out of these states 380434, about 250692 states are the bound states below dissociation threshold, whereas the remaining 129742 states are scattering resonances above threshold. The kinetics model developed in Chapters II, III and IV uses properties of all these scattering resonances (E_i, Γ_i^{ch1}, Γ_i^{ch2}, p_i^{sym}, p_i^{asym}) as input parameters, to compute the relevant channel-specific, product-specific, and pathway-specific dynamical partition functions ($\tilde{Q}_{\mathrm{sym}}$, $\tilde{Q}_{\mathrm{asym}}$, $\tilde{Q}_{\mathrm{ch1}}$, $\tilde{Q}_{\mathrm{ch2}}$, $\tilde{Q}_{\mathrm{A}}$, $\tilde{Q}_{\mathrm{B}}$, $\tilde{Q}_{\mathrm{S}}$, $\tilde{Q}_{\mathrm{I}}$) and predict the corresponding recombination rate coefficients (κ_{sym}, κ_{asym}, κ_{ch1}, κ_{ch2}, κ_{A}, κ_{B}, κ_{S}, κ_{I}), and deduce the isotope effects (ζ, η, ξ).

Although all scattering resonances are included in the dynamical partition functions $\tilde{Q}$ listed above, different resonances exhibit different properties, and these properties vary dramatically through the data set. Therefore, different resonances make different contributions to the rate of the reaction, and to the nascent isotope effects. In this chapter we will take much closer look at the distribution of resonance widths Γ_i (decay rates, inversely proportional to their lifetimes), and at the properties of resonance wavefunctions, trying to deduce a correlation.

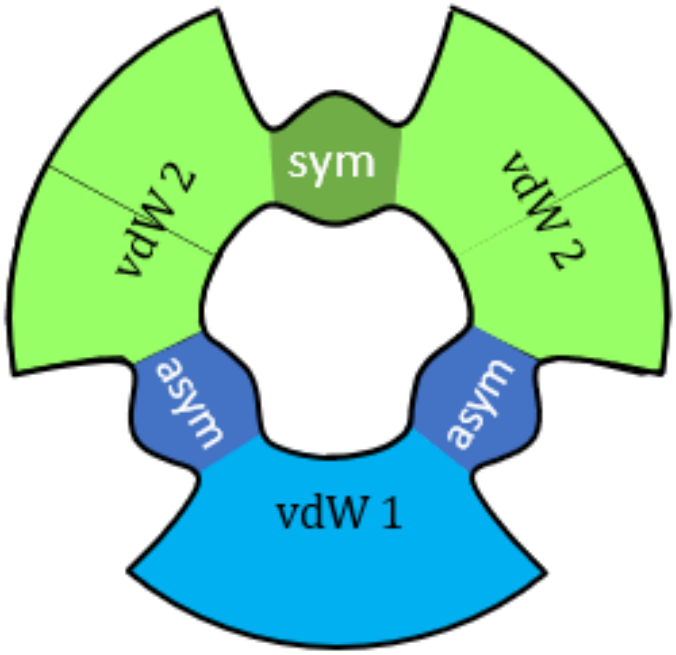

Figure 19. Probability in the van der Waals 1 (light blue) and van der Waals 2 (light green colors); asymmetric (blue) and symmetric (green) regions.

Obviously, it is impossible to plot and visually analyze the 3D wavefunctions for all states of the dataset, but this is unnecessary. The most important property of the wavefunction is the distribution of probability amplitude over different parts of the potential energy surface. Namely, the PES of ozone (see Figure 19) contains three deep localized wells that correspond to the stable symmetric and asymmetric ozone molecules with covalent bonds. Those wells are connected, through relatively tight transition states (bottlenecks in Figure 19), to the shallow and broad plateaus that host the weakly-bound van der Waals complexes in the two channels (Channel 1 and Channel 2). So, for each state, our database contains four probabilities, obtained by integrating its wavefunction over four regions of the PES: p_i^{sym}, p_i^{asym}, p_i^{vdw1}, p_i^{vdw2}. The corresponding areas of the PES are shown in Figure 19 by color.

The total covalent probability is $p_i^{\mathrm{cov}} = p_i^{\mathrm{sym}} + p_i^{\mathrm{asym}}$, while the total van der Waals probability is $p_i^{\mathrm{vdw}} = p_i^{\mathrm{vdw1}} + p_i^{\mathrm{vdw2}}$. From these two data, we can also compute, for each state, the probability of wavefunction in the asymptotic range of the PES: $p_i^{\mathrm{free}} = 1 - p_i^{\mathrm{vdw}} - p_i^{\mathrm{cov}}$, associated with the unbound (scattering) state behavior, similar to free particle states discussed in Chapter I (see Figure 4). In order to visualize the distribution of three probabilities (p_i^{cov}, p_i^{vdw}, p_i^{free}) over the data set, we use the Dalitz plot analysis.[45] This method allows to visualize the correlation between three properties, such that (in our case) $p_i^{\mathrm{cov}} + p_i^{\mathrm{vdw}} + p_i^{\mathrm{free}} = 1$. This plot has three axes, and a triangular area between them to place data points. In Figure 20 the distribution for the singly substituted ozone molecule is presented (the case of double substitution looks similar).

It appears that the complexity of the PES of ozone is responsible for appearance of a broad distribution of properties of its states. One can see a significant probability in the "covalent corner" of the plot, but even more probability is located in the "van der Waals corner" of the plot, which means that many states of ozone exhibit a van der Waals behavior, with wavefunctions located mostly outside of the transition states. So, both kinds of resonances are possible in ozone. The mixed states are also present, and our data show that the majority of points deviate significantly from the right side of triangle that connect the covalent corner with the van der Waals corner of this graph. This means that, when the covalent states and the van der Waals states mix, they also mix with the continuum (free particle) states in the asymptotic part of the PES. Our conclusion is that the majority of scattering resonances in ozone are mixed and can't be attributed to one or another type.

Although it is impossible to rigorously split the resonance states of ozone onto two or three groups, it is possible to determine the contribution of each state-kind to the overall reaction rate, and the resultant isotope effect, using the values of p_i^{cov}, p_i^{vdw} and p_i^{free}. It is also possible to determine the average properties of the states of each kind, such as average resonance width, as done in the following section.

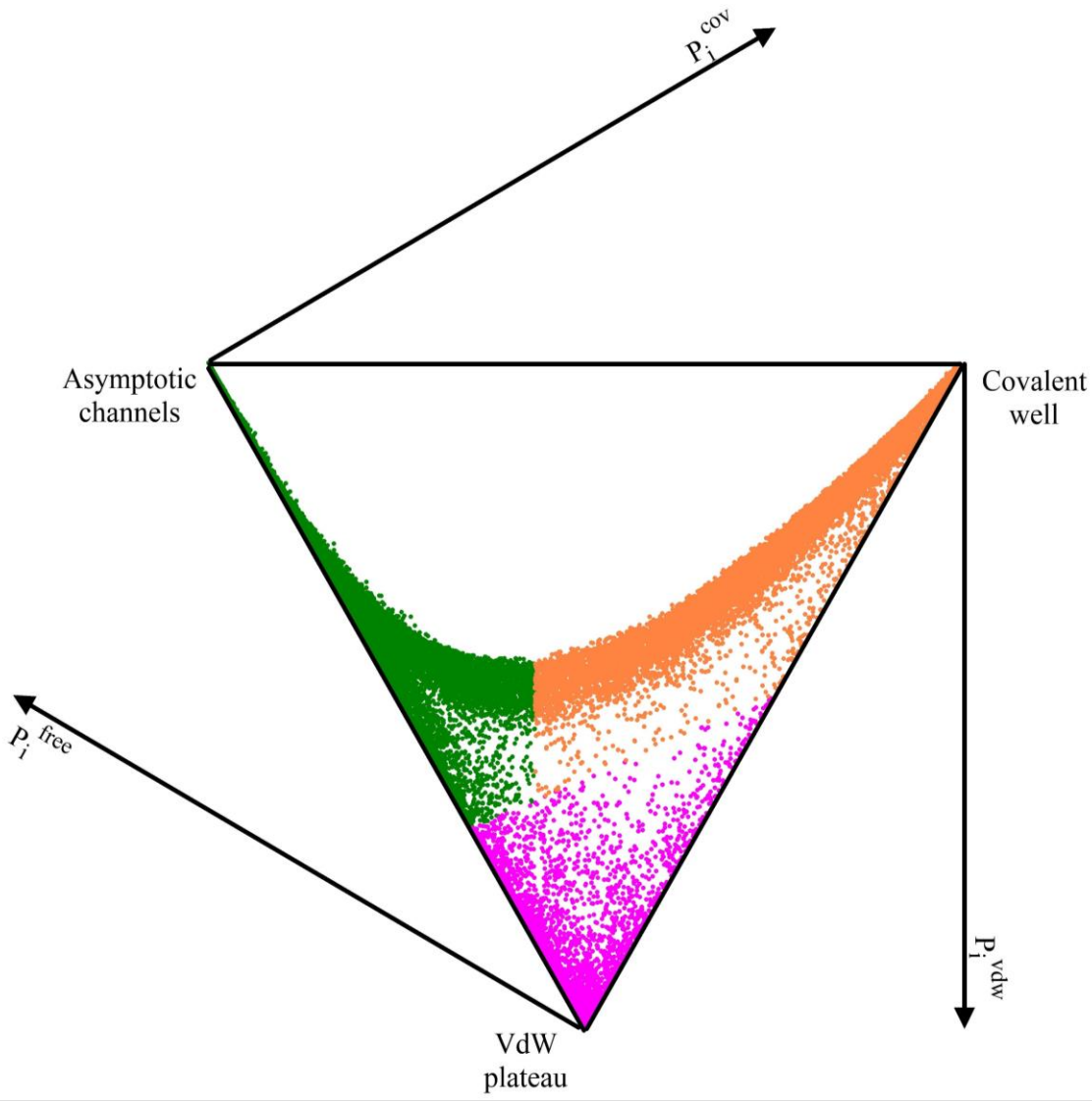

Figure 20. Dalitz-plot analysis of the p_i^{cov} versus p_i^{vdw} versus p_i^{free} for the scattering resonances in ozone. Upper right corner corresponds to the pure covalent states, lower corner corresponds to the pure van der Waals states, while upper left corner corresponds to the free particle states (unbound). The points distributed through the area of triangle exhibit all three probabilities.

V-2. Distribution of Resonance Widths

In this chapter the goal is to explore a broad distribution of resonance properties, such as their widths, or lifetimes. Resonances with different properties make drastically different contributions to the reaction rate and the isotope effects, but here we don't necessarily want to disregard resonances based on the value of their widths. In contrast, we want, first, to see and understand the spectrum of resonance widths, in a broad range. For this purpose, a convenient measure of resonances contribution is their dynamical partition function in the low-pressure limit given by Equations 99 and 149 for singly and doubly substituted cases, such as:

$$\tilde{Q}^{\circ}_{\mathrm{tot}} = \sum_{i} (2J+1)\, p_i^{\mathrm{tot}}\, e^{-\frac{E_i}{kT}}$$

This moiety still takes into account the energy of each resonance through the Boltzmann factor, and counts in the rotational state degeneracy, but the dynamical weights of all resonances are set to one, regardless of their width (there is no dependence on Γ_i in this formula, so, all values of Γ_i are equally weighted). We can also set $p_i^{\mathrm{tot}} = 1$ for now.

In Figure 21 we plotted a "raster" image of $\tilde{Q}^{\circ}_{\mathrm{tot}}$ vs Γ (to be exact, vs Γ_i^{tot}) obtained as a histogram with boxes generated using a log-scale for Γ_i. This can be thought of as $\tilde{Q}^{\circ}_{\mathrm{tot}}$ stretched along the Γ-axis, so that the sum of values in the histogram boxes gives the total value of $\tilde{Q}^{\circ}_{\mathrm{tot}}$ in the equation above. The range of resonance width is eight orders of magnitude broad, from extremely narrow, $\Gamma \sim 10^{-6}$ cm^{-1}, to very broad resonances

reaching $\Gamma \sim 100$ cm^{-1}. The data for singly and doubly substituted molecules are presented in Figure 21 separately. They both indicate that the overall distribution is likely to represent a convolution of three components that dominate in three ranges of Γ. These are shown by dashed straight lines: $\Gamma < 0.01$ cm^{-1}, $0.01 < \Gamma < 10$ cm^{-1} and $\Gamma > 10$ cm^{-1}.

Our theory gives an efficient, simple, and rigorous method for "deconvolution" of this distribution, by splitting the total probability, and the total partition function onto three:

$$p_i^{\mathrm{tot}} = 1 = p_i^{\mathrm{cov}} + p_i^{\mathrm{vdw}} + p_i^{\mathrm{free}}$$

$$\tilde{Q}^{\circ}_{\mathrm{tot}} = \tilde{Q}^{\circ}_{\mathrm{cov}} + \tilde{Q}^{\circ}_{\mathrm{vdw}} + \tilde{Q}^{\circ}_{\mathrm{free}}$$

The results of this deconvolution are presented separately for singly substituted case in Figure 22a and for doubly substituted case in Figure 22b. We see that it works

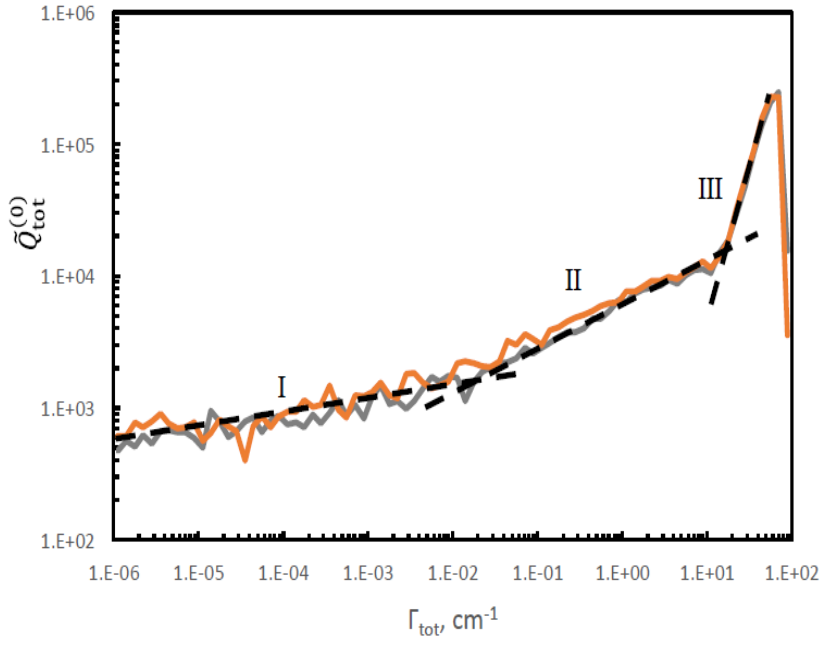

Figure 21. Distribution of resonance widths in singly (grey) and doubly (orange) substituted ozone molecules. Three ranges with different trends can be identified (shown by dashed lines).

well in each case. In the log-log scale used for these histograms the distribution of resonance widths for the covalent well states of ozone cover a broad range $\Gamma < 5$ cm^{-1}, growing roughly linearly, but then drops quickly. At that same point the number of free-particle states starts growing rapidly into the range $\Gamma > 5$ cm^{-1}. The distribution of the van der Waals states overlaps with both of them, covering the range $\Gamma >$ 10-3 cm^{-1}, and also growing roughly linearly (in this log-log plot).

The characteristic values of resonance widths for these three kinds of states can be computed as average using the following formula:

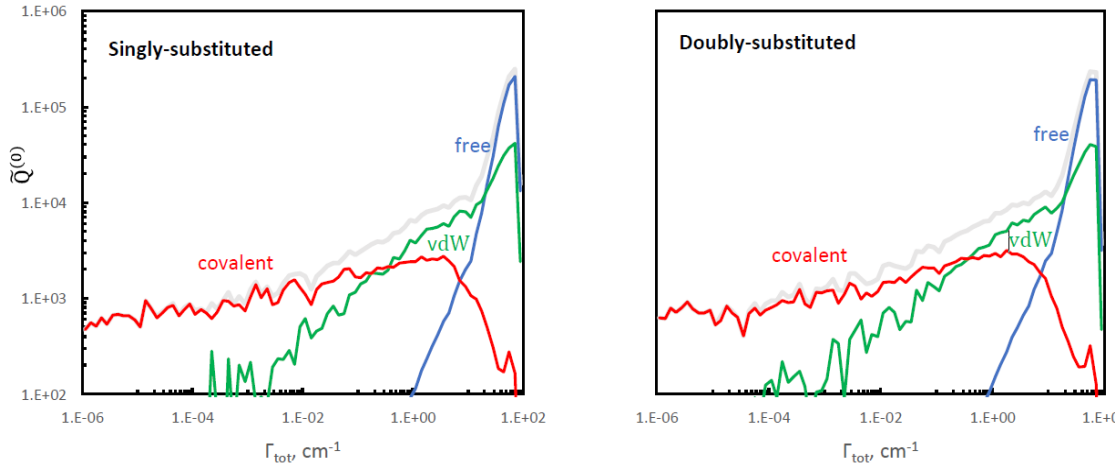

Figure 22. Deconvolution of the overall distribution of resonance widths in the singly substituted ozone onto three component that correspond to the covalent well states (red), van der Waals plateau states (green), and the continuum states in the asymptotic region of the PES (blue). Their total (gray) is the same as in Figure 21.

$$\tilde{\Gamma}_{\mathrm{cov}} = \frac{\sum_i \tilde{Q}_i^{\mathrm{cov}} \Gamma_i}{\sum_i \tilde{Q}_i^{\mathrm{cov}}}$$

$$\tilde{\Gamma}_{\mathrm{vdw}} = \frac{\sum_i \tilde{Q}_i^{\mathrm{vdw}} \Gamma_i}{\sum_i \tilde{Q}_i^{\mathrm{vdw}}}$$

$$\tilde{\Gamma}_{\mathrm{free}} = \frac{\tilde{Q}_i^{\mathrm{free}} \Gamma_i}{\sum_i \tilde{Q}_i^{\mathrm{free}}}$$

where $\tilde{Q}_i^{xxx} = (2J+1)\, e^{-\frac{E_i}{kT}}\, w_i\, p_i^{xxx}$ is a contribution of each resonance into the dynamical partition function $\tilde{Q}$, used here as a weighting factor in the averaging. The values of $\tilde{Q}_i^{\mathrm{cov}}$, $\tilde{Q}_i^{\mathrm{vdw}}$ and $\tilde{Q}_i^{\mathrm{free}}$ are obtained by substitution of p_i^{cov}, p_i^{vdw} and p_i^{free} into this formula. These data are presented in Table 14. They indicate that in ozone the resonances localized in the covalent well are much narrower (more stable) than those distributed over the van der Waals plateau. Indeed, the covalent states are trapped behind the transition state and therefore they must decay slower (and are populated slower too). In contrast, the wave functions of the van der Waals states are located outside of the transition state, very close to the dissociation channel. Therefore, they are less stable, they decay (and are populated) much faster.

Table 14. Average resonance widths and their corresponding lifetimes for the resonances of three kinds in singly and doubly substituted ozone molecules.

Resonance kind	$\tilde{\Gamma}(\mathrm{cm}^{-1})$		$\tilde{\tau}(\mathrm{ps})$	
	Single sub.	Double sub.	Single sub.	Double sub.
Covalent well	1.00	1.01	34	34
Van der Waals plateau	27.93	26.94	932	899
Free-particle states	68.91	67.33	2299	2246

V-3. Resonance Widths in Symmetric and Asymmetric Ozone Molecules

It was argued by several authors [Janssen, Marcus, F. Robert] that the lifetimes of resonances in symmetric and asymmetric ozone molecules may be quite different, and this may explain the mysterious symmetry-driven η-effect. Lifetimes are inversely proportional to resonance widths, so, here we will look at the distributions of resonance widths in symmetric and asymmetric ozone molecules. This way we can check this hypothesis.

First, we will deal with the covalent states of ozone because this is easier. We can readily split the overall covalent probabilities between the wells that hold symmetric and asymmetric ozone molecules: $p_i^{\mathrm{cov}} = p_i^{\mathrm{sym}} + p_i^{\mathrm{asym}}$. The corresponding partition functions were derived in the previous chapters, see Equations 100-101 for singly and 150-151 for doubly substituted ozone. Figure 23 compares the contributions of symmetric and asymmetric ozone molecules in the cases of single and double substitutions. For convenience of comparison, the data for symmetric ozone molecules were multiplied by 2, in order to offset the effect of symmetry (without this factor, the sum of two curves in the left and right frames of Figure 23 gives grey curves in Figures (23a) and (23b), respectively). One can see that these distributions are very similar for symmetric and asymmetric ozone molecules in both cases of single and double isotopic substitutions.

The average values of resonance width in symmetric and asymmetric ozone molecules were computed using these distributions and are summarized in Table 15. We see that the average values of widths are also very similar in symmetric and asymmetric ozone isotopomers, for both single and double isotopic substitutions.

Table 15. Average resonance widths and their corresponding lifetimes for the resonances localized over the covalent well of symmetric and asymmetric ozone molecules in the cases of single and double substitution.

Isotopomer of ozone	$\tilde{\Gamma}(\mathrm{cm}^{-1})$		$\tilde{\tau}(\mathrm{ps})$	
	Single sub.	Double sub.	Single sub.	Double sub.
Symmetric	1.22	0.91	41	30
Asymmetric	1.17	0.94	39	31

In order to run similar analysis for the van der Waals states of ozone we have to

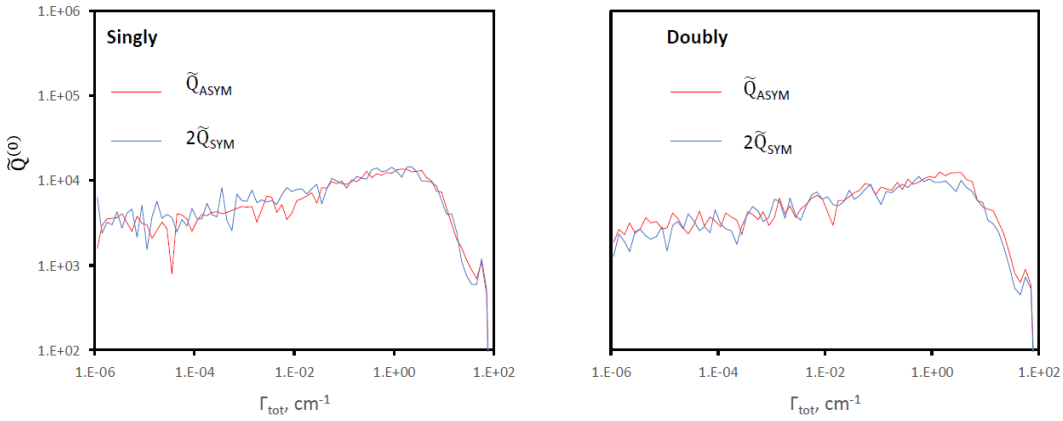

Figure 23. Distribution of resonance widths for the covalent states in asymmetric (red) and symmetric (blue) ozone molecules. Left and right frames correspond to single and double isotopic substitutions. To simplify the comparison, we plotted Q_{asym} and $2Q_{\mathrm{sym}}$ in order to offset the effect of symmetry.

split p_i^{ydw2} (the value of van der Waals probability in the Channel 2) between symmetric

and asymmetric ozone molecules. Although this could in principle be done rigorously, by integrating the wavefunctions of resonances over the corresponding parts of the PES as shown in Figure 24 below, this information was not computed by Teplukhin in the past and is not available from our database. One thing we can easily try is to split the values of

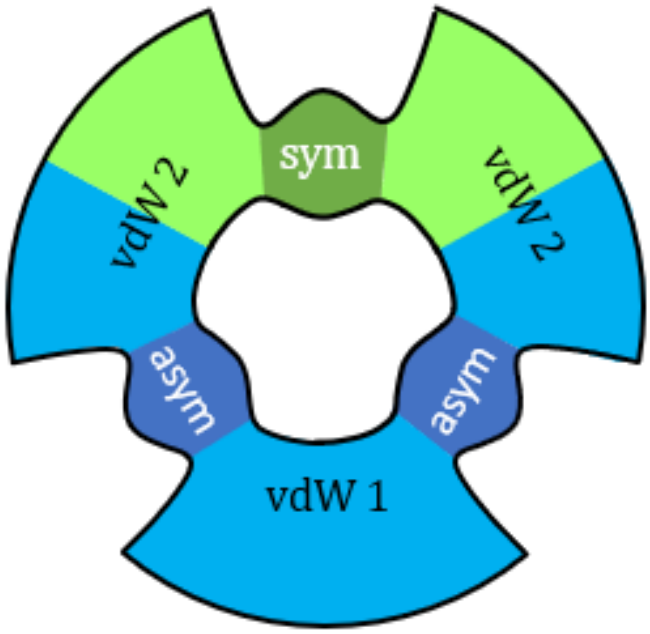

Figure 24. Simple splitting of probability in the van der Waals plateaus of the PES (light blue and light green colors) between asymmetric (dark blue) and symmetric (dark green) ozone molecules.

p_i^{vdw2} in halves, assigning equal parts of p_i^{vdw2} to symmetric and asymmetric ozone molecules. From Figure 24 we see that this corresponds to assigning $p = \frac{1}{2} p_i^{\mathrm{vdw2}}$ to symmetric ozone and assigning $p = p_i^{\mathrm{vdw1}} + \frac{1}{2} p_i^{\mathrm{vdw2}}$ to asymmetric ozone.

The results of such analysis are presented in Figure 24 and the average values of widths are added to the Table 14. We see that, again, the distributions of resonance widths are very similar in symmetric and asymmetric cases, in both isotopomers (singly and doubly substituted). The average values of widths are also very similar. One thing we can notice from Table 14 is that the value of average width is much larger for the van der Waals resonances, in comparison with the resonances localized over the covalent well.

V-4. Empirical Model for Splitting the Van der Waals Probabilities

What if in reality the van der Waals probability in the Channel 2 is not equally split between symmetric and asymmetric ozone molecules? What if there is a bias towards one of two isotopomers? A bias of this sort can be caused by the mode specificity, in which the van der Waals states would exhibit a local mode character and

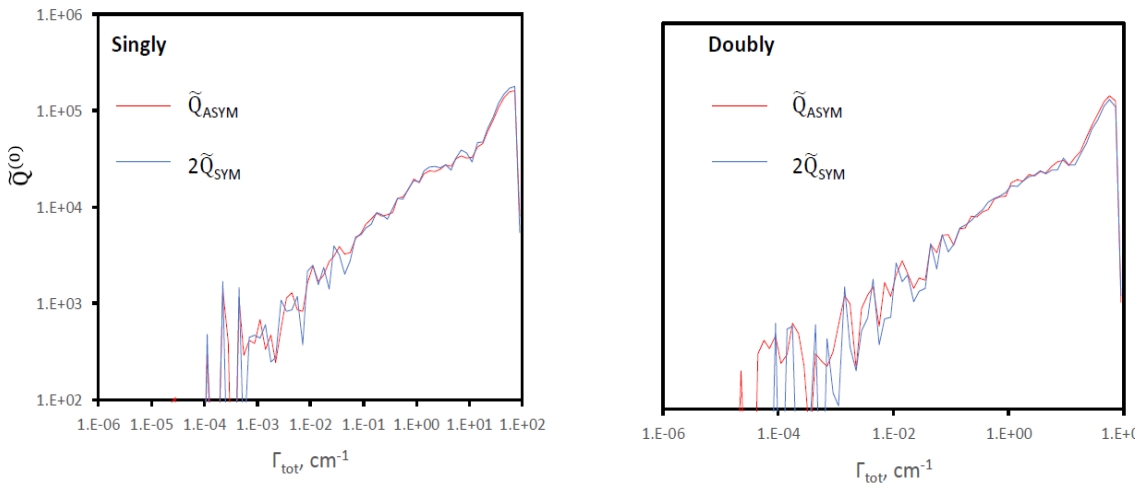

Figure 25. Distribution of resonance widths for the van der Waals states in asymmetric (red) and symmetric (blue) ozone molecules. Left and right frames correspond to single and double isotopic substitutions. To simplify the comparison, we plotted Q_{asym} and $2Q_{sym}$ in order to offset the effect of symmetry. In this analysis, van der Waals probability in Channel 2 was split in halves between symmetric and asymmetric isotopologues, as shown in Figure 24.

would lean more closely toward one or the other isotopomer. For each individual state,

the bias would depend on the probabilities of wavefunction in the covalent wells of symmetric and asymmetric ozone molecules, or namely, by:

$$p = \left(\frac{p_i^{\text{sym}}}{p_i^{\text{sym}} + p_i^{\text{asym}}}\right) p_i^{\text{vdw2}} \tag{171}$$

$$p = p_i^{\text{vdw1}} + \left(\frac{p_i^{\text{asym}}}{p_i^{\text{sym}} + p_i^{\text{asym}}}\right) p_i^{\text{vdw2}} \tag{172}$$

for symmetric and asymmetric cases, respectively.

The result of such analysis is presented in Figure 26. Interestingly, in the singly substituted case the red curve, that corresponds to the contribution of asymmetric ozone molecules, lays notable higher, compared to the symmetric one. In the doubly substituted case this is not observed. The effect of this peculiar result on the kinetics and on the

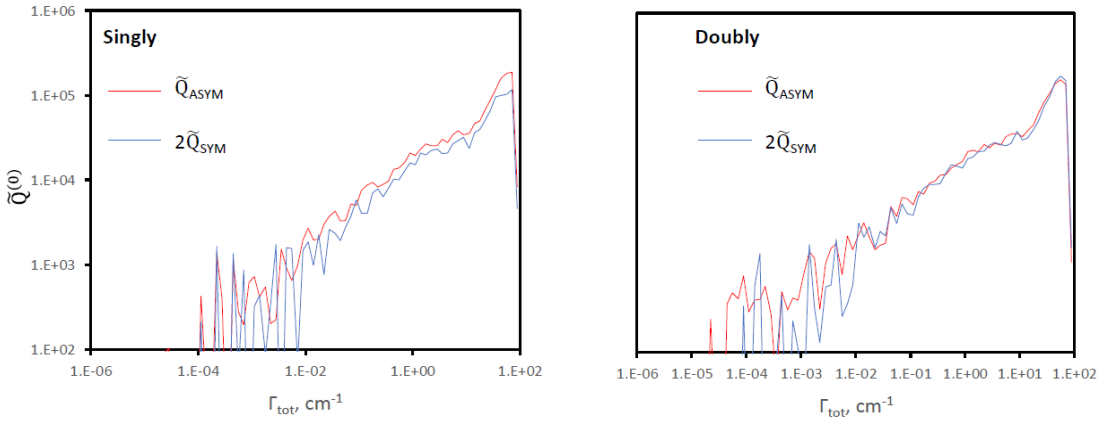

Figure 26. Distribution of resonance widths for the van der Waals states in asymmetric (red) and symmetric (blue) ozone molecules. Left and right frames correspond to single and double isotopic substitutions. To simplify the comparison, we plotted Q_{asym} and $2Q_{\text{sym}}$ in order to offset the effect of symmetry. In this analysis, van der Waals probability in Channel 2 was split between symmetric and asymmetric isotopologues according to Equations 171 and 172.

isotope effect still needs to be determined during the future work. Average values of

resonance widths computed in this this way are included to the Table 14. Those numbers are very similar which, again, means that we do not see any substantial difference between widths of resonances in symmetric and asymmetric ozone molecules.

V-5. Summary

In this chapter we started a detailed study of resonance properties, with the focus on differences between symmetric and asymmetric ozone molecules. It appears that resonance widths depend on the kind of a resonance. We identified three types of resonances that corresponds to the vibrational states with wavefunctions localized in the covalent well of ozone (behind the transition state), those delocalized over the van der Waals plateau (outside of the transition state) and the continuum states (in the asymptotic region of the PES). In the future, the effect of these van der Waals states on the temperature dependence of pathway-specific rates of the ozone forming reaction, and on the isotope effects will be studied.

CHAPTER VI. THE MODEL OF STABILIZATION AND APPLICATION TO KINETIC THEORY

In famous paper of Mauersberger's et al.[27] in Science (1999), it was stated that "It is not the symmetry of a molecule that determines the magnitude of the enrichment, but rather it is the nature of the collision process that occurs when ozone is produced in a nitrogen-oxygen gas mixture". Mauersberger stated that the clue to the ozone isotope problem is in the stabilization step. Since the most important of my goals in this work as listed in Chapter IV was the testing of a more sophisticated model for stabilization. In order to achieve this, the process of collision of metastable states must be rethought. Previously, stabilization process was described by Equation 41. The single value of k^{stab} was proportional to the constant value of σ_{stab} and collision velocity. In a literature there is lack of sufficient stabilization model that explains the mysterious isotope effect in ozone. In this chapter, the attempt to propose a sufficient model for the stabilization step will be taken and the rest of ideas for improvement of the ozone theory is left for the future generations of researchers.

VI-1. Exponential Model of Stabilization

Here we test the exponential stabilization model. Initially we postulated that the stabilization rate coefficient $k_i^{\mathrm{stab}} = \sigma \upsilon p_i^{\mathrm{tot}}$ is directionally proportional to the collision velocity $\upsilon = \sqrt{8kT/\pi\mu}$ and $\sigma_{\mathrm{stab}} = 154.03\ a_0^2$.[21] The outcome of such a simple stabilization model is illustrated in Chapter IV, particularly in Figure 17, with which the theoretical prediction is in comparable range with experimental dependence.

For better visualization of Figure 17, in Figure 27 we added an error bar from the paper of Janssen[10] and complemented by the η-effect calculated with an exponential

model (red line, which will be discussed further). The difference between the experiment and the simple stabilization model (green line) stays within the error bars, but the discrepancy in magnitude increases as temperature is raised. With introduction of exponential factor $k_i^{\text{stab}} = \sigma \upsilon p_i^{\text{tot}} e^{-\frac{E_i}{\Delta E}}$ in the stabilization step the theoretical curve was improved (red curve in Figure 27).

The temperature dependence of the η-effect in Figure 17 as the main achievement of the previous theory, summarized in Chapter IV, was recalculated in this chapter using the database provided by Igor Gayday (unpublished).

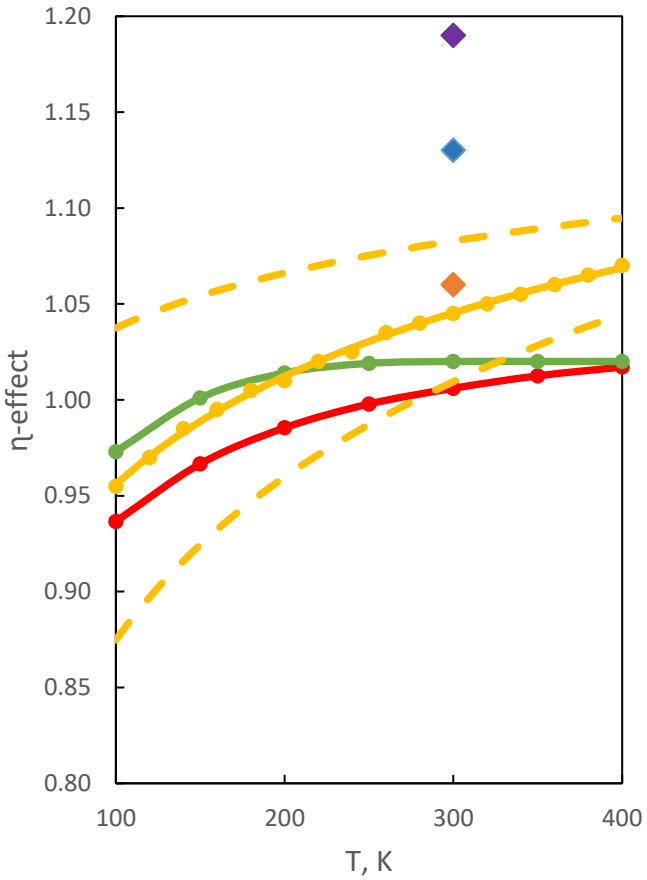

Figure 27. Theoretical (green, red) and experimental (yellow) temperature dependencies of the η-effect for molecule $^{668}O_3/^{686}O_3$.[43] The orange diamond the η-effect reported in a paper of Janssen[10], the blue diamond was reported earlier[35]; the violet diamond corresponded to doubly substituted case.[10]

It is necessary to clarify the changes that Igor Gayday brought to the new database:

1. The new data base was supplemented with states for all J and K up to J = 32, then after that were calculated with increments of $\Delta J = 4$ and $\Delta K = 2$ up to J = 64. A half-integer basis has been added to account for symmetry of rotational wavefunctions; this amendment will be used for calculation but won't be discussed in this chapter.
2. The important innovation is subdivision onto the covalent and van der Waals probabilities (see Chapter V) between symmetric and asymmetric components, so that the models proposed in the Chapter V are no longer required. This does not belittle the importance of discussing the properties of resonances, notedly the conclusion is that van der Waals resonances play an important role in recombination.
3. The new database contains calculations not only for the singly and doubly substituted ozone with ^{18}O, but also for the molecule with the substituted isotope ^{17}O, as well as the calculation for the unsubstituted ozone molecule $^{16}O^{16}O^{16}O$. It is especially important in the context of Chapter IV, where instead of a direct comparison with the dependences for the k_{666}, we had to take pathway S, assuming that they are experimentally close.

In the context of all this, the reader can notice that the green line in Figure 27 differs from Figure 17, but not by much. The changes made to the database do not remove the flat dependence at high temperatures, while the exponential factor corrects it

well. For this theoretical prediction (red line, Figure 27) the ΔE = 43.13 cm^{-1} was taken from a paper of Schinke[15] for temperature of 298 K.

The theory, using with which the red line was calculated was also finalized. Starting with ΔE in Equation 60-61 with energy difference, ΔZPE, and in an agreement with our formalism for asymmetric and symmetric rates we now obtain:

$$R_{\mathrm{sym}} = [\mathrm{M}][68][6]\frac{k^{\mathrm{stab}}}{Q_{\mathrm{ch2}}}\sum_i (2J+1)p_i^{\mathrm{sym}} w_i \frac{\Gamma_i^{\mathrm{ch2}}}{\Gamma_i^{\mathrm{tot}}} e^{-\frac{E_i}{kT}} e^{-\frac{E_i}{\Delta E}} + [\mathrm{M}][66][8]\frac{k^{\mathrm{stab}}}{Q_{\mathrm{ch1}}}\sum_i (2J+1)p_i^{\mathrm{sym}} w_i \frac{\Gamma_i^{\mathrm{ch1}}}{\Gamma_i^{\mathrm{tot}}} e^{-\frac{E_i-\Delta\mathrm{ZPE}}{kT}} e^{-\frac{E_i-\Delta\mathrm{ZPE}}{\Delta E}} \quad (173)$$

$$R_{\mathrm{asym}} = [\mathrm{M}][68][6]\frac{k^{\mathrm{stab}}}{Q_{\mathrm{ch2}}}\sum_i (2J+1)p_i^{\mathrm{asym}} w_i \frac{\Gamma_i^{\mathrm{ch2}}}{\Gamma_i^{\mathrm{tot}}} e^{-\frac{E_i}{kT}} e^{-\frac{E_i}{\Delta E}} + [\mathrm{M}][66][8]\frac{k^{\mathrm{stab}}}{Q_{\mathrm{ch1}}}\sum_i (2J+1)p_i^{\mathrm{asym}} w_i \frac{\Gamma_i^{\mathrm{ch1}}}{\Gamma_i^{\mathrm{tot}}} e^{-\frac{E_i-\Delta\mathrm{ZPE}}{kT}} e^{-\frac{E_i-\Delta\mathrm{ZPE}}{\Delta E}} \quad (174)$$

Where k_i^{stab} is initially expressed through the constant cross-section and velocity; it's constant part k^{stab} stays outside the summation while the exponential factor is added to the summation and it is present in w_i. Respectively to Equation 62, the dynamic weight w_i contains k_i^{stab}, for both symmetric and asymmetric cases the dynamic weight with embedded exponential factor:

$$w^i = \frac{\Gamma_i/\hbar}{\Gamma_i/\hbar + k^{\mathrm{stab}} p_i^{\mathrm{tot}}\left[\frac{\Gamma_i^{\mathrm{ch1}}}{\Gamma_i^{\mathrm{tot}}} e^{-\frac{E_i-\Delta\mathrm{ZPE}}{\Delta E}} + \frac{\Gamma_i^{\mathrm{ch2}}}{\Gamma_i^{\mathrm{tot}}} e^{-\frac{E_i}{\Delta E}}\right][\mathrm{M}]} \quad (175)$$

Notice that the exponential factor analytically cancels in η-effect (because it is the ratio of R_{asym} and R_{sym}) except in the dynamic weight (see the Equation 175). This dynamic weight creates a well visible effect on the ratio of asymmetric and symmetric

(see the red curve in Figure 27). Recall that R_{asym} and R_{sym} contributes from two reaction channels but both relate to the lowest. The ratio of Equations 173 and 174 defines the η-effect:

$$\eta = \frac{R_{\text{asym}}}{2R_{\text{sym}}} = \frac{\kappa_{\text{asym}}}{2\kappa_{\text{sym}}} \tag{176}$$

In Figure 27, there is still a discrepancy with experimental dependence in the high temperature region, but slope is significantly improved.

Of course, η-effect is not the only, although very important, experimental result on which the influence of the exponential model can be tested. There are also temperature and pressure dependences for the k_{666}, which can now be calculated directly since the new database is available. In the literature, data are available for the δ-effect (which relates to unsubstituted molecule) and its dependence on pressure and temperature. The study of this model is in the next section, it gives a positive result but cannot completely describe all the isotope effects. However, useful insights from these tests were obtained and applied further.

VI-2. Testing the Exponential Model

We start with varying the magnitude of ΔE. ΔE is the energy that resonance loses during collision with the bath gas. The higher the ΔE the more likely resonance will be stabilized. For simplicity it is convenient to directly compare the experimental dependence of non-substitute $^{16}O^{16}O^{16}O$ with the theoretical model. Recall that the total rate of ozone formation is given by Equation 121 as:

$$R_{666} = k_{666}[\mathrm{M}][\mathrm{O}][\mathrm{OO}] = \sum_i k_i^{stab}[\mathrm{M}][\mathrm{O}_3^*]_i \tag{177}$$

From which the recombination rate coefficient for non-substituted $^{16}O^{16}O^{16}O$:

$$k_{666} = \frac{1}{[O][OO]} \sum_i k_i^{stab} [O_3^*]_i \tag{178}$$

With steady state approximation and analogously to the Equations 173-174 the k_{666} contains the exponential factor:

$$k_{666} = \frac{k^{\text{stab}}}{Q_{\text{ch}}} \sum_i (2J+1) p_i^{\text{tot}} w_i e^{-\frac{E_i}{kT}} e^{-\frac{E_i}{\Delta E}} \tag{179}$$

Where the dynamic weight with exponential factor compared to Equation 175 is simply:

$$w^i = \frac{\Gamma_i/\hbar}{\Gamma_i/\hbar + k^{\text{stab}} p_i^{\text{tot}} e^{-\frac{E_i}{\Delta E}} [\text{M}]} \tag{180}$$

And, of course, the $k_i^{\text{stab}} = k^{\text{stab}} p_i^{\text{tot}} e^{-\frac{E_i}{\Delta E}}$. As in Chapter II the formation rate coefficient is expressed through the Equllibrium constant $K_{\text{eq}} = \frac{(2J+1)e^{-\frac{E_i}{kT}}}{Q_{\text{ch}}}$ (see Equations 55-56). Finally the recombination rate coefficient for unsubstituted molecule which was used by me for computing with the summation across all states is:

$$k_{666} = \sum_i w^i K_{\text{eq}} \, k_i^{\text{stab}} \tag{181}$$

In the literature there is data[10,16,23,46] with the pressure dependence behavior of rate coefficient k_{666}. Particularly in the beginning of this document the pressure dependence is taken from a paper of Troe[16] in Figure 1.

Here in the Figure 28, the experimental points taken from follow Figure 1 he 2nd order kinetics at low pressure and 3d order kinetics at the high pressure, but the shape of the curve shows the same small curvature in high pressure limit as in Figure 1. The ΔE = 200 cm^{-1} qualitatively repeated the experimental behavior, however, at the lower pressure so called plateau (2nd order rate coefficient) is not described by the theoretical curve. It requires more detailed analysis (see next section).

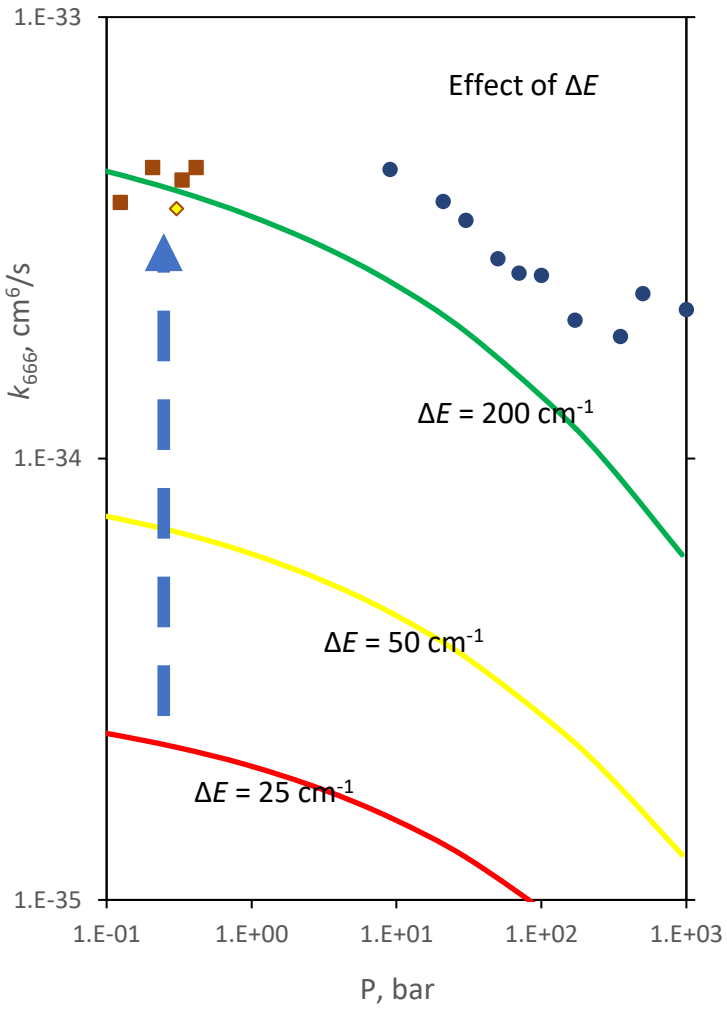

Figure 28. The pressure dependence of non-substituted ozone rate coefficient in comparison with experimental data[10,16,23]; with bath gas was taken as Ar. Red and yellow and green lines show the theoretical prediction with ΔE = 25, ΔE = 50 and 200 cm^{-1} accordingly. The measurements are in consistency with theoretical prediction with ΔE = 200 cm^{-1}.

Peculiar effects were also seen with changing the P-model (see Figure 29a) and varying the cross section (see Figure 29b). P-model basically defines the formula for the p_i^{tot} term, for example, in Equation 180; in this expression van der Waals probability is included (see Figure 29a).

A change in σ_{stab} gives a parallel shift of the pressure curve. Its effect on the denominator in the weight expression is not as significant as on the numerator in k_i^{stab}. The changing in slope is observed in Figure 29a in the yellow curve where the van der Waals is included in the formula - $p_{\mathrm{cov}} + p_{\mathrm{vdw}}$; in the green curve with van der Waals and the square root - $\sqrt{p_{\mathrm{cov}} + p_{\mathrm{vdw}}}$; and the blue curve - $\sqrt[5]{p_{\mathrm{cov}} + p_{\mathrm{vdw}}}$. We observe a

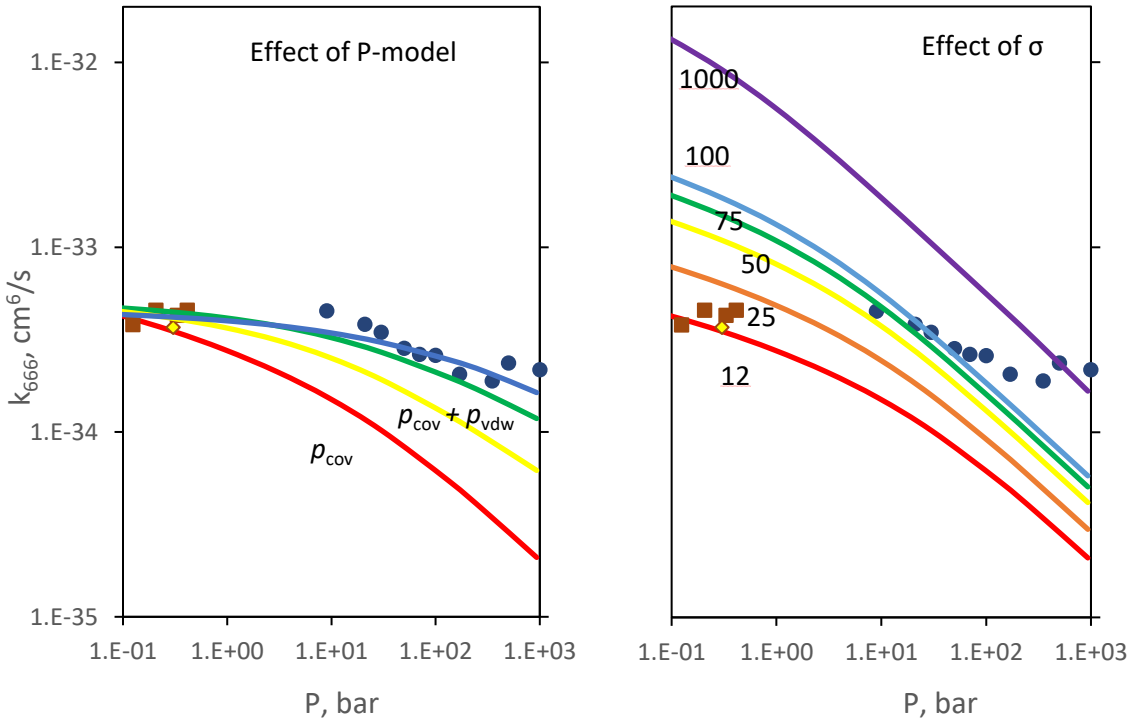

Figure 29. The temperature dependence of non-substituted ozone rate coefficient in comparison with experiment.[10,16,23] Left picture corresponds to varying the P-model: 1) red curve corresponds to P-model with single covalent probability p_{cov} which multiplied by cross section in k^{stab}; 2) yellow curve corresponds to p_{cov}+p_{vdw}; 3) green curve - $\sqrt{p_{\mathrm{cov}} + p_{\mathrm{vdw}}}$; 4) the blue curve - $\sqrt[5]{p_{\mathrm{cov}} + p_{\mathrm{vdw}}}$. Right picture corresponds to the σ_{stab} varied from red to violet as 12, 25, 50, 75, 100 and 1000 a_0^2.

different plateau at low pressures or a different fall off on the right. For obvious reasons, the root of some degrees slows down the fall off of the curve. Probability is included in the numerator; it is always less than 1 and the root increases its contribution artificially. Further, it was found that the introduction of the root causes the undesirable factors to the contribution of states to recombination, which are not clear how to estimate, therefore it is recommended to abandon the model with a root. In this work, these factors will not be explained in detail, it is only recommended to continue with including the van der Waals probability.

Just as the ΔE has defined the behavior of the pressure dependence, the absolute value of it at 300 K, the plateau at the lower pressure limit can be adjusted by varying the value of the cross-section σ. The cross section of the stabilization is a parameter in this model and has been adjusted to fit the experiment. The temperature dependence of the recombination rate coefficient is not as sensitive to ΔE in terms of the slope. In general, to describe the temperature behavior of the rate it is enough to adjust the cross-section of stabilization (Figure 30a, Figure 30b). In the Introduction in Figure 2 the temperature dependence was fitted by Troe[19], he fits it with two trend lines - the blue fitting line accounts for the Chaperon radical complex mechanism and red – for the Lindeman energy transfer mechanism. Here on Figure 30c by varying a ΔE we observe the increasing of magnitude of the rate and the slope is in a good agreement with the experiment. In Figure 30a and Figure 30b, Lindeman dotted line and red solid line (sum of both mechanisms which describes experimental points from Figure 2) fit by theoretical curves. The temperature dependence of ΔE is theoretically possible and in the paper of Schinke[15] ΔE grows as a function of temperature.

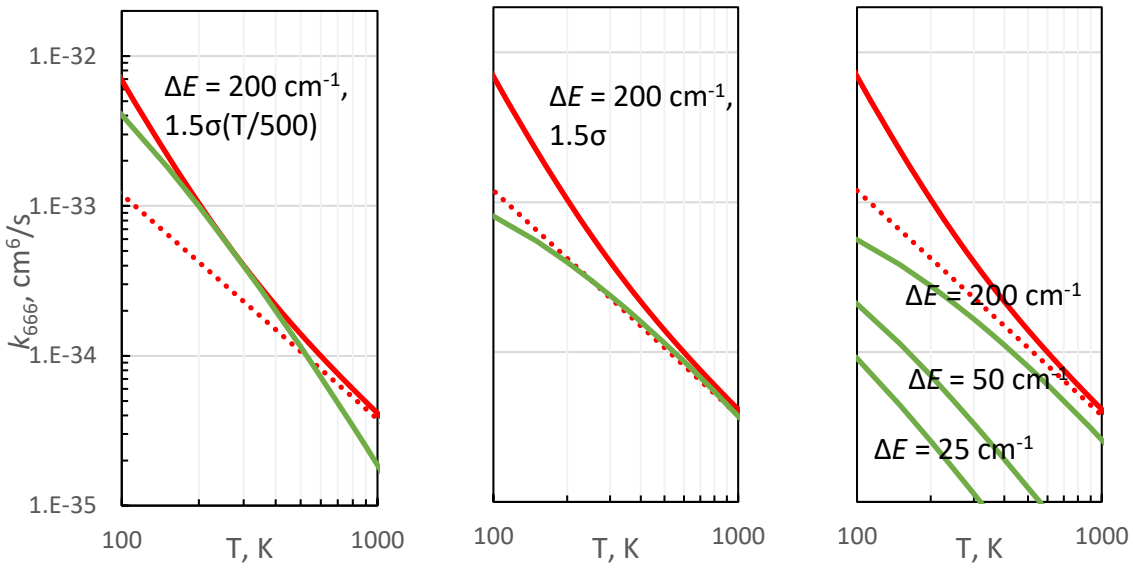

Figure 30. The temperature dependence of non-substituted ozone rate coefficient in comparison with experimental data of Troe. Red and blue dotted lines correspond to $k_{rec}^{RC} = 1.7 \times 10^{34}$ (T/300)$^{-3.2}$ cm^6 mol^{-2} s^{-1} and $k_{rec}^{ET} = 2.3 \times 10^{34}$ (T/300)$^{-1.5}$ cm^6 mol^{-2} s^{-1} fitting equations. The red solid line corresponds to the sum of RC and ET mechanisms. The green line corresponds to theoretical predictions – a) theoretical curve with cross-section with T-dependent σ(T/500), Δ*E* = 200 cm^{-1}; b) theoretical curve with good fit of Lindeman k_{rec}^{ET}, temperature independent σ = 1.5σ$_0$ (σ$_0$ =154.03 a$_0^2$, recommended for ozone), c) varied Δ*E* with constant σ$_0$.

Unfortunately, the implementation of Δ*E* depending on temperature from the paper[15] does not provide a desirable temperature dependence of k_{666}, controversially to gain the decreasing curve in a raising temperature the dependence of Δ*E* is supposed to be the opposite (see Table 16). The good fit of both Lindeman curve and the red solid line (sum of both mechanisms) are given on Figure 31. The last point at the temperature of 100 K

Table 16. The temperature dependence of the ΔE based on the fitting results of experimental temperature dependence. ΔE from second column was used for blue theoretical curve; ΔE from third column used for green theoretical curve on Figure 31.

T(K)	ΔE, fitting $k_{rec}^{ET} + k_{rec}^{RC}$	ΔE, fitting k_{rec}^{ET}
100	1000	90
150	200	35
200	66	23
250	35	18
300	25	14
350	20	12.5
400	17	11
700	10	8,5
1000	9	7.7

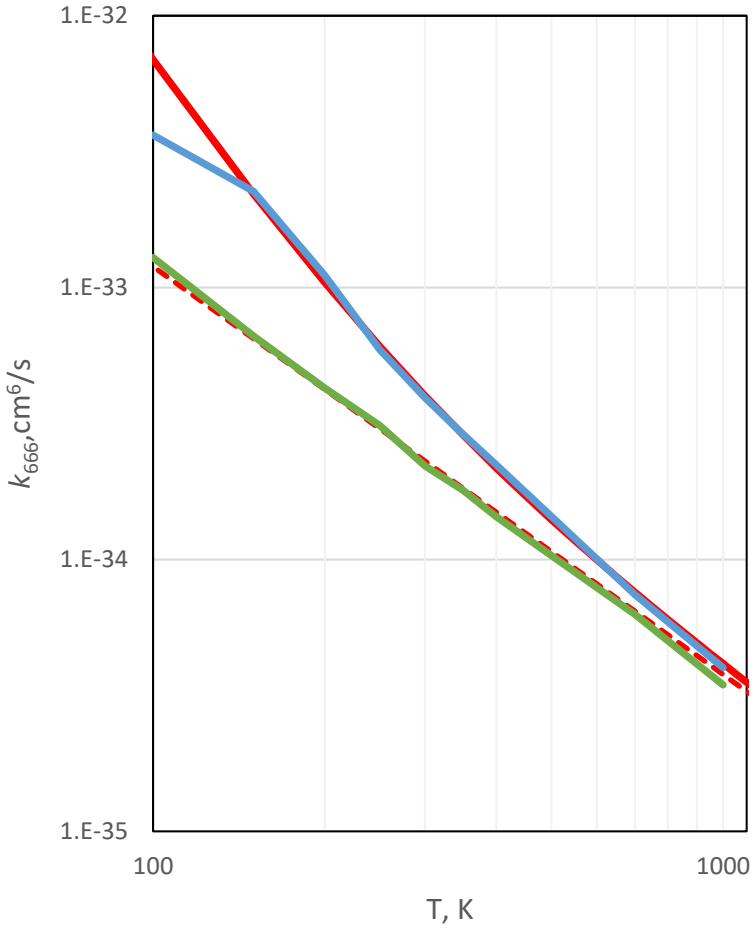

Figure 31. The temperature dependence of non-substituted ozone rate coefficient in comparison with experimental data of Troe[19]. Green line corresponds to theoretical prediction of k_{rec}^{ET}. Blue line corresponds to theoretical prediction of $k_{rec}^{ET} + k_{rec}^{RC}$.

stands out from the rest because the spectrum of states is cut after 1000 cm^{-1} and at such a low temperature ΔE of 1000 cm^{-1} no longer plays a role, there are simply no states. It would be optimistic to describe with theoretical prediction the sum of both mechanisms (red solid on Figure 31), but to be realistic in our theory the Chaperon mechanism is not included and it is too ambitious to expect that this curve will be described by this theory, however, the fact that the lower curve is completely described is already a good result.

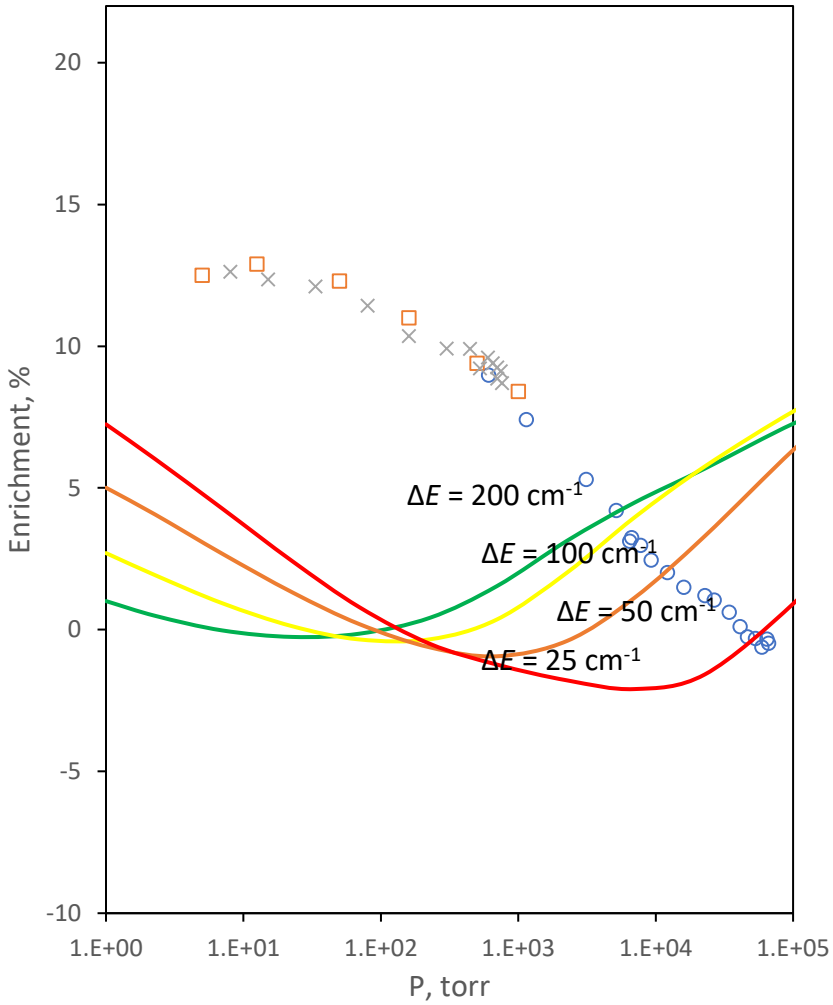

Figure 32. The pressure dependence of delta-effect predicted for the ΔE from 25, 50, 100 to 200 cm^{-1} (red, orange, yellow, green accordingly) compared to experimental data. The theoretical prediction involved exponential model discussed in the Appendix.

Finally, the exponential model was applied to the description of η, δ-effects. In the first section we already tried the exponential model for η-effects (see Figure 27), but we don't know how η-effect behaves with increasing pressure. We know only that δ-effect drops to zero around 100 bar. By employing the exponential model with different ΔE the dependence in Figure 32 behaves exactly opposite. It bends the other way and in general grows with increasing pressure. Notice also that the absolute values are an order of magnitude smaller. If we choose among gained results, the red curve shows slight tendency to fall, but at the end it bends in the wrong direction.

Summing up the exponential model taught us how to handle temperature dependence but failed with pressure dependence. The main insight is that the temperature dependence of k_{rec} is easy to describe. To be consistent for description of the isotope effect and its pressure dependences the optimal parameter of ΔE needs to be taken as 25 cm^{-1} with appropriate cross-sections. The P-model should contain the covalent and van der Waals probabilities.

VI-3. The Exponential Model with Transitions between the States

Many attempts to describe the isotope effect, and particularly this attempt, have been undertaken by varying the value of ΔE, introducing the temperature dependence in stabilization (see previous sections), varying the P-model. Most of these attempts decreased the magnitude of η-effect and failed to describe the experimental pressure dependence.

In the paper of R. Forrey[47], the model with a promising outcome for pressure dependence was developed for reaction of H_2. The idea of taking in account repopulation of the metastable and bound states is the basis of his iteration approach. To understand the mechanism of repopulation it can be useful to look at the Figure 33. In the Figure 33, the reaction of ozone formation according to the Lindeman mechanism goes through the formation of resonance states O_3^*. After the collision with a bath gas M, it transfers the energy and stabilizes into O_3 (bound state). Here with green arrows, we represent the stabilization process that was described in Chapter I with difference in how one resonance state stabilizes in all available bound states (not in the one single ground state as in Chapter I). Then we add the repopulation of the metastable state by other resonances (red and pink arrows), and then dissociation from given state to all others (violet arrows).

All these transitions should first be reflected in the master equation. To take in account the repopulation of the state the master Equation 52 must be rewritten:

$$0 = \frac{d[O_3^*]_i}{dt} = k_i^{\text{form}}[OO][O] - k_i^{\text{dec}}[O_3^*]_i - k_i^{\text{stab}}[M][O_3^*]_i - k_i^{\text{diss}}[M][O_3^*]_i \quad (182)$$

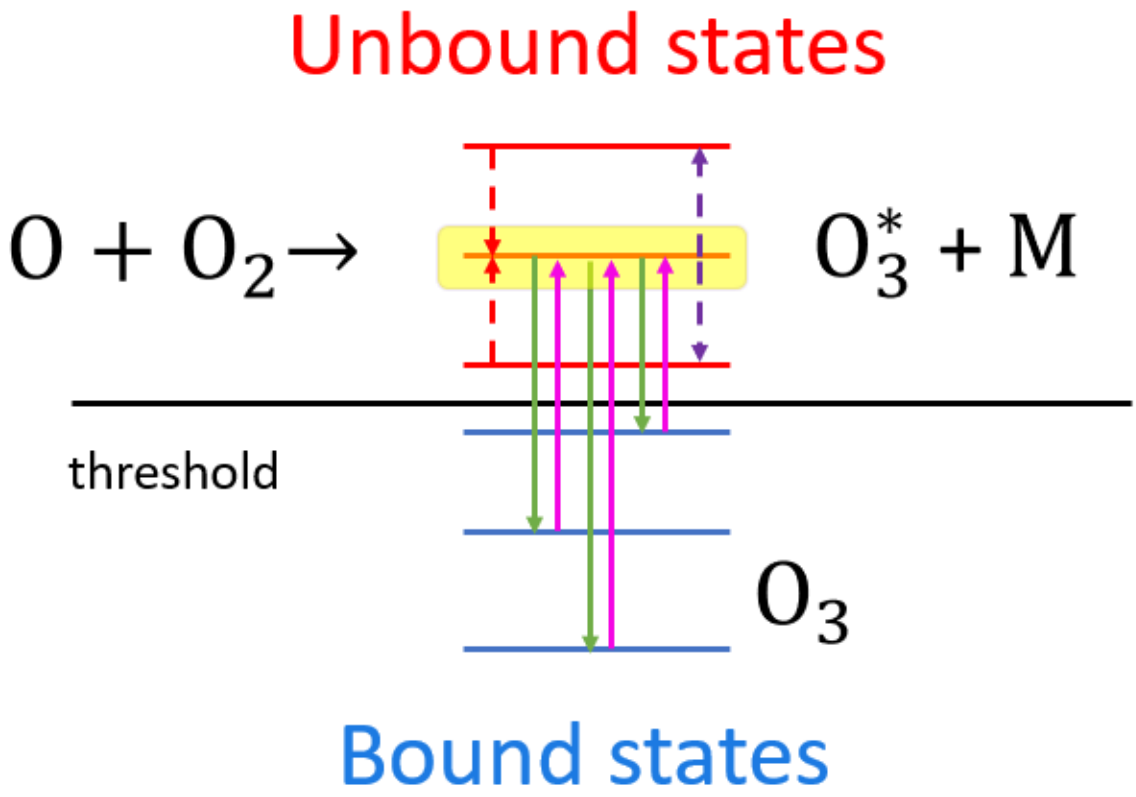

Figure 33. The schematic picture of ozone formation through the metastable ozone states. The green arrows accounts for the stabilization to the all ground states from active resonance; the pink arrows describe the opposite process of repopulation of the resonance from bound. The red and violet arrows show the repopulation and dissosiation to other resonances accordingly.

By assuming a steady-state approximation and for the sake of simplicity for the formation of unsubstituted ozone $^{16}O^{16}O^{16}O$, we obtain:

$$[O_3^*]_i = \frac{k_i^{\text{form}}[OO][O]}{k_i^{\text{dec}} + (k_i^{\text{stab}} + k_i^{\text{diss}})[M]} \quad (183)$$

The cornerstone of this method lies in how the transitions between the states are calculated. Particularly the k_i^{stab} and k_i^{diss} are not the arbitrary constants anymore but the sums of all other transitions between *i* (initial) and *j* (final) states. State *j* can be another

neighboring resonance state or bound state. Physically such a transition must be allowed. Stabilization to the state with closer energy should occur more easily than for two states distant from each other. The exponential factor copes well with this distribution. The probability factor (P-model - see Equation 184) in the iteration model can be expressed in different ways. For resonance states that are delocalized between two symmetric and asymmetric wells, this factor determines the probability of the cross-term transitions between wells. If cross-terms are not included in the factor, such transitions are prohibited. Van der Waals probability discussed in the Chapter V can be either included in the model or not (it also prohibits the cross-term transitions between van der Walls wells). In the case when van der Waals terms are included we obtain transition elements:

$$\kappa^i_{\text{tran}} = \kappa_{i\to j} = \left(\sqrt{p^i_{\text{cov}} p^j_{\text{cov}}} + \sqrt{p^i_{\text{vdw}} p^j_{\text{vdw}}}\right) \exp\left(-\frac{\left|E^i - E^j\right|}{\Delta E}\right) \tag{184}$$

$$\text{where } \Delta E = \begin{cases} \Delta E_{\text{up}}, \text{if } j > i \\ \Delta E_{\text{down}}, \text{if } j < i \end{cases}$$

ΔE_{up} is for the transition to the state j with higher energy and ΔE_{down} is for transition to the state with lower energy. According to macroscopic reversibility principle:

$$\frac{1}{\Delta E_{\text{up}}} - \frac{1}{\Delta E_{\text{down}}} = \frac{1}{kT} \tag{185}$$

The relationship between ΔE_{up} and ΔE_{down} depends on temperature. Taken from the paper of Schinke[15] the ΔE_{up} and ΔE_{down} is presented in the Figure 34 (orange line). In

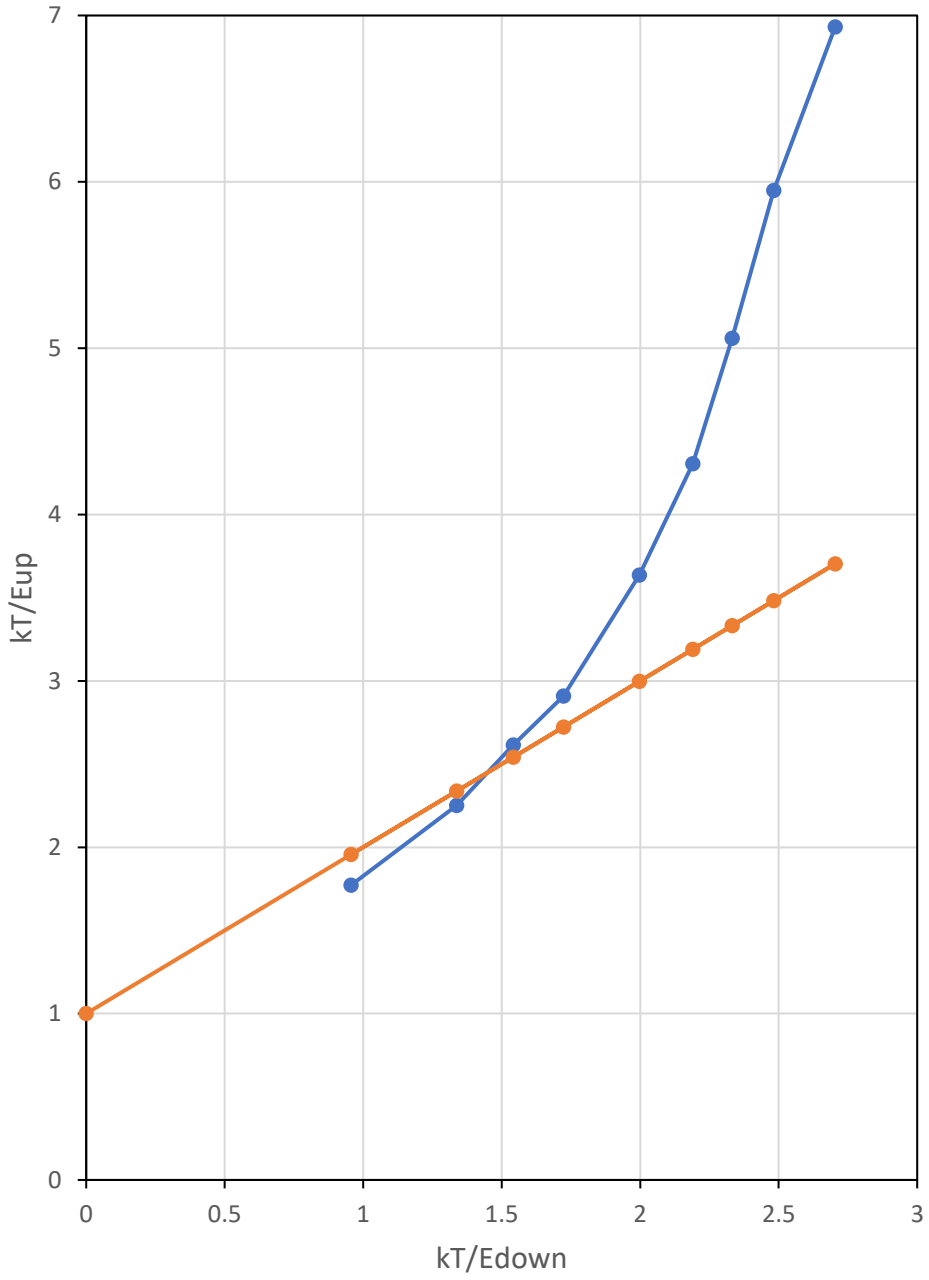

Figure 34. Macroscopic reversibility principle compared to the theoretical prediction of Schinke[15]. Nine blue points connected with a line correspond to the table temperature range from 100 to 2500 K. Orange line corresponds to Equation 185 with $\Delta E\downarrow$ taken from Table 16.

Figure 34 ratios $\frac{kT}{\Delta E_{\mathrm{up}}}$ vs. $\frac{kT}{\Delta E_{\mathrm{down}}}$ gives a linear function, and Schinke's points (blue) are in

Table 17. The temperature dependence of the ΔE based on the data of Schinke.[18] In first colomn with ΔE contains the vibrational ΔE which was used for exponential model. $\Delta E\downarrow$ and $\Delta E\uparrow$ are depicted in the Figure 34.

	ΔE	$\Delta E\downarrow$	$\Delta E\uparrow$
100	20.13	72.69	39.22
200	29.02	103.9	61.76
298	43.13	134.33	79.24
400	60.54	161.38	95.57
700	122.52	243.57	133.81
1000	184.11	317.31	161.4
1500	295.39	47.13	206.08
2000	397.48	559.92	233.69
2500	474.36	642.62	250.68

a good agreement up to 400 K. The experimental data for temperature dependence of ΔE_{up} and ΔE_{down} is given in a Table 17.

Returning to the master equation for the unsubstituted molecule, the steady-state approximation provides the expression for $[\mathrm{O}_3^*]_i$ in Equation 183; originally substituted to the definition expression of total rate of the recombination in Equation 178 and provides the expression for rate coefficient $k_{666} = \sum_i w^i K_{\mathrm{eq}}\, k_i^{\mathrm{stab}}$. The dynamic weight w^i, with the additional process we have discussed at the beginig of this section, has trasformed to:

$$w^i = \frac{\Gamma_i/\hbar}{\Gamma_i/\hbar + (k_i^{\mathrm{stab}} + k_i^{\mathrm{diss}})[\mathrm{M}]} \tag{186}$$

Where the sum of $k_i^{\text{stab}} + k_i^{\text{diss}} = k_0 \kappa_{\text{tran}}^i$; κ_{tran}^i is the sum of all possible transitions from state *i* to all states *j*. The coefficient k_0 remains constant, $k_0 = v * \sigma_{\text{tran}}$ and σ_{tran} is the fitting parameter. According to Equation 178, the recombination rate coefficient is determined by three components – dynamic weight, equilibrium constant and stabilization rate coefficient. In Equation 186 the only one entity which depends on pressure is dynamic weight.

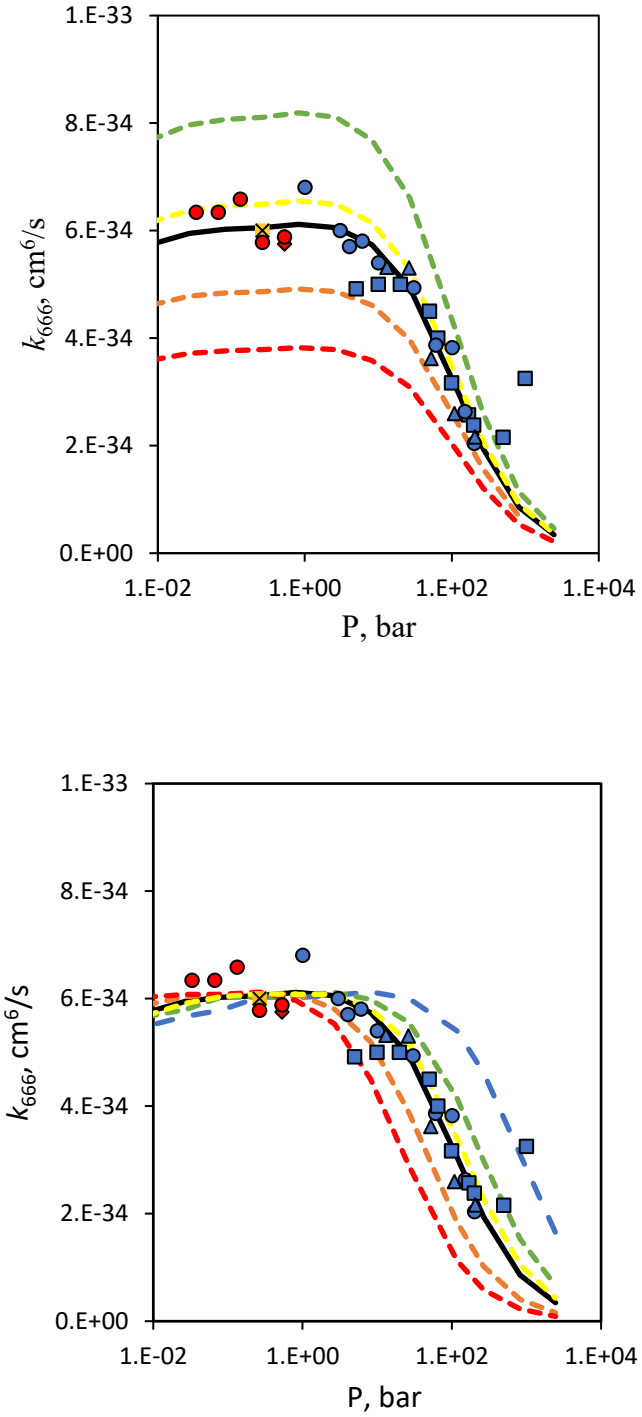

Figure 35. The effect of varying the σ_{stab} and σ_{tran}. On 35a (upper picture) σ_{stab} varies from 0.7 (red) to 1.5 a_0^2 (green) On picture 35b (lower picture) the σ_{tran} was varied from 0.9 a_0^2 (blue) to 32 a_0^2 (red). Red circles and diamond correspond to results of Lin and Leu[23] , the orange diamond of Maursberger[10], blue square, triangles and circles are from Troe.[16,46]

Stabilization rate coefficient also accounts for the transitions from *i* to *j*, but the states *i* are strictly defined as resonances and the states *j* as bound states; for such a transition we use Equation 184 with only ΔE_{down}:

$$\kappa_{i\to j} = \left(\sqrt{p^i_{\text{cov}} p^j_{\text{cov}}} + \sqrt{p^i_{\text{vdw}} p^j_{\text{vdw}}}\right) \exp\left(-\frac{\left|E^i - E^j\right|}{\Delta E_{\text{down}}}\right), E^i > E^j \qquad (187)$$

Then $k^i_{\text{stab}} = k_0 \kappa_{i\to j} = v\sigma_{\text{stab}}\kappa_{i\to j}$.

In general, σ_{stab} and σ_{tran} are fitting parameters and can be defined from comparison with experimental data. As the experimental data we take the pressure dependence of unsubstituted ozone $^{16}O^{16}O^{16}O$. The experimental results of three groups of Maursberger[10], Lin and Leu[23], and Troe[16,46] are in Figure 35 including the pressure dependence of the second order rate coefficient k_{666} at the lower pressure limit and third order rate coefficient in a high-pressure limit in respect to O, O_2 and M.

VI-4. Numerical Results with New Stabilization Model.

In general, the values of cross sections σ_{stab} and σ_{tran} are arbitrary, however, the significant difference between them can't be explained in terms of general physical stand points. To demonstrate the effect of both cross sections on pressure dependence of k_{666} the values of σ_{stab} and σ_{tran} were varied to fit the experimental points and represented in Figure 36a and in Figure 36b accordingly. Stabilization cross section σ_{stab} is a coefficient that defines the magnitude of k_{666} and does not affect the shape of the curve. However, transition cross section σ_{tran} defines the pressure dependence curve's fall off, since the pressure multiplied by this factor in the denominator competes with the resonance width.

The black curve from both pictures described the experimental pressure dependence accurately with σ_{stab} = 1.12 a_0^2 and σ_{tran} = 6.5 $a_{0,}^2$ both parameters have the same order of magnitude.

The pressure dependence taken from Figure 35 with best set of parameters σ_{stab} = 1.12 a_0^2 and σ_{tran} = 6.5 a_0^2 and the temperature dependence of Troe and all in Figure 36 are in comparable range with experiment. The experimental "tail" in Figure 36a at high pressure must be described by the process of three body collision, and with this theory we do not even hope to describe it, because we do not consider such terms. It is very fortunate that we have described most of the pressure and temperature dependence of k_{666}; however, the temperature and pressure dependences of isotope effects cannot be simply adjusted by changing a cross-section value. As it was mentioned above the [M] pressure of the bath gas is multiplied by the σ_{tran} competes with a resonance width Γ (see Equation 186). In the lower pressure limit the second term with [M] might be neglected so the pressure dependence becomes flat. In Figure 36b we tried to control the fall off through varying the value of σ_{tran}, but in the low pressure limit the lifetime of the resonance determines the behavior.

Therefore, we introduce new Γ-criteria which will differentiate the bound state from resonance state based on the value of their widths. We would transfer the resonance states to bound according to Γ-criteria and our theoretical curve would reach the plateau and stop growing on the left. Otherwise, there would always be some resonance state at a given pressure that would be with such a small Γ that pressure dependence would be observed. Basically, in Figure 35 and in Figure 36 this criterion was already used. The plateau in the left part of all pictures was obtained because of all resonances with Γ < 1

cm^{-1} were converted to the bound states. Why was the Γ-criteria taken as 1 cm^{-1}? Firstly, with that parameter, the curve becomes flat at the pressure, comparable with the experiment, then falls off with increasing pressure. We learned that the fall off can be corrected using σ_{tran}, so why not to take any other Γ as criterion? The observable fact is that by removing states from resonances by applying this criterion, we greatly reduce the number of states with significant prevalence of van der Waals. The Γ-criteria removes states from that part of the spectrum where there is a difference between a symmetric and asymmetric molecule. It potentially affects the η-effect, therefore, if some criterion for Γs must be applied it should be no more than 1 cm^{-1}. It can be less, but then the δ-effect cannot be described. After employing Γ_{cutoff} = 1 cm^{-1} to the temperature dependence of η-effect, it showed a good slope, comparable to experiment, but dropped by the absolute

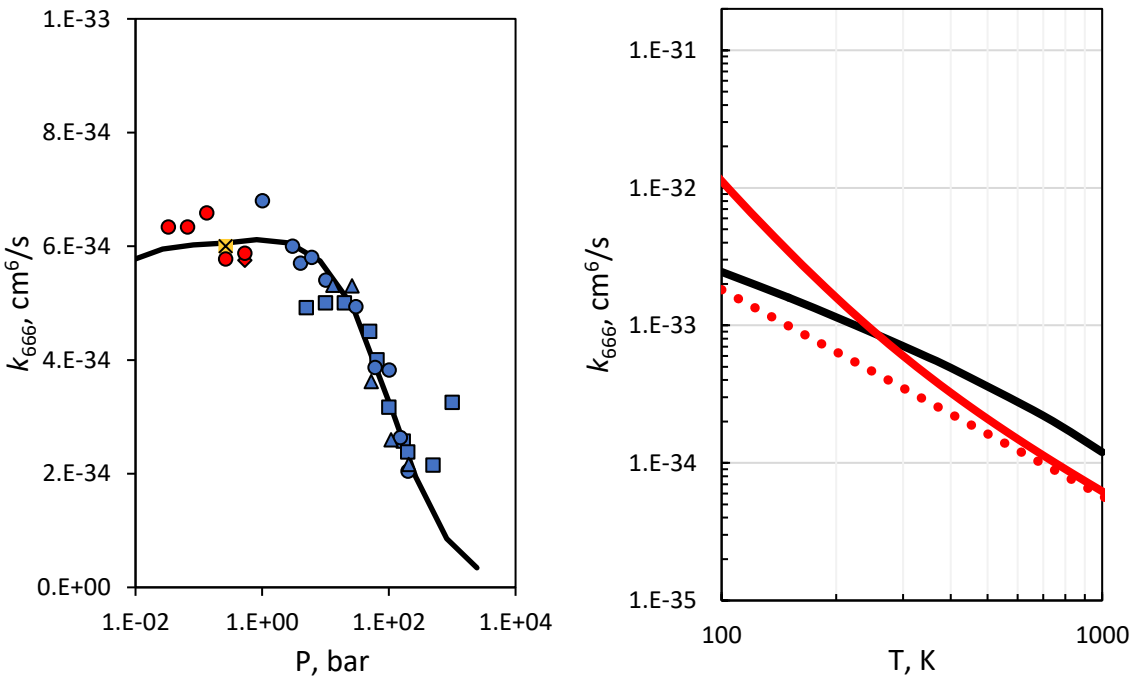

Figure 36. The effect of varying the σ_{stab} and σ_{tran}. On 32a (left picture) the pressure dependence with σ_{stab}= 1.12 a_0^2 and σ_{tran} = 6.5 a_0^2, on 32b (right picture) the temperature dependence with the same parameters. Bath gas – N_2/O_2 mixture.

value (black curve in Figure 37). Another adjustment is needed to describe both η-effect and δ-effect.

The p-model came to the rescue in this case. In Chapter V we have discussed the importance of the covalent and van der Waals probabilities and its distributions. The assumptions discussed in section 2 with exponents in the P-model caused the additional factors and became an outcast. The only one remaining knob to turn is whether or not to include the van der Waal in the P-model. It was noticed that at high pressures, the exclusion of van der Waals states led to an increase in dependence instead of a fall off after 1 bar. Being that the van der Waals probabilities are distributed differently in symmetric and asymmetric k_{sym} and k_{asym}, then if we cut some states with low total probability, we increase the difference in contribution of that van der Waals states, and

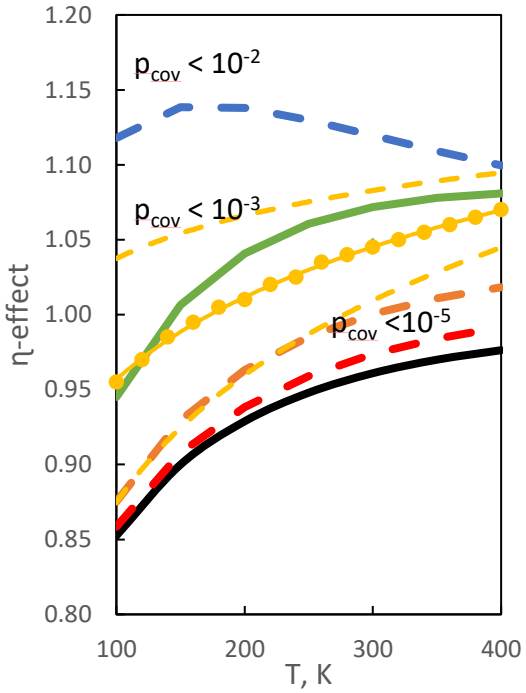

Figure 37. The effect of varying p-creteria with Γ-criteria = 1 cm^{-1}. A black curve corresponds to the theoretical prediction without cutoff by p-creteria, the red curve correspondes to $p_{\text{cutoff}} = 10^{-5}$, the orange - $p_{\text{cutoff}} = 10^{-4}$, the green - $p_{\text{cutoff}} = 10^{-3}$, the blue - $p_{\text{cutoff}} = 10^{-2}$.

this amplifies the value of the η-effect. Particularly in Figure 37 any cutoff which is higher than 0 amplified the η-effect. It seems as though the green curve from Figure 37 lies within the error bars and can be taken as an optimal criterion for the other dependences.

Finally, the last equation introduced in this work will be the expression for k_{tot}, which was implied in a Chapter II but for some reasons was not introduced directly:

$$k_{\text{tot}} = k_{\text{sym}} + k_{\text{asym}} \tag{188}$$

It directly follows from the Equations 50, 67-72, 81-82 but is not explicitly stated anywhere. Why does this equation become important? The data base now allows to calculate δ-effect directly, because it contains data for $^{16}O^{16}O^{16}O$. In the Equation 122 we showed that δ can be calculated through η if we assume that $k_{666} = 2k_{\text{sym}}$. This assumption is not needed because the source data for $^{16}O^{16}O^{16}O$ is available. Now we can use the original Equation 122 to calculate δ-effect:

$$\delta = \frac{2}{3}\left(\frac{R_{\text{asym}} + R_{\text{sym}}}{R_{666}}\right)\frac{[66]}{[68]} - 1 = \frac{2}{3}\left(\frac{\kappa_{\text{asym}} + \kappa_{\text{sym}}}{\kappa_{666}}\right) - 1 = \frac{2}{3}\frac{\kappa_{\text{tot}}}{\kappa_{666}} - 1 \tag{189}$$

The experimental data for δ-effect was measured involving singly-substituted ozone with isotopes ^{17}O and ^{18}O. The pressure dependences of δ-effect are shown in Figure 38. The pressure dependence of k_{666} shows fall off at 0.26 bar. By varying the value of the p_{cutoff} parameter, the experimental data can be fitted at the lower pressure limit, it shows no pressure dependence. The p_{cutoff} parameter implies that all states with p_{cov} (probability in covalent well) lower than this parameter are completely eliminated from the summation, compared to Γ-criteria which converts the state to bound but does not exclude its contribution. The plateau of δ-effect depends on the Γ-criteria, whereas

value of cutoff $p_{cutoff} = 10^{-3}$, 10^{-4} (orange or green curve) describes the tendency of the experimental pressure falloff with good accuracy.

While this pressure dependence is described accurately, unfortunately, the temperatures δ-effect became a stumbling block on the way to the finalization of this theory. Which, on the one hand, is good because it leaves room for reflection on the topic of improvement, but on the other hand, everything is squeezed out of this theory and there is no more leverage. For both singly-substituted molecules with ^{17}O and ^{18}O, experimental temperature dependence of δ-effect increases with increasing temperature.

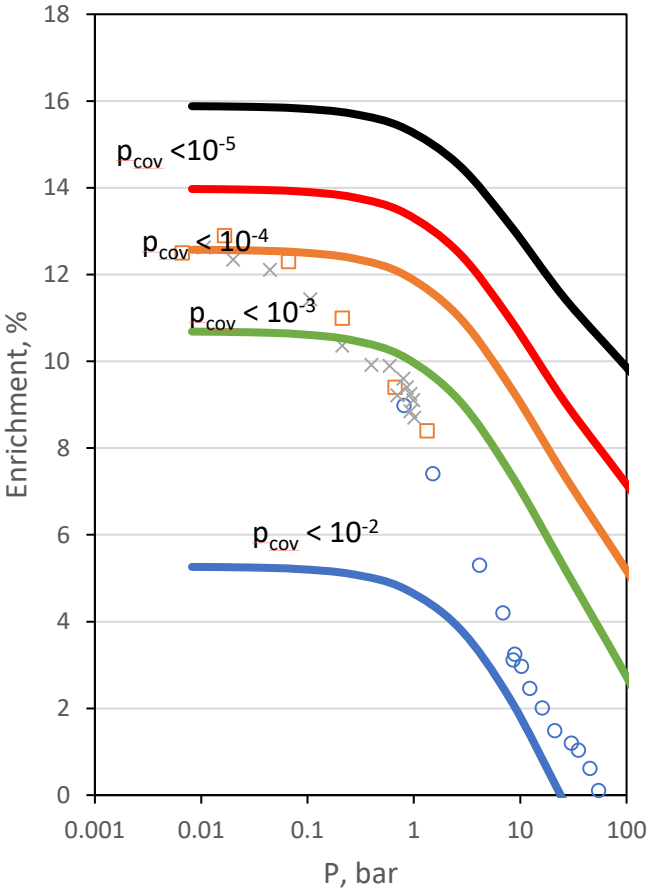

Figure 38. Experimental points for δ-effect with Γ-criteria = 1 cm^{-1}. A black curve corresponds to the theoretical prediction without any p-criteria, the red curve correspondes to $p_{cutoff} = 10^{-5}$, the orange - $p_{cutoff} = 10^{-4}$, the green - $p_{cutoff} = 10^{-3}$, the blue - $p_{cutoff} = 10^{-2}$.

To describe the experimental points both parameters of p_{cutoff} and Γ_{cutoff} were applied, and the best slope of the temperature dependence is shown in Figure 39. The absolute value of the δ-effect at given parameters drops to 1.77 % at 300 K.

To finish this chapter on a positive note, δ-effect for $^{16}O^{18}O^{16}O$ /$^{16}O^{16}O^{18}O$ and $^{16}O^{17}O^{16}O$/$^{16}O^{16}O^{17}O$ is found in good agreement with the experiment in terms of slope. The slopes of both curves are comparable to experiment.

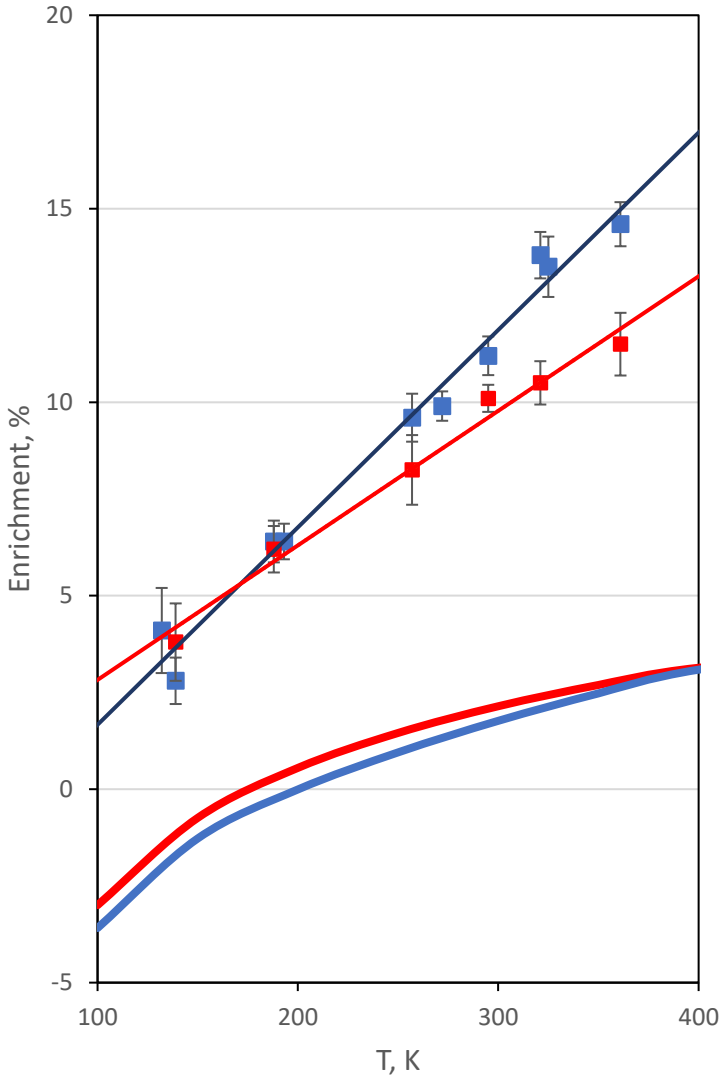

Figure 39. Experimental points for temperature dependence of δ-effect. The lower two bold lines correspond to the theoretical prediction with Γ-criteria - 1 cm^{-1} and all states included.

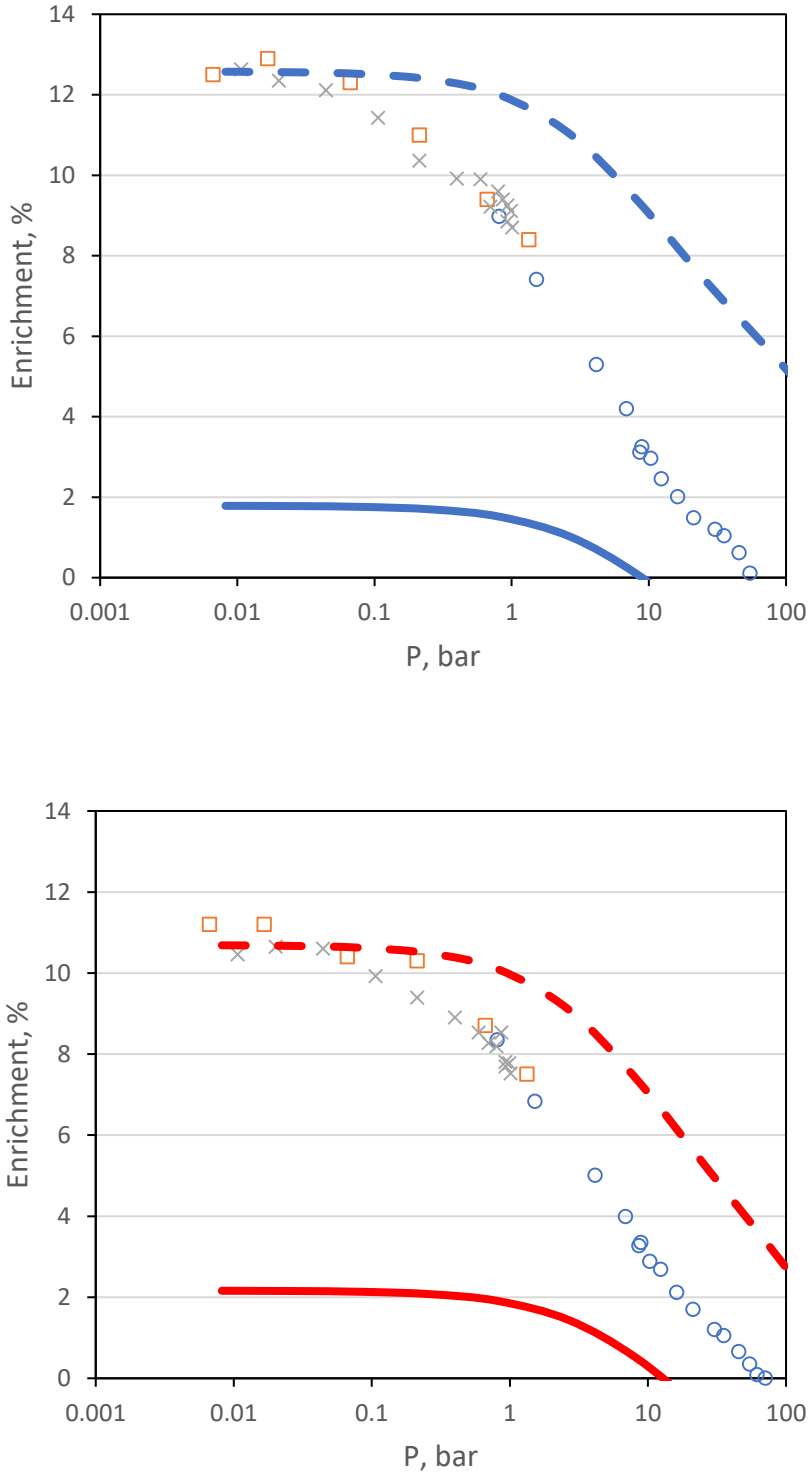

Figure 40. Experimental points for pressure dependence of δ-effect with Γ_{cutoff} = 1 cm^{-1}. Left picture corresponds to singly substituted molecule with ^{18}O, right picture corresponds so substitution with ^{17}O.

Table 18. The best fitting parameters to describe the temperature and pressure dependences of isotope effects and k_{666}. The results achieved with these parameters in terms of absolute value of η, δ-effects at 300 K, absolute value of k_{666}.

	ΔE, cm^{-1}	σ_{tran}, a_0^2	σ_{stab} a_0^2
Parameter	43.13	250	130
	P_{cutoff}	Γ_{cutoff}	
Parameter	10^{-3}	1	
	η	δ	$k_{666}*10^{35}$, cm^6/s
Result	1.07	10.5	60

In Figure 39 the red line corresponding to $^{16}O^{17}O^{16}O/^{16}O^{16}O^{17}O$ prevails over $^{16}O^{18}O^{16}O$ /$^{16}O^{16}O^{18}O$ at low temperatures and shows a tendency to exchange at the end of the temperature range, but still, they are very close to each other as in the experiment; this is the best achievement of this chapter. With the same parameters as in Figure 40 (solid lines) the absolute value of δ-effect has dropped drastically (see Figure 40), improvement of which lies outside this project and is left to reflection for future work.

The results of the theory are summarized in Figures 36-39 and in Table 18. With ΔE = 43.13 cm^{-1} and cross sections σ_{tran} = 250 a_0^2 , σ_{stab} = 130 a_0^2 the pressure and temperature dependences of k_{666} are described perfectly, the absolute value at 300 K is given in Table 18. The absolute values of isotope effects significantly increased with P_{cutoff} and Γ_{cutoff} criterion. The experimental η-effect at 300 K is 1.16 (according to Table 7), with the theory of Chapter IV was computed as 1.02 and has been improved to 1.07 (see Table 18). Notice that from experimental temperature dependence η-effect we had as 1.04 at 300 K (see Figure 37), the η =1.07 is a good achievement. The experimental δ-effect at 300 K is 11 % and this theory predicted it as 10.5 %. Both isotope predictions for η, δ -effect are valuable contributions to the recombination theory of ozone.

CHAPTER VII. SUMMARY

The ultimate goal of my study is the explanation of the mysterious mass-independent isotope effect. First, the complex stabilization kinetic theory of ozone recombination was proposed for singly and doubly sustituted isotopologues. The theory allows to split the resonance width and the corresponding decay rate coefficient onto two channel-specific contributions and rate coefficients for *stabilization* of scattering resonances onto two components, those that produce symmetric and asymmetric ozone molecules. Importantly, the κ_{sym} and κ_{asym} depend only on stabilization probabilities p_i^{sym} vs. p_i^{asym}, meanwhile the rate coefficients κ_{ch1} and κ_{ch2} has no probabilities but depend entirely on Γ_i^{ch1} and Γ_i^{ch2}. Doubly substituted isotopologue of ozone is similar to some extent to singly but the lower and upper channels flip and that affects the kinetic equations.

The application of general theory developed in Chapters II and III permitted to derive expressions for four pathways-specific rates of the recombination reaction that forms ozone. Including the insertion pathway for singly and doubly substituted cases, which was theoretically studied for the first time. The values of predicted rate coefficients κ_{I} are in good agreement with the experiment. This is an encouraging accomplishment of this work. Moreover, the ζ-effect related to κ_{I} also seems to be in a good agreement with the experiment.

Several issues discovered in the earlier theory were fixed and coefficients for the other three (major) reaction paths, κ_{A}, κ_{B} and κ_{S}, were updated. The new database was provided, and the first test involving new data for unsubstituted $^{16}O^{16}O^{16}O$ and singly substituted with isotope ^{17}O have been completed and discussed. Absolute values of these

rate coefficients are also in good agreement with the experiment. Quantum ζ-effect is in good agreement with the experiment for both single and double isotopic substitution. The mysterious η-effect is still small in comparison with the experiment but with certain parameters stay within the error bars in Figure 37. This question about temperature dependence of δ-effect remains open and extremely important and it needs to be better understood in future work. Systematic study of temperature dependence of the pathways-specific and channels-specific rate coefficients; the isotope effect reveals necessity of theory improvements. Incorporation of temperature dependent stabilization cross section is likely to improve comparison with the experiment.

Finally, we identified three types of resonances that corresponds to the vibrational states with wavefunctions localized in the covalent well of ozone, those delocalized over the van der Waals plateau and the asymptotic region of the PES.

The recommended future goals:

1) Change the strategy in the approach to understanding the master equation; particularly to give up on steady-state approximation and apply the so-called method of propagation and diagonalization based on the paper of Pack.[48]
2) To achieve the agreement between propagation and diagonalization methods of Pack[48] in application to singly and doubly substituted isotopologues with isotope ^{17}O and ^{18}O.
3) Possibly create the analytical approach to evaluate the kinetics which simulates the results of propagation and diagonalization but in a quick intuitive way and can be potentially applied to describe the isotope effect for the other molecules.

APPENDIX A. CALCULATION OF THE REAGENT PARTITION FUNCTIONS AND EQUILIBRIUM CONSTANTS FOR THE ISOTOPE EXCHANGE

The Exchange rate constant, for example, for singly substituted case is the equilibrium constant of:

$$68 + 6 \overset{K^{ex}}{\longleftrightarrow} 66 + 8$$

By definition it's the ratio of products over reactants $K^{ex} = \frac{[66][8]}{[68][6]} = \frac{Q_{\mathrm{ch1}} e^{-\frac{\Delta ZPE}{kT}}}{Q_{\mathrm{ch2}}}$, consists of two partition functions of product and reactants and Boltzmann's factor which appears in the upper channel B. Partition function in upper channel Q_{ch1} has a classical statistical properties in thermodynamic equilibrium and represent distribution over rotational, translational and electronic states. In upper channel B because of symmetry every other state is prohibited, so the rotational partition function includes degeneracy, Boltzmann factor and ΔZPE and is determined as sum over odd states:

$$Q_{\mathrm{rt1}} = \mathrm{e}^{-\frac{\Delta \mathrm{ZPE}}{kT}} \sum_{j=1,3,5,7,\ldots} (2j+1)\mathrm{e}^{-\frac{E^i(j)}{kT}} \qquad (187)$$

Alternatively, rotational partition may include all states, but the final sum must be reduced by half. Even though the second method is approximate, both methods give comparable results at low temperatures and identical at high temperatures.

Table 19. The rotational partition function calculated with two approaches for singly- and doubly substituted molecules in the wide range of temperatures.

T, K	66	66/2	88	88/2
1	0.046834	0.523426	0.074426	0.537251
10	2.577654	2.577872	2.878210	2.878269
100	24.207184	24.207184	27.219421	27.219421
200	48.246657	48.246657	54.271247	54.271247
250	60.266499	60.266499	67.797254	67.797254
293	70.603581	70.603581	79.429636	79.429636
298	71.805568	71.805568	80.782239	80.782239
300	72.286363	72.286363	81.323280	81.323280

Electronic and translational functions both depend on temperature. Translational partition function includes reduced mass, for singly and doubly substitution reduced masses slightly differ (the absolute values are given by Equations 169 and 170). The expressions for electronic and translational partition functions are the same for both isotopologues:

$$Q_{\mathrm{el}} = 3(5 + e^{\frac{-227.6}{T}} + e^{\frac{-325.9}{T}}) \tag{188}$$

$$Q_{\mathrm{tr}} = (\frac{\mu k T}{2\pi\hbar})^{\frac{3}{2}} \tag{189}$$

With all that the Equations partition functions in channel 1 and channel 2:

$$Q_{\mathrm{ch1}} = Q_{\mathrm{el}} Q_{\mathrm{tr}} Q_{\mathrm{rt1}} \tag{190}$$

$$Q_{\mathrm{ch2}} = Q_{\mathrm{el}} Q_{\mathrm{tr}} Q_{\mathrm{rt2}} \tag{191}$$

Rotational partition function for channel 2 with asymmetrical reactants has no prohibition with sum goes over all states:

$$Q_{\mathrm{rt2}} = \sum_{j=0,1,2,3,\ldots} (2j+1)\mathrm{e}^{-\frac{E^i(j)}{kT}} \tag{192}$$

In expression for doubly substituted exchange constant Q_{ch1} and Q_{ch2} are swapped and the factor $e^{-\frac{\Delta ZPE}{kT}}$ sticks to the upper Channel 2. Equations 188-189 are applicable for doubly substitution with proper reduced mass and energies.

Temperature dependence for two important component of rotational partition function – factor $\mathrm{e}^{-\frac{\Delta \mathrm{ZPE}}{\mathrm{kT}}}$ and ratio of $\frac{\mathrm{Q_{ch2}}}{\mathrm{Q_{ch1}}}$ was calculated (see Table 20). The temperature dependence is shown on Figure 41, magnitudes of curves are provided in the Table 19. Ratio of $\frac{Q_{\mathrm{ch2}}}{2Q_{\mathrm{ch1}}}$ shows no T-dependence, the factors with ΔZPE show significant t-dependence. And that can explain the source of pronounced T-dependence provided by Bella Tuzson[35] in his dissertation. At 300 K the exchange constant was calculate with absolute value for singly substituted case as 0.4627 (inverse – 2.1611). In the paper of

Table 20. Ratios singly- and doubly substituted exponential factors with ΔZPE corresponding partition functions ratio of channels and gradients per 1000 K (temperature dependence slopes at 300 K).

Ratio	Equation		Gradient*1000K	
	Singly sub	Doubly sub	Singly sub	Doubly sub
#0	$\mathrm{e}^{-\frac{\Delta \mathrm{ZPE}}{\mathrm{kT}}}$	$\mathrm{e}^{+\frac{\Delta \mathrm{ZPE}}{\mathrm{kT}}}$	0.345	-0.444
#1	$\frac{Q_{\mathrm{ch2}}}{2Q_{\mathrm{ch1}}}$	$\frac{Q_{\mathrm{ch2}}}{2Q_{\mathrm{ch1}}}$	0.00550	-0.000343

Hartorn and Marcus[37] the inverse experimental exchange constant is 2.16; at work of Janssen[10] is 2.1615. In doubly substituted molecule the exchange constant was gained as 1.8471 and in the paper of Hartorn and Marcus[37] – 1.85, in the data of Janssen[10] – 1.8474. To sum up the exchange constant was calculated with a good accuracy.

The temperature dependence of exchange recombination constant is taken from the literature as well. In dissertation work of Bella Tuzson[35] the recombination reaction is $66+8 \overset{K^{\mathrm{ex}}}{\longleftrightarrow} 68+6$. For singly substituted case temperature dependence due to Bella is described by Equation 194.

$$K^{ex} = 1.9481e^{31.652\frac{K}{T}}\left[1 - 1.28 * 10 - 5\left(\frac{T}{K}\right) + 2.32 * 10 - 8\left(\frac{T}{K}\right)^{2}\right] \qquad (193)$$

Which in comparison with current calculations of this work shown on Figure 42.

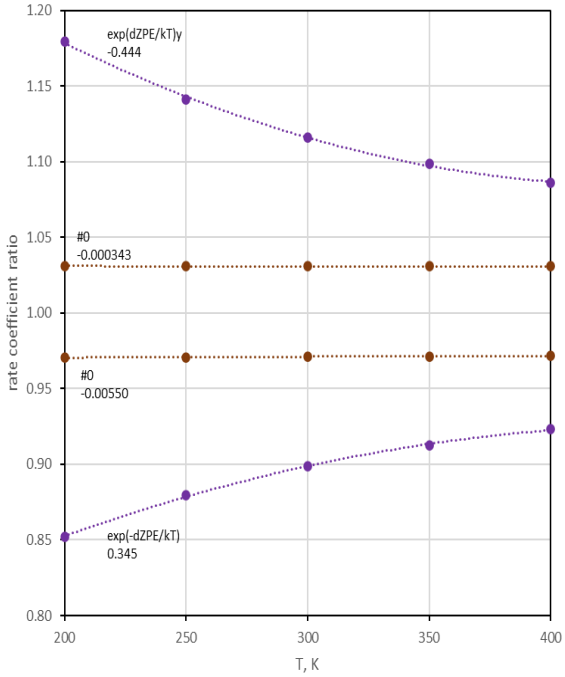

Figure 41. Temperature dependencies of $\frac{Q_{ch2}}{2Q_{ch1}}$ in comparison of T-dependence of $e^{-\frac{\Delta ZPE}{kT}}$. Brown curves are the ratio of partition functions in channels, purple curves are t-dependence of factors with ΔZPE.

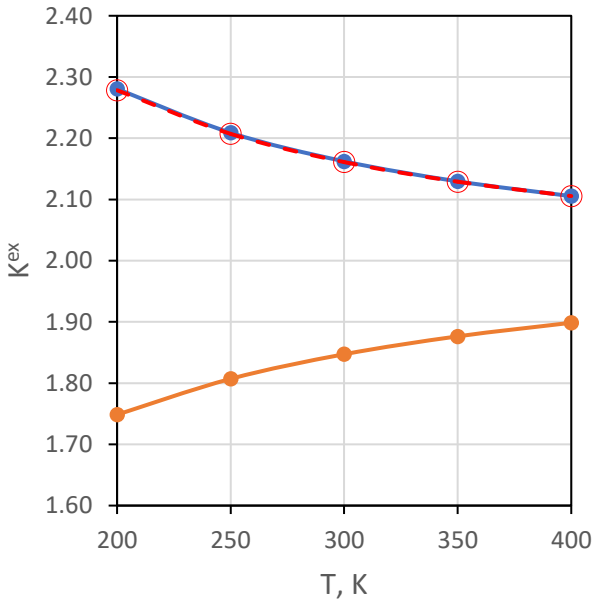

Figure 42. The temperature dependence of exchange rate coefficient for doubly (orange) and singly (blue) substituted molecule in comparison with experimental data of Bella.[35] Orange and blue lines show the theoretical prediction and red dotted line is the experimental. The measurements are in consistency with theoretical prediction.

BIBLIOGRAPHY

(1) Thiemens, M. H. History and applications of mass-independent isotope effects. *Annu. Rev. Earth Planet. Sci*. **2006**, 34, 217−262.

(2) Mauersberger, K., Measurement of heavy ozone in the stratosphere, *Geophys. Res. Lett.* **1981**, 8(8), 935– 937.

(3) Teplukhin, A. Theoretical Study of Ozone Forming Recombination Reaction and Anomalous Isotope Effect Associated with It, Marquette University, 2017.

(4) Peterson J.T., Demerjian K.L. The sensitivity of computed ozone concentrations to U.V. radiation in the Los Angeles area. *Atmospheric Environment*. **1967**, 10, 6, 459-468.

(5) Fishman, J., and Brackett, V. G. The climatological distribution of tropospheric ozone derived from satelite measurements using version 7 Total Ozone Mapping Spectrometer and Stratospheric Aerosol and Gas Experiment data sets, *J. Geophys. Res.* 1997, 102 (D15), 19275– 19278.

(6) Thiemens, M. H. Nonmass-Dependent Isotopic Fractionation Processes: Mechanisms and Recent Observations in Terrestrial and Extraterrestrial Environments. *Treatise on Geochemistry*. **2007**, 4,1−24.

(7) Thompson, D., Solomon, S., Kushner, P. *et al.* Signatures of the Antarctic ozone hole in Southern Hemisphere surface climate change. *Nature Geosci*. **2011**, 4, 741–749.

(8) Lide, D. R. *CRC Handbook of Chemistry and Physics*, 2004, 85th.

(9) Thiemens, M. H. Mass-independent isotope effects in planetary atmospheres and the early solar system. Science **1999**, 283, 341−345.

(10) Janssen, C.; Guenther, J.; Mauersberger, K.; Krankowsky, D. Kinetic Origin of the Ozone Isotope Effect: A Critical Analysis of Enrichments and Rate Coefficients. *Phys. Chem. Chem. Phys*. **2001**, 3, 4718–4721.

(11) J. C. Janssen. Investigation and Assessment of an Oxygen Isotope Anomaly. 2004

(12) Thiemens, M.; Chakraborty, S.; Dominguez, G. The physical chemistry of mass-independent isotope effects and their observation in nature. *Annu. Rev. Phys. Chem.* **2012**, 63, 155−177.

(13) Thiemens M. H., Heidenreich J E. The Mass-Independent Fractionation of Oxygen: A Novel Isotope Effect and Its Possible Cosmochemical Implications. *Science*. **1983**, 219, 4588, pp. 1073-1075

(14) Teplukhin, A.; Babikov, D. Several Levels of Theory for Description of Isotope Effects in Ozone: Symmetry Effect and Mass Effect. *J. Phys. Chem. A.* **2018**

(15) Ivanov, M. V.; Schinke, R. Temperature Dependent Energy Transfer in Ar–O_3 Collisions. *J. Chem. Phys.* **2005**, *122*, 234318.

(16) Hippler, H.; Rahn, R.; Troe, J. Temperature and Pressure Dependence of Ozone Formation Rates in the Range 1–1000 Bar and 90–370 K. *J. Chem. Phys.* **1990**, *93*, 6560–6569.

(17) Troe, J. Toward a Quantitative Analysis of Association Reactions in the Atmosphere. Chem. Rev. **2003**, 103, 4565-4576.

(18) Ivanov M. V., R. Schinke R. Recombination of ozone via the chaperon mechanism. *J. Chem. Phys*. **2006**, 124, 104303.

(19) K. Luther, K. Oum and J. Troe, The role of the radical-complex mechanism in the ozone recombination/dissociation reaction. *Phys. Chem. Chem. Phys.*, **2005**, **7**, 2764-2770

(20) Charlo D., Clary D. C. Quantum-mechanical calculations on termolecular association reactions XY+Z+M→XYZ+M: Application to ozone formation. *The Journal of Chemical Physics*. **2002** 117, 1660.

(21) Babikov D. Accuracy of gates in a quantum computer based on vibrational eigenstates. The Journal of Chemical Physics. **2004**, 121(16), 7577-7585.

(22) Teplukhin A., Babikov D., Properties of Feshbach and 'shape'-resonances in ozone and their role in recombination reaction and anomalous isotope effects. *Faraday Discuss.***, 2018**, 212**,** 259-280.

(23) Lin, C.L. and Leu, M.T. Temperature and third-body dependence of the rate constant for the reaction O + O2 + M → O3 + M. Int. J. Chem. Kinet. **1982**, 14: 417-434.

(24) Günther J., Krankowsky, D., Mauersberger, K. Third-body Dependence of Rate Coefficients for Ozone Formation in 16O — 18O Mixtures', *Chem. Phys. Lett*. **2000**, 324, 31–36.

(25) Teplukhin, A.; Gayday, I.; Babikov, D. Several Levels of Theory for Description of Isotope Effects in Ozone: Effect of Resonance Lifetimes and Channel Couplings. *J. Chem. Phys*. **2018**, 149, 164302.

(26) Marcus, R. A. Theory of Mass-Independent Fractionation of Isotopes, Phase Space Accessibility, and a Role of Isotopic Symmetry. *Proc. Natl. Acad. Sci.* **2013**, 110, 17703–17707.

(27) Mauersberger, K.; Erbacher, B.; Krankowsky, D.; Günther, J.; Nickel, R. Ozone Isotope Enrichment: Isotopomer-Specific Rate Coefficients. *Science (80-.).* **1999**, *283*, 370–372.

(28) Babikov, D.; Kendrick, B. K.; Walker, R. B.; Pack, R. T.; Fleurat-Lesard, P.; Schinke, R. Formation of Ozone: Metastable States and Anomalous Isotope Effect. *J. Chem. Phys.* **2003**, *119*, 2577–2589.

(29) Babikov D, Kendrick BK, Walker RB, Schinke R, Pack RT. Quantum origin of an anomalous isotope effect in ozone formation. *Chemical Physics Letters*. **2003,** 372: 686-691.

(30) Meng Q., Chem J. Ring-polymer molecular dynamics study on rate coefficient of the barrierless OH + CO system at low temperature. *J. Chem. Phys*. **2019**, 150, 044307.

(31) Teplukhin A., Babikov D. A full-demintional model of ozone forming reaction: the absolute value of the recombination rate coefficient, its pressure and temperature dependenciies. *Phys. Chem. Chem.* Phys. **2016**, 18, 19194

(32) Babikov, D.; Kendrick, B. K.; Walker, R. B.; Pack, R. T.; Fleurat-Lesard, P.; Schinke, R. Metastable States of Ozone Calculated on an Accurate Potential Energy Surface. *J. Chem. Phys.* **2003**, 118, 6298–6308.

(33) Ivanov M., Babikov D. Efficient quantum-classical method for computing thermal rate constant of recombination: Application to ozone formation. *J. Chem. Phys.* **2012**, 136, 184304

(34) Gao Y.Q.,Marcus A. Strange and Unconventional Isotope Effects in Ozone Formation. **Science**. **2001**, 293, 5528

(35) Janssen, C. & Platt, U. Symmetry specific study of ozone isotopomer formation. (2005).

(36) Hathorn, B. C.; Marcus, R. A. An Intramolecular Theory of the Mass-Independent Isotope Effect for Ozone. II. Numerical Implementation at Low Pressures Using a Loose Transition State. *J. Chem. Phys.* **2000**, *113*, 9497–9509.

(37) Babikov, D.; Kendrick, B. K.; Walker, R. B.; Pack, R. T.; Fleurat-Lesard, P.; Schinke, R. Metastable States of Ozone Calculated on an Accurate Potential Energy Surface. *J. Chem. Phys.* **2003**, *118*, 6298–6308.

(38) Schinke, R.; Grebenshchikov, S. Y.; Ivanov, M. V.; Fleurat-Lesard, P. Dynamical Studies of the Ozone Isotope Effect: A Status Report. *Annu. Rev. Phys. Chem.* **2006**, *57*, 625–661.

(39) Marcus, R. A. Theory of Mass-Independent Fractionation of Isotopes, Phase Space Accessibility, and a Role of Isotopic Symmetry. *Proc. Natl. Acad. Sci.* **2013**, *110*, 17703–17707.

(40) D. Charlo, D. C. Clary. The Journal of Chemical Physics 120, 2700 (2004).

(41) Braams, B. J.; Bowman, J. M. Permutationally Invariant Potential Energy Surfaces in High Dimensionality. *Int. Rev. Phys. Chem.* **2009**, *28*, 577–606.

(42) Reinhardt P., Robert F. On the mass independent isotope fractionation in ozone. Chemical Physics. **2018**. 513, 287-294.

(43) Janssen C. Intramolecular isotope distribution in heavy ozone ($^{16}O^{18}O^{16}O$ and $^{16}O^{16}O^{18}O$). *Journal of geophysical reserch*. **2005**, 110, D08308.

(44) Petty, C.; Spada, R. F. K.; Machado, F. B. C.; Poirier, B. Accurate Rovibrational Energies of Ozone Isotopologues up to $J = 10$ Utilizing Artificial Neural Networks. *J. Chem. Phys.* **2018**, *149*, 024307.

(45) Babikov D., Gislason E., Sizun M., Aguillon F., Sidis V., Barat M., Brenot J., Fayeton J. A., Picard Y. J.. Dalitz plot analysis of three-body fragmentation of Na 3 + excited by He impact. *Journal of Chemical Physics,* **2002.**

(46) De Cobos, A. E. C. & Troe, J. High-pressure range of the recombination O + O2 → O3. *Int J Chem Kinet* **16**, 1519–1529 (1984).

(47) Forrey, R. C. Sturmian theory of three-body recombination: Application to the formation of H2 in primordial gas. *Phys Rev A* **88**, 052709 (2013).

(48) T Pack, R., Walker, R. B. & Kendrick, B. K. Three-body collision contributions to recombination and collision-induced dissociation. II. Kinetics. *Journal of Chemical Physics* **109**, 6714–6724 (1998).